FINAL TECHNICAL REPORT
(December 31, 2006)

Project Title: Co-seismic and post-mainshock study on the San Andreas fault ruptured in the 2004 *M*6 Parkfield earthquake.

Award Number: 06HQGR0027

Sponsor: US Geological Survey

Principal Investigator: Yong-Gang Li
Department of Earth Sciences
University of Southern California
Los Angeles, CA 90089-0740
E-mail: ygli@terra.usc.edu
Tel: 213-740-3556
Fax: 213-740-8801

Proposed Start Date: December 1, 2005.

Proposed Duration: 12 months.

Key Words: Fault Dynamics, Wave Propagation, Earthquake Effects

Non-technical Summary:

Immediately after the *M*6 Parkfield earthquake on September 28, 2004, we installed a dense seismic array of 45 PASSCAL RT130s across and along the San Andreas Fault near the town of Parkfield to record fault-zone trapped waves generated by aftershocks. The array was located in the middle of a high-slip part of the surface rupture in this earthquake, and co-sited in our previous experiment conducted in the fall of 2002. We recorded the data for ~ 1000 aftershocks in 3 months starting from a week after the mainshock. In the end of 2004, we detonated 2 near-surface explosions within the rupture zones in Middle Mountain and southeast of Parkfield town. We observed significant fault-zone trapped waves from explosions and aftershocks occurring within the rupture zone. Many events occurred at the depths below 5 km, giving us a good opportunity to document the damage structure of fault zone at seismogenic depths. Preliminary results from the fault-zone trapped wave data recorded at our array show existence of a low-velocity zone ~100-150-m wide on the fault, which extends across the seismogenic depths. Within the zone, *Q* is 10-50 and seismic velocities are reduced by 30-50% from wall-rock velocities, with the great velocity reduction at shallower depth [Li et al., 2004]. We interpret that this distinct low-velocity zone is a result of repeated damage in historical earthquakes on the SAF at Parkfield. The trapped wave data also show the greater velocity reduction on the fault segment near the town of Parkfield where the anomalous largest peak acceleration and the larger slip were measured in the recent *M*6 earthquake.

Repeated explosions and earthquakes at the SAF before and after the 2004 *M*6 Parkfield earthquake show a peak ~2.5% decrease in seismic waves within a ~200-m-wide fault zone at seismogenic depths, most likely due to co-seismic damage of fault-zone rocks during dynamic rupture of this *M*6 mainshock. The measured ratio between the *P* and *S* wave traveltime changes indicates wetter cracks within the damaged fault zone, probably due to the ground water percolating into the cracks opened in the mainshock. Waveform cross-correlation measurements for repeated aftershocks show a ~1.2% velocity increase within the fault zone in the 3-4 months after the mainshock, indicating that the fault heals through time. The healing rate is approximately logarithmic with the largest healing rate in the earliest stage of post-mainshock. The magnitude of fault damage and healing varies along the rupture zone, and is

most prominent at depths above ~7 km. Observations of rock damage during the mainshock and healing thereafter on the SAF at Parkfield illuminate the conceptual framework of faulting-healing progression on an active fault in the earthquake cycle.

Intellectual Merit. So far, because of the density and frequency of our data, this study may be the first to illuminate the temporal-spatio patterns of damage on a major fault zone due a *M*6 earthquake in 4-D. In contrast to the Landers and Hector Mine earthquakes examined previously, in the present case, our deployments straddle the mainshock and thus we are able to isolate co-seismic changes as well as the post-mainshock healing. The results have implications for the physics of co-seismic and post-seismic faulting processes. Further, because of the types and quality of our observations, our work provides fundamental information on the nature and source of the fault damage in situ. This research will help to develop and test models of large and small earthquake occurrence at Parkfield.
Broader Impact. The work done through this project helps to determine the evolution of physical properties that might control the onset and characteristics of damaging earthquakes. As part of this excise, the *M*6 Parkfield earthquake can be taken as a validation test to assess the faulting process on active faults globally. This study is to utilize data collected by USGS and partner organizations USArray and SAFOD components of EarthScope facility at Parkfield. The project involves graduate student research and scholarly exchange between USC and other institutions.

ACTIVITIES:

We have used fault-zone guided waves (FZGW) generated by local microearthquakes and explosions to delineate a ~150-m-wide low-velocity zone (LVZ) with highly damage at seismogenic depths, within which seismic velocities are reduced by 25-45% from wall-rock velocities. The ~150-m LVZ on the SAF inferred from FZGW has been confirmed by SAFOD drilling. The data from repeated explosions and aftershocks show that seismic velocities were decreased by ~2.5% within the ~150-m-wide zone along the fault strike at seismic depths before and after this *M*6 earthquake, most likely owing to the co-seismic damage of fault-zone rocks during dynamic rupture in the mainshock. The damage zone is not symmetric but extends farther on the southwest side of the main fault trace. We interpret that the distinct low-velocity waveguide along the principal slip plane of the SAF at depth is a remnant of repeated damage caused by large historical earthquakes on the SAF. The 2004 *M*6 Parkfield earthquake added the damage on it. Soon thereafter we observed seismic velocities increased by ~1.2% within the fault zone in ~4 months starting a week after the *M*6 earthquake, indicating that the damaged rock has been healing and regaining the strength through rigidity recovery with time, most likely due to the closure of cracks that had opened during the mainshock. The fault healing is most prominent at depths above ~7 km. The healing rate was not constant with time but largest in the earlier stage of post-mainshock healing process. The preliminary results indicate that the greater damage was inflicted and thus greater healing is likely observed, in regions with larger slips in the mainshock. We also did shear-wave splitting (SWS) analysis using these data, and found that the fast shear-wave polarization direction nearly fault-parallel within a ~150-m-wide zone of pervasive cracking and damage interpreted from FZGW while the fast shear wave orientations outside the zone are roughly parallel to the regional maximum horizontal compressive stress direction. The measured SWS is likely due to a combination of stress-aligned micro-cracks away from the fault and shear fabric within the highly evolved fault core (damage zone). Results from our research at the SAF, Parkfield have produced 4 papers listed below**.**

PUBLICATIONS:

1. Li, Y. G., P. Chen, E. S. Cochran, J. E., Vidale, and T. Burdette, Seismic evidence for rock damage and healing on the San Andreas fault associated with the 2004 *M*6 Parkfield earthquake, Special issue for Parkfield *M*6 earthquake, *Bull. Seism. Soc. Am.*, 96, No.4, S1-15, doi:10.1785/0120050803, 2006.

2. Cochran, S. E., Y. G. Li, and J. E. Vidale, Anisotropy in the shallow crust observed around the San Andreas fault before and after the 2004 M6 Parkfield earthquake, Special issue for Parkfield *M*6 earthquake, *Bull. Seism. Soc. Am.*, 96, S1-10, doi:10.1785/0120050804, 2006.

3. Li, Y. G., J. E. Vidale, and P. E. Malin, Parkfield fault-zone guided waves: High-resolution delineation of the low-velocity damage zone on the San Andreas fault at seismogenic depth near SAFOD site, *The Proceeding of ICDP-IODP Fault-Zone Drilling*, pp 1-4, Miyazaki, Japan, 2006.

4. Li, Y. G., P. Chen, E. S. Cochran, and J. E. Vidale, Seismic velocity variations on the San Andreas Fault caused by the 2004 *M*6 Parkfield earthquake and their implications, Earth, Planets and Space, in press, 2006.

The electronic versions of these 4 papers are attached in this report. Dr. Yong-Gang Li is the contact person for the ability of data acquired in this project (see the fist page).

Seismic Evidence for Rock Damage and Healing on the San Andreas Fault Associated with the 2004 *M*6 Parkfield Earthquake

By Yong-Gang Li, Po Chen, Elizabeth S. Cochran, John E. Vidale, and Thomas Burdette

Abstract We deployed a dense linear array of 45 seismometers across and along the San Andreas fault near Parkfield a week after the *M*6 Parkfield earthquake on September 28, 2004 to record fault-zone seismic waves generated by aftershocks and explosions. Seismic stations and explosions were co-sited with our previous experiment conducted in 2002. The data from repeated shots detonated in the fall of 2002 and 3 months after the 2004 *M*6 mainshock show ~1.0-1.5% decreases in seismic wave velocity within an ~200-m-wide zone along the fault strike and smaller changes (0.2-0.5%) beyond this zone, most likely due to the coseismic damage of rocks during dynamic rupture in the 2004 *M*6 earthquake. The width of the damage zone characterized by larger velocity changes is consistent with the low-velocity waveguide model on the San Andreas fault, near Parkfield that we derived from fault-zone trapped waves (Li *et al.*, 2004). The damage zone is not symmetric but extends farther on the southwest side of the main fault trace. Waveform cross-correlations for repeated aftershocks in 21 clusters, with a total of ~130 events, located at different depths and distances from the array site show ~0.7-1.1% increases in *S*-wave velocity within the fault zone in 3 months starting a week after the earthquake. The velocity recovery indicates that the damaged rock has been healing and regaining the strength through rigidity recovery with time, most likely due to the closure of cracks opened during the mainshock. We estimate that the net decrease in seismic velocities within the fault zone was at least ~2.5% caused by the 2004 *M*6 Parkfield earthquake. The healing rate was largest in the earlier stage of post-mainshock healing process. The magnitude of fault healing varies along the rupture zone, being slightly larger healing beneath Middle Mountain, correlating well with an area of large mapped slip. The fault healing is most prominent at depths above ~7 km.

INTRODUCTION

Extensive field and laboratory research, and numerical simulations indicate that the fault zone undergoes high, fluctuating stress and pervasive cracking during an earthquake (e.g., Dieterich, 1978; Aki, 1984; Scholz, 19990; Rice, 1992; Kanamori, 1994). While we know slip is localized on faults because of their lower strength compared to the surrounding bedrock, critical parameters remain practically unknown (e.g., Sleep et al., 2000). For example, the friction laws are approximate, and damage and healing rates are poorly constrained (e.g., Richardson and Marone, 1999). Perhaps most critically, the magnitude of the strength reduction and its spatial extent has only been measured partially and at a few places before (e.g., Hickman and Evans, 1992; Vidale et al; 1994). Earthquake-related fault-zone damage and healing have been documented quantitatively in only a few cases (e.g., Marone et al., 1995; Li et al., 1998, 2003; Massonnet et al., 1999; Yasuhara et al., 2004). In order to relate present-day crustal stresses and fault motions to the geological structures formed in their past earthquake histories, we must understand the evolution of fault systems on many spatial and time scales. Major crustal faults are structurally marked by zones of lowered velocity with a width of a few hundred meters to a few kilometers (Mooney and Ginzburg, 1986). Intense fracturing during earthquakes, brecciation, liquid-saturation and possibly high pore-fluid pressure near the fault are thought to create these low-velocity zones. The size and magnitude of the low-velocity anomalies on active faults might vary over the earthquake cycle as observed in our previous studies at rupture zones of the 1992 M7.4 Landers and 1999 M7.1 Hector Mine, California earthquakes (Li et al., 1998, 2003; Li and Vidale, 2001; Vidale and Li, 2003).

Research at the San Andreas fault (SAF) at Parkfield has revealed a low-velocity zone a few hundred meters to 1 km wide with velocity reductions of 10-30% and a *Vp/Vs* ratio of 2.3 surrounding the surface trace of the SAF (e.g. Lees and Malin, 1990; Michelini and McEvilly, 1991; Eberhart-Phillips and Michael, 1993; Thurber *et al.*, 1997; 2003; Roecker *et al.*, 2004). The low *Vs* and corresponding high *Vp/Vs* ratios within the fault zone have been interpreted to be caused by dilatant fracturing due to high pore-fluid pressures. Magnetotelluric imaging of the SAF at Parkfield yields a similar model, with a zone of very low resistivity a few hundred meters wide extending to a depth 3-4 km (Unsworth *et al.*, 1997); the low-resistivity zone is interpreted to be fluid-rich. Byerlee (1990) and Rice (1992) suggest that pore fluids migrate up from depth and the fault-zone acts as a channel due in part to its greater permeability than adjacent blocks. Recent initial results from SAFOD drilling and borehole logs at Parkfield show a low velocity zone with high

porosity a couple of hundred meters wide at the ~3.2 km depth, indicating a damage zone associated with the SAF (Hickman *et al.*, 2005).

Fault-zone trapped wave studies at Parkfield have shown a highly fractured zone characterized by a low-velocity waveguide on the SAF (Li *et al.*, 1990, 1997; Malin *et al.*, 1998, 2004; Shalev and Malin, 2005; Korneev *et al.*, 2000). We carried out an experiment at Parkfield in 2002 to record fault-zone trapped waves generated by near-surface explosions and microearthquakes within the fault zone, and used these waves to delineate a ~150-m wide low-velocity zone, in which seismic velocities are reduced by 25-40% and seismic attenuation Q values are ~20-50, along the fault strike at depths above 5 km (Li *et al.*, 2004). The data recorded after the 2004 M6 Parkfield earthquake at our 2004 seismic array, co-sited with the experiment in 2002 provide better constraints on the depth extent of the damage structure on the SAF.

In this paper, we report our observations of temporal changes in seismic velocity for repeated explosions detonated within the SAF on October 16, 2002 and on December 28, 2004 to document the co-seismic damage associated with the 2004 M6 Parkfield earthquake. In addition, results from repeated aftershocks recorded for 3 months starting a week after the mainshock confirm post-mainshock healing of fault-zone rocks.

DATA AND RESULTS

After the M6 Parkfield earthquake on September 28, 2004, we deployed a dense seismic array of 45 PASSCAL 3-channal RT130 seismometers across and along the San Andreas Fault (SAF) near the town of Parkfield to record aftershocks (Fig. 1a). The across-fault array A consisted of 35 stations with station spacing of 25 m while array B and array C with station spacing 50 m were along the main SAF main trace and north strand. The array site was located in the middle of a high-slip part of the surface rupture in this earthquake, and co-sited with our experiment conducted at Parkfield in the fall of 2002. L22 2Hz sensors were buried at the same locations as in the previous experiment. The three components of the sensor at each station were aligned vertical, parallel, and perpendicular to the fault trace. Coordinates of station ST0 of array A, located on the SAF main trace are 35°N54.566' and 116°W26.954'. Seismometers operated in a continuous mode, with sample rate at 100 samples per second. We recorded ~1000 aftershocks in 3 months, starting a week after the mainshock. On December 28 of 2004, we detonated 2 near-surface explosions, each using ~250 kilograms of chemical explosives in a 30 m-deep hole drilled within the fault zone. The signals from shots were sampled at a rate of 500 samples per second. Shots PMM and WORK were located ~7 km northwest and ~9 km southeast of the array site. Shot PMM was a repeated explosion at the same shot-hole site in middle Mountain as in our previous experiment in 2002. Coordinates of the shot-hole were 35°N57.481' and 116°W30.237'. The clocks of all recorders and shot times were synchronized through Global Positioning System (GPS). The timing errors for recorders and explosions were less than 2 milliseconds. In the following part of this section, we show results from a quantitative analysis of the data from repeated shots and aftershocks to examine seismic velocity changes near the fault caused by this M6 earthquake at Parkfield.

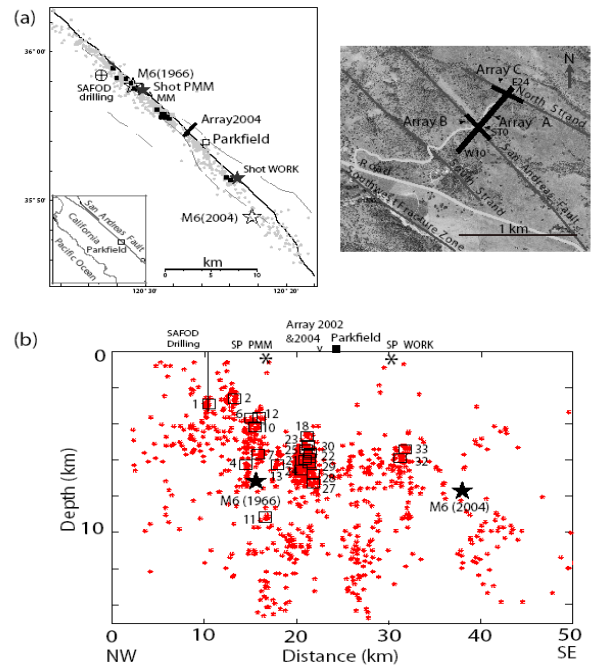

Figure 1. (a) Maps show locations of seismic array (denoted by bars), shots (solid stars) and aftershocks (dots) of the M 6.0 earthquake on 28 September 2004 at Parkfield, California. Seismic arrays were deployed across and along the San Andreas fault in 2002 and 2004. Solid squares denote clusters of repeated aftershocks used for this study. Array A consisted of 35 PASSCAL RT130s and 2-Hz L22 sensors with station spacing of 25 m. Arrays B and C consisted of 6 RT130s for each with station spacing of 50 m. Station ST0 was located on the main fault trace. Gray and white lines are fault surface traces and roads. Fault lines and topographic map are provided by Michael Rymer of the USGS. (b) The vertical section along the San Andreas fault at Parkfield shows locations of the seismic array, shots, the 1966 and 2004 M 6.0 earthquakes, and aftershocks in 2004. Twenty-one squares (labeled by numbers) denote clusters of repeated aftershocks; each cluster includes at least five similar aftershocks located within 200 m.

1. Repeated Shots

Figure 2a shows three-component seismograms recorded at array A across the SAF for shot PMM detonated on December 28, 2004. Fault-zone guided waves were dominant at stations close to the main fault trace, similar to those recorded at the same stations for this shot on October 16, 2002 (Li *et al.*, 2004). In Figure 2b, seismograms recorded for the repeated shots in 2002 and 2004 are overlaid with the shot times aligned at 0 s. The first P-arrivals at the wellhead geophone show identical travel times for repeated shots. However, traveltimes of P, S and fault-zone guided waves at stations near the fault for the shot in 2004 were delayed by several

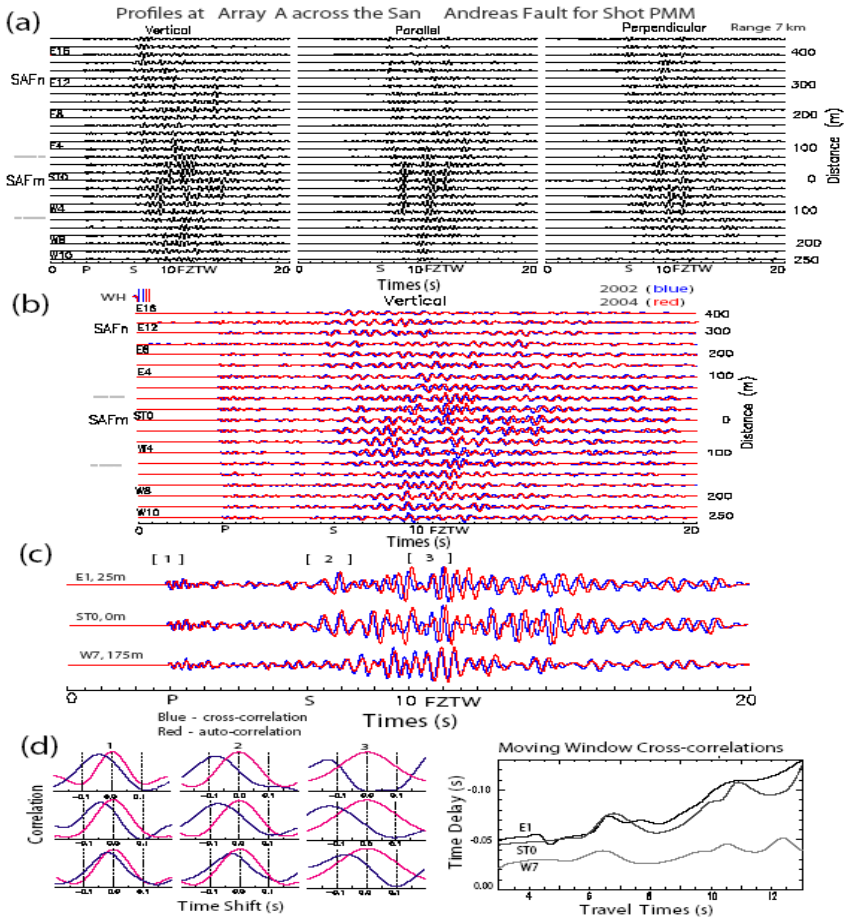

Figure 2. (a) Three-component seismograms recorded at array A across the San Andreas fault for shot PMM detonated at 7 km northwest of the array in 2004. Seismograms have been low-pass (<3-Hz) filtered and are plotted using a common scale for all traces in each plot. Station names and offsets from the fault are plotted. Stations ST0 and E15 were located on the main fault (SAFm) and north strand (SAFn). The shot origin time is at 0 sec. P and S waves arrive at ~3 sec and ~7 sec. Fault-zone trapped waves (FZTW) with large amplitudes and long wavetrains are dominant between S arrival and 15 sec at stations in the range of ~150 m marked by two bars. (b) Vertical-component seismograms at Array A for shot PMM in 2002 and 2004. Similar waveforms were recorded in repeated experiments, but waves traveled slower after the M 6.0 Parkfield earthquake in 2004. WH denotes the station located at the wellhead of shot-hole; the unclipped first P arrivals show identical arrival times for the repeated shots. (c) Vertical-component seismograms recorded at three stations within and out of the fault zone for shot PMM in 2002 and 2004. (d) Left: Autocorrelations (red lines) of seismograms in 2004 and cross-correlations (blue lines) of recordings at the same station in 2002 and 2004 for three time windows 1 to 3 including *P*, *S*, and trapped waves, respectively. The peak of the autocorrelation curve is at zero lag time in each window. The negative time shift indicates time advance. Greater time delays of waves in 2004 were registered at stations E1 and ST0 than at station W7. Right: Moving-window cross-correlations of waveforms at the three stations for shot PMM in 2002 and 2004 show time delays in 2004.

tens milliseconds. We measured the traveltime delays using waveform cross-correlation in 3 time windows including the *P*, *S* and trapped waves, respectively, for each pair of recordings at the same recorder in 2002 and 2004. The length of Hanning tapered time window is 0.5 s for *P* waves, 1 s for *S*, and 1.5 s for guided waves. Figure 2c exhibits vertical-component seismograms recorded at 3 stations of array A for shots in 2002 and 2004. Cross-correlations of the waveforms in 3 time windows are shown in Fig. 2d. Traveltimes of *P*, *S*, and guided waves to stations STO and E1 within the fault zone were delayed by 45, 80, and 120 ms in 2004 while traveltimes were delayed by 20, 35, and 50 ms at station W7 located 175m away from the fault, indicating larger velocity decreases within the fault zone. The measured changes in traveltimes are much larger than the uncertainty in the origin time of the explosion (a few milliseconds).

We applied the moving window cross-correlation technique developed by Niu *et al.* (2003) based on the method used in Coda-wave interferometry for estimating

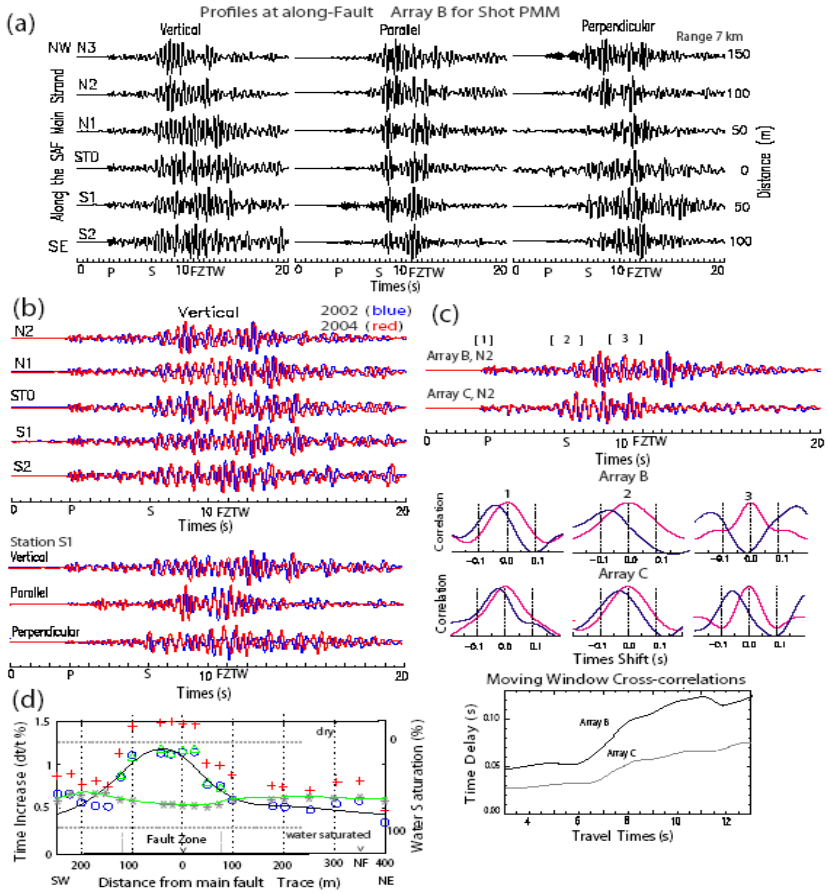

Figure 3. (a) Three-component seismograms recorded at array B along the main trace of San Andreas fault for shot PMM in 2004. Seismograms have been <3-Hz filtered and are trace-normalized in plot. Station names and distances from station ST0 are plotted. Other notations are the same as in Figure 2. (b) Overlapped seismograms recorded at Array B for repeated shot PMM in 2002 and 2004 show similar waveforms, but waves traveled slower after the 2004 M 6.0 Parkfield earthquake. (c) Vertical-component seismograms recorded at station N2 of array B and station N2 of array C for repeated shot PMM. Cross-correlations of recordings in 2002 and 2004 for time windows 1 to 3 including *P*, *S*, and trapped waves (top) and for moving-window show travel-time delays in 2004, with larger delays at array B along the main fault than those at array C along the north strand. (d) Travel-time increases, in percent, for P (crosses), S (circles), and trapped waves (triangles) measured from cross-correlations of seismograms at array A across the SAF for repeated shot PMM in 2002 and 2004, showing that seismic velocities decreased after the 2004 M 6.0 earthquake due to rock damage within the fault zone. Some stations did not work in both experiments due to weather and battery problem. The black line is a polynomial fit to travel-time increases of S waves in 2004. A pair of vertical gray bars denotes a zone with greater travel-time increases. Ratio of travel-time changes for P waves to S waves (gray stars with a curve) indicate the degree of water saturation in cracks. Two horizontal light lines indicate the ratios predicted for a range of water percentage for a Poisson solid. NF, north fault strand decrease in shear rigidity of the fault-zone rock during the time period between two repeated shots.

nonlinear behavior in seismic velocity (Snieder *et al.*, 2002) to measure the traveltime changes of seismic phases between the recordings from repeated shots. We examined low-pass (<3 Hz) filtered seismograms using a 1-s window for cross-correlation with the window center moving from the first *P*-arrival to later *S* coda. To ensure reliable results from computations, we enforce a minimum correlation coefficient of 0.8 for the *P*, *S* and guided waves. For example, Figure 2d shows moving window cross-correlations of seismograms at 3 stations ST0, E1 and W7 of array A for shots in 2002 and 2004. The absolute traveltime delays in 2004 increase progressively for *P*, *S*, and guided waves, consistent with the measurements in 3 time windows shown above.

Figure 3 shows results from array B along the main fault and array C along the north strand for repeated shot PMM in 2002 and 2004. Figure 3a exhibits fault-zone guided waves with longer wavetrains following *S* waves on array B than those on array C. The overlaid seismograms recorded in 2002 and 2004 show clearly that waves traveled slower in 2004, indicating seismic velocity decreases within the fault zone (Fig.3b). Figure 3c shows overlaid seismograms and correlations of recordings in 2002 and 2004 at station N2 of array B and station N2 of array C. The measured traveltime delays for *P*, *S*, and guided waves in 2004 are 45, 85, and 125 ms on array B, but are 25, 42, and 65 ms on array C, showing-larger velocity decreases within the rupture zone along the main

fault. In Figure 3d, we plot the percentage increase in traveltimes of *P*, *S*, and fault-zone guided waves at all stations on arrays A, B and C for repeated shot PMM. Larger changes in traveltimes were observed at stations located closer to the fault trace in a range of ~200 m.

Assuming velocity changes were uniform in the crust sampled by these waves, the increases in traveltime are straightforward to interpret. The *P* wave arrived with a 45 ms delay in 2004, with a traveltime of ~3 s, so the *P* wave velocity decreased by ~1.5% within the fault zone between the fall of 2002 and 3 months after the *M*6 earthquake in 2004. Similarly, the *S* wave arrived with a 85 ms delay in 2004, with traveltime of ~6.8 s, so the *S* wave velocity decreased by ~1.25%. Trapped waves in window 3 with longer travel times had larger time advances than *P* and *S* waves, again resulting in ~1.25% increase in velocity within the rupture zone. In contrast, the *S*-wave velocity decreased by ~0.5% in the surrounding rocks. Based on the width of the zone exhibiting larger traveltime increases between 2002 and 2004, we estimate that the zone which experienced fracturing and damage during the *M*6 mainshock, is about ~150-200 m wide in the top few kilometers. The width of this zone is consistent with the low-velocity waveguide on the San Andreas fault delineated using fault-zone trapped waves at the same array site in our previous experiment at Parkfield in 2002 (Li *et al.*, 2004), suggesting the width of fault zone is stable while velocities within it change over time. We examine in greater detail the width of the low-velocity waveguide after the 2004 *M*6 event using guided waves in a future study. Assuming that there was no significant change in seismic velocity between October 16, 2002 and September 28, 2004 at Parkfield region, the measured velocity decreases between 2002 and 2004 are most likely caused by the co-seismic rock damage with cracks opening due to the latest *M*6 Parkfield earthquake. Although processes associated with aseismic transients have shown to influence wave propagation (Niu *et al.*, 2003), however, there were no such transients and resolvable measurements in seismic velocity in Parkfield area during this time period (Rubinstein and Beroza, 2005). We note that the damage zone is not symmetric with the main fault trace but is broader on the southwest side. Also note that the velocity decreases on the north fault strand were smaller than those within the damage zone on the main fault but larger than the background velocity changes in surrounding rocks. In our previous study of fault-zone structure at Parkfield, we have delineated a distinct low-velocity waveguide on the main fault and a waveguide with smaller velocity reduction on the north strand at this site. The north strand might have experienced minor breaks due to secondary slip and strong shaking from ruptures on the main fault in the 2004 *M*6 earthquake.

The observed velocity decrease within the fault zone may be interpreted as dilatancy (Nur, 1972). Estimates of the change in velocity due to the change in the density of cracks may be calculated using equations in which the elastic constants of fractured rock are functions of the crack density (O'Connell and Budiansky, 1974). We assume randomly oriented cracks, and compute the change in apparent crack density from measured changes in seismic velocity. The apparent crack density is defined by $\varepsilon = N(a^3)/V$, where a is the radius of the flat penny-shaped crack and N is the number of cracks in a volume V. We assume cracks to be partially-water filled, and estimate that Poisson's ratio is 0.33. For the calculation, we use an average Vp = 3.0 km/s and Vs = 1.5 km/s for the fault-zone rocks at depths above ~5 km (*Li et al.*, 2004). Calculations reveal that the apparent crack density within the fault zone increased by ~0.018 in accordance with ~1.25% decrease in *S* velocity due to ~2.5% decrease in shear rigidity of the fault-zone rock during the time period between two repeated shots.

If observed changes in seismic velocity are modeled by fluid-filled cracks, then the degree of fluid saturation in cracks can be estimated from the ratio of changes in traveltime of *P*-waves to *S*-waves ($\Delta tp/\Delta ts$) because *S*-wave velocity does not depend as strongly as *P*-wave velocity on the amount of water in cracks. We have estimated water saturation degrees within low-velocity zones along ruptures in the 1992 Landers and 1999 Hector Mine earthquakes using this method (Li *et al.*, 1998; 2003). According to equations for the elastic moduli of the medium with isotropically oriented penny-shaped cracks (Garbin and Knopoff, 1975), the ratio of traveltime changes of *P* to *S* waves ($\Delta tp/\Delta ts$) in a Poisson solid is ~1.22 for dry cracks, and ~0.27 for water-saturated cracks (Li *et al.*, 2003). More precisely, in our study area where the *P* wave velocity is about twice the *S* wave velocity, the rock has an anomalous Poisson's ratio of 0.33 (see details in the discussion section). In this medium, $\Delta tp/\Delta ts$ is predicted to be 1.64 for dry cracks and 0.17 for water-saturated cracks. Figure 3d shows the $\Delta tp/\Delta ts$ values at array A across the SAF for repeated shot PMM in 2002 and 2004. The value of $\Delta tp/\Delta ts$ is ~0.57 within the fault zone and ~0.65 out of the zone, indicating more water included in cracks within the fault zone at shallow depth. The initial saturation degree of water in cracks before the mainshock is not predicted because no traveltime changes for *P* to *S* waves ($\Delta tp/\Delta ts$) before the 2004 *M*6 earthquake are available.

2. Repeated Aftershocks

Using the catalog of Northern California Seismic Network (Nadeau, personal communication), we selected 21 clusters of repeated aftershocks among ~1000 aftershocks recorded at our seismic array in 3 months starting a week after the 2004 *M*6 earthquake. Each cluster includes at least 5 repeated aftershocks occurring at the same place with the location difference among them smaller than 200 m and the difference in magnitude smaller than 0.5. The location precision of Parkfield earthquakes in the catalog is less than a few tens of meters in relative distance. The repeated aftershocks in each cluster show similar waveforms with correlation coefficient higher than 0.8. We found a total of about ~130 such repeated aftershocks in 21 clusters located at depths between ~3 km and ~9 km along the ~25-km-long rupture zone of the 2004 *M*6 earthquake (Fig. 1b). We examined these repeated aftershocks to determine seismic velocity changes with time after the mainshock. It is noted that we lack of data in the first week after the mainshock.

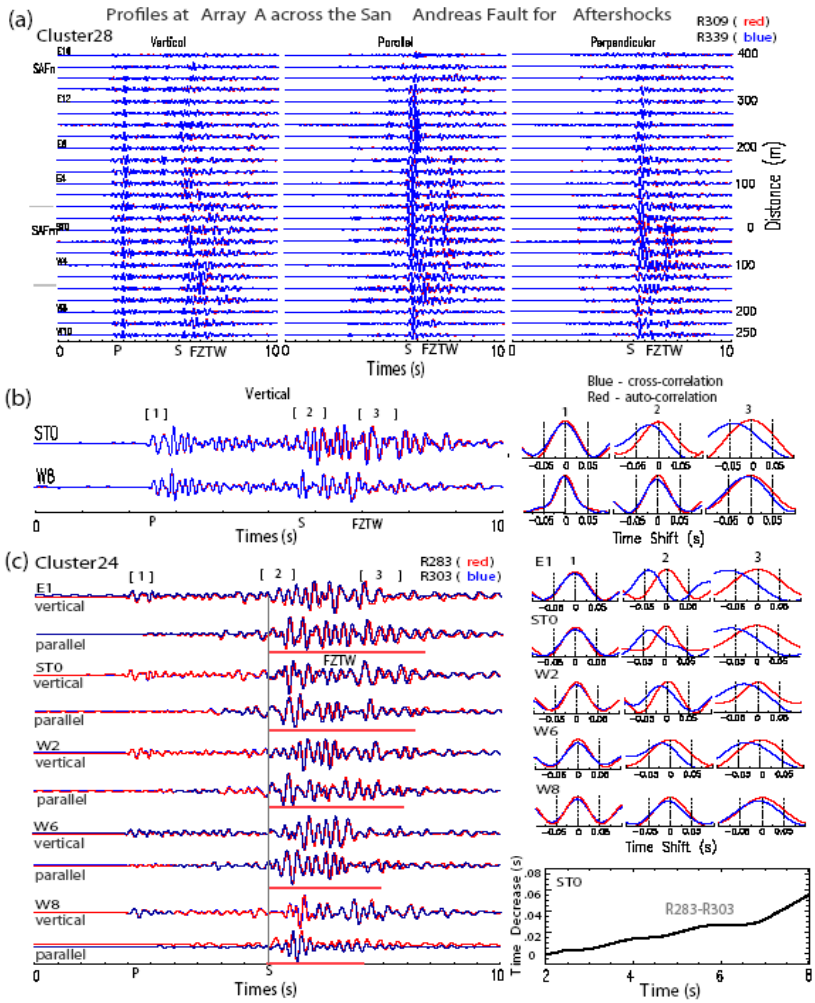

Figure 4. (a) Three-component seismograms recorded at array A across the SAF for two repeated aftershocks in cluster 28, occurring on 4 November (Julian date R309) and on 3 December (R339) 2004. Seismograms have been low-pass (<8-Hz) filtered and are trace-normalized in plot. Similar waveforms were recorded at array A for repeated aftershocks. Other notations are the same as in Figure 2. (b) Overlaid seismograms and waveform cross-correlations at stations ST0 and W8 located within and 200 m away from the fault for the repeated aftershocks. The first P arrivals for two events are aligned at the same time in the plot. S waves from the later event travel faster than the early event, with much larger time advance within the fault zone, indicating that the fault has been healing with rigidity recovery after the M 6.0 mainshock. (c) Overlapped vertical and parallel-to-fault component seismograms at five stations of array A for two repeated aftershocks in cluster 24 occurring on 9 (R283) and 29 (R303) October 2004. The first P arrivals for two events are aligned at the same time in plot. Horizontal bars denote the length of fault-zone-trapped wavetrains, showing longer trapped wavetrains following S waves at stations within the fault zone. Cross-correlations of vertical-component seismograms in three time windows at five stations, and moving-window cross-correlation of waveforms at station ST0 for two repeated aftershocks show that waves traveled faster for the later event and with larger advances at stations within the fault zone.

For example, Figure 4a shows similar seismograms recorded at array A across the SAF for a pair of repeated aftershocks in cluster 28 at 6.9 km depth and 2 km northwest of the array site, occurring on November 4 and December 3 of 2004. Prominent fault-zone guided waves with long-duration wavetrains appeared at stations close to the main fault trace in a width range of ~150 m. The time-expanded seismograms in Figure 4b shows that seismic waves from the later event traveled faster than those from the earlier event with larger traveltime advances at station STO on the main fault than those at station W8 200 m away from the fault. Waveform cross-correlations show that traveltime advances of *S* and guided waves from the later aftershock arriving at station ST0 are 25 ms and 38 ms plus the undetermined change in *P* traveltime, but much smaller at station W8. These observations indicate that the fault zone has been healing such that the rigidity recovers with time, most likely due to the closure of cracks that opened in the-*M*6 earthquake. In Figure 4c, we display seismograms at 5 stations of array A for a pair of repeated aftershocks in cluster 24 at 6.4 km depth and ~2 km northwest of the array, occurring on October 9 and 29. Note that fault-zone guided waves show longer wavetrains after *S*-waves at stations within the rupture zone than those farther away from the fault. Waveform cross-correlations exhibit traveltime advances

for the later event with larger changes at stations within the rupture zone. The moving window cross-correlation of seismograms at station ST0 for repeated aftershocks shows progressive increase in traveltime advance from 32 ms to 55 ms for *S* and guided waves, reflecting that seismic velocities have increased within the fault zone after the mainshock. Traveltime advances of seismic waves between October 9 and 29 measured in this example are larger than those between November 4 and December 3 shown in Fig. 4b although the time span between repeated events in each example and the travel distance from these events are similar (Fig. 1b), indicating that seismic velocities increased more rapidly in the earliest stage after the mainshock.

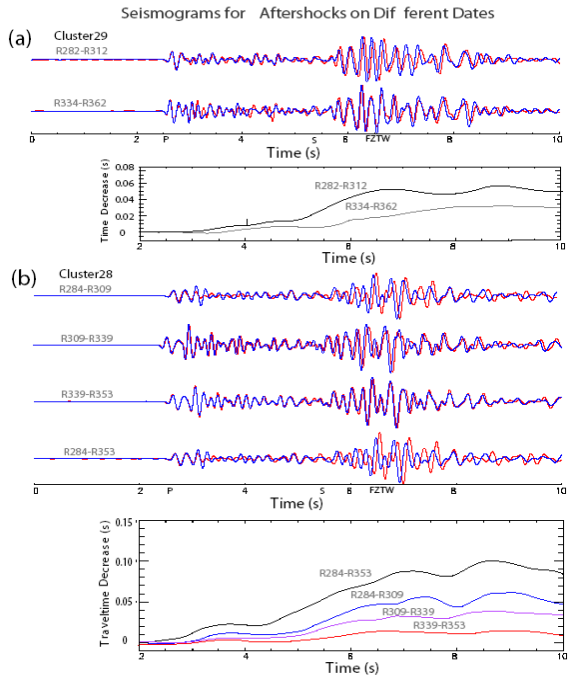

Figure 5. (a) Vertical-component seismograms recorded at station W4 of array A for four repeated aftershocks in cluster 29, occurring on 7 October (R282), 7 November (R312), 28 November (R334), and 26 December (R362) 2004. Seismograms have been low-pass (<8-Hz) filtered and are plotted in gray and black lines for the earlier and later events in each pair. Moving-window cross-correlations of waveforms show that the travel-time advance in the first pair of repeated aftershocks is larger than that in the second pair of aftershocks. The time spans in the two pairs are the same, indicating that the healing rate was larger in the earlier stage after the mainshock. (b) Same results from a sequence of four repeated aftershocks in cluster 28, occurring on 10 October (R284), 4 November (R309), 3 December (R339), and 17 December (R353), show greater travel-time advance in the earlier stage of the postseismic fault-healing process.

The trend of healing rate decreasing with time is shown in more detail by the examples given below. Figure 5a exhibits seismograms recorded at station W4 of array A for 4 repeated aftershocks in cluster 29 at 6.5 km depth and ~2 km northwest of the array, showing very similar waveforms with the correlation coefficient higher than 0.9 (Fig. 5a). Traveltime advances measured by moving window cross-correlation for the first pair of repeated events occurring on October 7 and November 7 are ~30-50 ms for *S* and guided waves in traveltime plus the change in *P* traveltime, nearly twice as large as those for the second pair of repeated events occurring on November 28 and December 26. Figure 5b exhibits seismograms and moving window cross-correlations of waveforms recorded at station W4 for 4 repeated aftershocks in cluster 28, occurring on October 10, November 4, December 3 and 17 in 2004. The relative decreases in traveltime for these waves were measured to ~30-50 ms in the first month, ~20-30 ms in the second month and less than ~15 ms in the third month after the mainshock, indicating that post-seismic fault healing rate is not constant but decreased with time. However, the healing is still observable 3 months after the mainshock, but the healing rate reduced to a third of that seen in the first month.

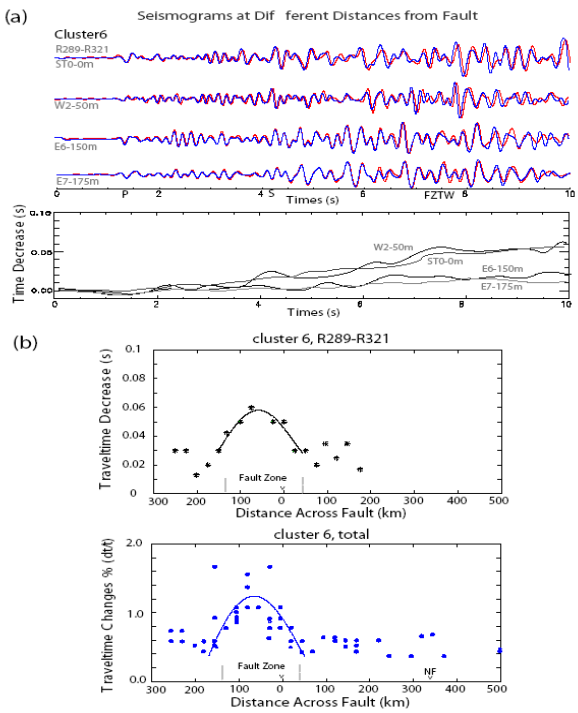

Figure 6. (a) Vertical-component seismograms recorded at four stations of array A for two repeated aftershocks in cluster 6, occurring on 15 October (R289) and 16 November (R3210). Other notations are the same as in Figure 5. Moving-window cross-correlations show that travel-time advances are larger at stations close to the fault and much smaller at stations located 150–175 m east of the fault. (b) Travel-time decreases of S waves measured by waveform cross-correlations at array A for these two repeated aftershocks show larger travel-time advances within the fault zone in a width range of ~200 m, indicating the larger healing rate in the rupture zone where the rock experienced greater damage in the 2004 M 6.0 earthquake. Note that this zone is not symmetric with the main fault trace, but broader on the southwest side of the main fault trace. (c) Travel-time advances, in percent, for S waves measured from waveform cross-correlations at array A for all available pairs of six repeated aftershocks in cluster 6, occurring on Julian dates 289, 299, 308, 321, 332, and 354 in 2004. The data have been adjusted for changes in travel times for P waves in a Poisson's solid. Results show larger travel-time advance (velocity increase) after the main-shock within the fault zone. The measurements of travel times for each pair of repeated aftershocks have been normalized to a time period of 20 days. NF, the north fault strand.

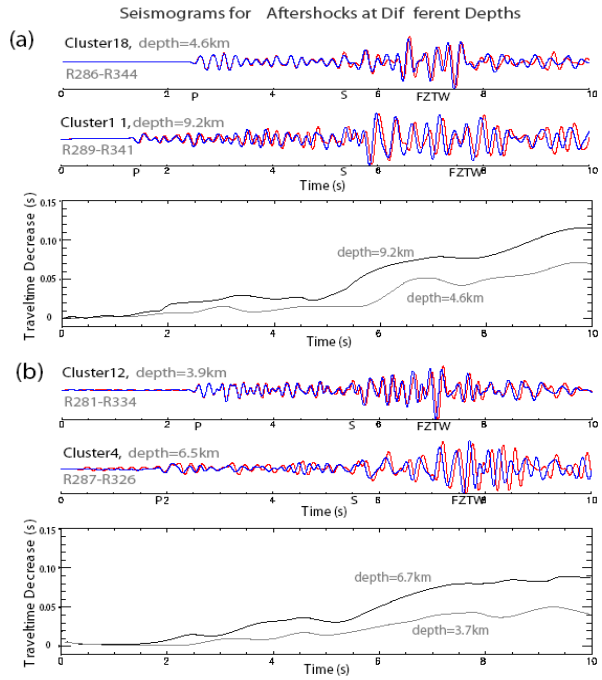

Figure 7. (a) Vertical-component seismograms recorded at station W4 of array A for two repeated aftershocks in cluster 18 at 4.6 km depth and another two repeated events in cluster 11 at 9.2 km depth. Other notations are the same as in Figure 5. Moving-window waveform cross-correlations show that the travel-time decreases for the pair of deeper aftershocks are larger than those for the pair of shallower events, although time spans between the repeated events in two pairs are nearly the same. (b) Vertical-component seismograms and moving-window waveform cross-correlations at station W4 of array A for two repeated aftershocks in cluster 12 at 3.7 km depth and another two repeated events in cluster 4 at 6.5 km depth, showing larger travel-time decreases for the pair of deeper aftershocks. These observations suggest that the healing occurred on the SAF, likely across seismic depths to ~9 km, although with smaller healing magnitude within the deeper portion of the fault zone.

The following examples show variations in traveltime change across the fault zone. Figure 6a exhibits seismograms recorded at 4 stations of array A for two repeated aftershocks in cluster 6 at 3.9 km depth and ~8 km northwest of the array site, occurring on October 15 and November 16 of 2004. Moving window cross-correlations show ~40-55 ms advance in traveltimes of *S* and guided waves to stations ST0 and W2 within the fault zone, larger than those (~10-20 ms) to stations E6 and E7 located at 150-175 m northeast of the fault. In Figure 6b, we display the relative changes in traveltime of *S* waves and guided waves at all available stations of array A measured by moving window cross-correlations for these two repeated aftershocks, showing larger traveltime decrease at stations within the fault zone. Figure 6c exhibits the traveltime changes in percentage for *S* and guided waves at all working stations of array A for 6 repeated aftershocks in cluster 6 occurring between October 15 and December 15, 2004. Traveltimes for *S* and guided waves decreased by ~1.1% within the rupture zone in this time period, but with a smaller change (~0.5%) out of the zone. Note that the traveltime decreases at stations near the north fault strand were slightly larger than the background level in surrounding rocks. These observations indicate that the rocks damaged in the 2004 *M*6 earthquake have been healing with larger healing magnitude within the rupture zone than in surrounding rocks.

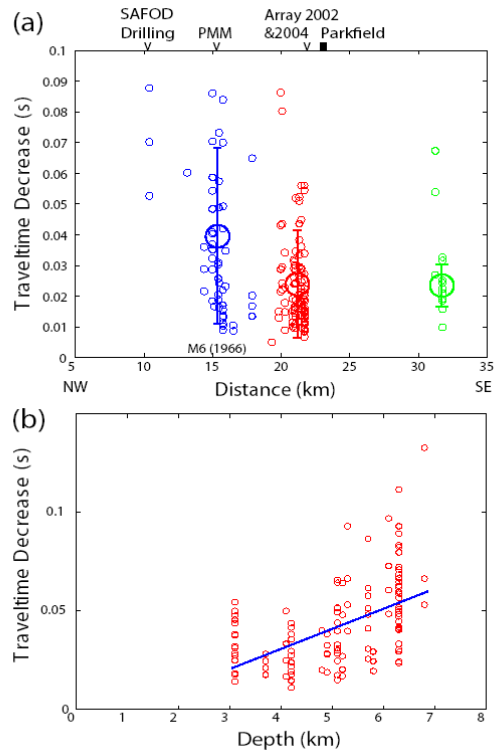

Figure 8. Travel-time decreases measured at nine stations W5–E3 located within the fault zone for 226 pairs of repeated aftershocks in 21 clusters, with the first event in each pair occurring before 26 October (R300) and the second event occurring at least 20 days later than the first event. The measured time decreases for each pair of repeated aftershocks have been normalized to the changes in 20 days. The mean values and standard deviations of the data for three groups of clusters labeled 1, 2, and 3 are marked by large circles and error bars. Group 1 is located close to the hypocenter of the 1966 M 6.0 earthquake. The data have been normalized to a depth range of 4 km to remove the effect of different depths of pairs on measurements. Aftershocks in group 1 occurring on or close to the slip patch of the M 6.0 earthquake in 1966 show larger travel-time decreases, although three groups of clusters are nearly at the same average depth. (b) The data used in (a) are plotted versus depths of repeated aftershocks. The straight line is the least squares fit to the data, showing that the accumulated travel-time advance increases as the event depth increases between depths of 3 km and 7 km. The results suggest that the fault experienced healing after the 2004 M 6.0 Parkfield earthquake at seismogenic depths to ~7 km, although the magnitude of healing is smaller in the deeper portion of fault zone.

We then examined the data for variations in traveltime change along the fault strike and with depth. Figure 7a exhibits the seismograms recorded at station W4 of array A for 2 repeated aftershocks in cluster 18 occurring at 4.6 km depth on October 11 and December 8, and other 2 repeated events in cluster 11 occurring at 9.2 km depth on October 14 and December 5. Moving window waveform cross-correlations show that traveltimes of *S* and guided waves were decreased by ~50-

80 ms plus changes in *P*-waves for the pair of deeper repeated aftershocks, but by ~30-50 ms for the pair of shallower events, although the time span of repeated events in the two pairs are nearly the same. In Figure 7b, we exhibit seismograms recorded at station W4 for 2 repeated aftershocks in cluster 12 occurring at 3.7 km depth on October 7 and November 29, and other 2 repeated aftershocks in cluster 4 at 6.5 km on October 13 and November 20. Again, we see larger traveltime decreases for the pair of deeper repeated events. These observations suggest that the post-mainshock healing occurred on the ruptured fault to a depth of at least 6-7 km, probably across the seismogenic depths but with smaller healing magnitude in the deeper portion of the fault zone. The increasing pressure with increasing depth will reduce the crack density and probably increase the rate of healing of damage caused by earthquakes. It is also likely to influence the development of fault gouge (Scholz, 1990; Marone, 1998) and the mineralogy of the rocks (Angevine *et al*, 1982). Thus, the fault-zone properties are dependent on depth.

In summary, Figure 8 shows relative decreases in traveltime for *S* and guided waves at 9 stations between W5 and E3 located in a range of 200 m across the fault for 226 pairs of repeated aftershocks in 21 clusters measured by an automatic computer procedure for moving window cross-correlation. The catalog includes more pairs of repeated aftershocks in the 21 clusters, but parts of them were not recorded at some stations of array A because of battery problems. Also, some repeated aftershocks with correlation coefficients lower than 0.7 are not used for computation. We used the data from repeated aftershocks with the first event occurring before October 26 (R300) and the second event occurred at least 20 days after the first event in the pair. The measured decreases in traveltime for pairs with longer time span between repeated aftershocks are normalized to the change in 20 days. Figure 8a shows measured relative traveltime decreases for *S* waves from these repeated aftershocks as a function of position along the fault strike. Although the data are scattered, the repeated aftershocks in group *1* located close to the hypocenter of the *M*6 earthquake in 1966 beneath Middle Mountain show relatively large changes in traveltime although the average depths of the 3 groups of clustered aftershocks used in this plot are nearly the same. Langbein *et al.* (2005) surveyed surface rupture and post mainshock surface slip after the 2004 September 28 *M*6 Parkfield earthquake. They found the greatest dextral slip of 44 mm in the Middle Mountain area. The preliminary results from inverse of GPS and broadband waveform data show the maximum slips of ~0.6 m at depths of 4-6 km beneath Middle Mountain. Figure 8b shows traveltime decrease for these repeated aftershocks versus event depths. We see an increasing trend of cumulative traveltime changes as the depth increases from 3 km to 7 km although the data are scattered.

DISCUSSION AND CONCLUSION

Our seismic study at Parkfield indicates that the active fault zone, which undergoes strong dynamic stresses and pervasive cracking during a major earthquake, has a distinct low-velocity zone that co-seismically weakens and consequently heals. We have used fault-zone trapped waves to delineate a ~150-m-wide low-velocity damage zone on the San Andreas fault at Parkfield, in which seismic velocities are reduced by 25-40% from wall-rock velocities (Li *et al.*, 2004). Although this damage zone along the fault strike has accumulated over geological time, it was in part weakened by the latest *M*6 Parkfield earthquake in 2004 possibly due to inelastic deformation around the propagating crack tip in the 2004 *M*6 mainshock, as predicted by existing fault-zone rupture models (e.g., Rice, 1980; Scholz, 1990).

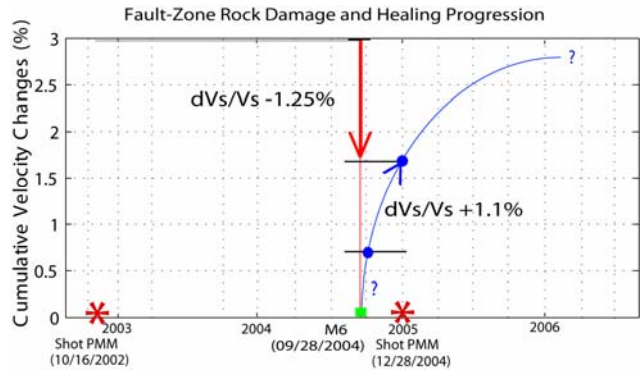

Figure 9. *S*-wave velocity changes within the rupture zone on the SAF associated with the M 6.0 Park-field earthquake on 28 September 2004. The S velocity decreased by ~1.25% in the time period between the two repeated shots on 16 October 2002 and 28 December 2004, most likely due to the coseismic rock damage during this M 6.0 mainshock. The velocity within the rupture zone then increased by ~1.1% in 3 months starting a week after the mainshock, showing postmainshock fault healing with rigidity recovery of damaged rocks within the fault zone. The healing rate is not constant but decreases with time, although details just after the existing data and extrapolation into the future are not well constrained. The velocity changes in the first week after the main-shock were not measured in this study.

The data acquired in our recent experiments at Parkfield provide details of co-seismic damage and post-mainshock healing on the San Andreas fault associated with the 2004 *M*6 earthquake. In summary, Figure 9a shows seismic velocity changes measured at our seismic arrays deployed at Parkfield before and after this earthquake. Our measurements for repeated shots on October 16 of 2002 and December 30 of 2004 show a decrease of ~1.25% in shear wave velocity within the fault zone, most likely due to rock damage with crack opening caused by dynamic rupture in the *M*6 earthquake on September 28 of 2004, assuming that there was no significant changes in seismic velocity at Parkfield area in the time period between the shot in 2002 and the 2004 *M*6 earthquake (Rubinstein and Beroza, 2005). The water table change will affect the seismic velocity at shallow depth. As we carried out repeated experiments in the fall of 2002 and 2004, there would be not significant variations in water table in the same season at Parkfield. It is reasonable to attribute the observed velocity changes to the 2004 *M*6 event. Measurements for repeated aftershocks show the velocity increased by ~1.1% within the rupture zone during 3 months starting a week after the mainshock, reflecting the damaged rocks healing, most likely due to the closure of cracks that had opened during the latest *M*6 Parkfield earthquake in 2004. The healing rate is not constant but decreases with time (Fig. 5). It suggests that a fault may regain strength rapidly in the early stage in the post-mainshock period, but may take a reasonable long time to fully recover the strength for the next earthquake on it.

Healing varies across the fault zone with largest healing occurring within a ~200-m wide zone (Fig. 6) that likely experienced greater damage in the mainshock. This damage zone is asymmetric, broader on the southwest side of the main fault trace. The asymmetry may imply that the fault zone has a significant cumulative damage due to previous large earthquakes on the SAF. When a fault ruptures, it may preferentially damage the already weakened rocks in the zone, even though those rocks are not symmetrically distributed on either side of the main slip plane (Chester et al., 1993). Recent results from the SAFOD drilling project and borehole logs at Parkfield show high porosity and multiple slip planes in an ~200-m-wide low-velocity zone with velocity reduction of ~25% on the SAF at ~3.2 km depth (Hickman *et al.*, 2005).

We observed variations in the magnitude of fault healing along fault strike and with depth. Larger decreases in traveltime (larger increase in seismic wave velocity) were measured for repeated aftershocks occurring beneath Middle Mountain (Fig. 8) where the maximum slips were found in the 2004 Parkfield *M*6 earthquake. The traveltime changes increase with focal depth of aftershocks at between 3 km and 7 km depth, indicating that healing occurs on the fault to at least ~7 km depth. Because we have only captured healing for one cluster of repeated aftershocks at depth below ~7 km in this study, we lack constraints on the healing magnitude for the deeper portion of the fault zone. However, the repeated events in cluster 11 at the depth of ~9.2 km also shows larger time delays than those at shallower depths (Fig. 7).

The net co-seismic decrease in shear wave velocity within the fault zone at depths above ~7 km caused by this *M*6 event is thus estimated to be at least ~2.5%, accounting for the measurements of traveltime increase (seismic velocity decrease) of ~1.25% for repeated shots in the fall of 2002 and the December 28 of 2004, and traveltime decrease (velocity increase) of ~1.1% for repeated aftershocks in 3 months starting a week after the mainshock on September 28, 2004. In contrast, the changes in shear velocity in surrounding rocks were smaller than ~0.5%. Because we have no data at array site in the first week after the mainshock, we do not have information about the earliest stage of fault healing. However, Rubinstein and Beroza (2005) observed significant traveltime delays caused by the 2004 *M*6 Parkfield earthquake at the seismic network stations for repeated earthquakes occurring at depths of ~3 km near the SAFOD drilling site before and after the 2004 *M*6 earthquake. They measured traveltime decreases exceeding ~25 ms in *S* coda for the repeated SAFOD target events occurring on October 21 and 23, 2003, approximately one year before the *M*6 earthquake and on September 28 0f 2004 immediately after the mainshock at borehole station PMM of Parkfield Seismic Network (Fig. 1a), located ~200 m from the SAF main trace at ~5 km southwest of the SAFOD site. They also observed direct *S*-wave traveltime delays up to 7 ms to many of the surface stations but much smaller delays at borehole stations in the Parkfield area. They attribute the time delays to cracks opened during the strong shaking of the *M*6 Parkfield earthquake at depths shallower than 100-300 m. Crack opening is likely favored at shallow depths with soft rock and lower confining crustal stress in a broad distance range from the epicenter due to strong ground motion. However, stations of our dense array were located much closer to the fault than network stations. The data presented here from the shots and aftershocks located on or close to the fault mainly document the changes within the fault zone rather than the changes in surrounding rocks. We interpret the observed velocity decrease within the fault zone as mainly due to crack opening caused by the dynamic rupture of the latest *M*6 earthquake. Shaking-induced weakening may also effect the rupture propagation because the pre-existing weak, low impedance fault zone is susceptible to damage (Fialko et al., 2002; Vidale and Li, 2003). Calculation for a ~2.5% decrease in velocity revealed that the apparent crack density within the rupture zone increased by ~0.035, which caused ~5% decrease in shear rigidity of the fault-zone rock during dynamic rupture of the 2004 *M*6 Parkfield earthquake. The subsequent 1.1% increase in *S* velocity during 3 months starting a week after the mainshock suggests the apparent crack density within the rupture zone decreased by 0.016, causing a ~2.2% increase in shear rigidity of the fault-zone rock during the early post-mainshock period.

During the fault healing, the reduction of crack density may be controlled by a combination of mechanical and chemical processes on the active fault. Fault healing may be affected by time-dependent frictional strengthening (Vidale *et al.*, 1994; Marone, 1998; Schaff and Beroza, 2004), rheological fluid variations or changes in the state of stress (Blanpied *et al.*, 1992; Peltzer *et al.*, 1998; Dodge and Beroza, 1997), cementation, recrystallization, pressure solution, crack sealing and grain contact welding (Hickman and Evans, 1992; Olsen *et al.*, 1998; Sleep *et al.*, 2000) and the fault-normal compaction of the rupture zone (Massonnet *et al.*, 1996; Boettcher and Marone, 2004) as well as chemical healing from mineralogical lithification of gouge materials over longer time period at seismogenic depth (Angevine *et al.*, 1982). In addition, the 'crack dilatancy' mechanisms (Nur, 1972) associated with the earthquake are likely to operate for co-seismic fault damage and post-mainshock healing even if other processes are active too. The stress-related temporal changes in seismic velocity caused by the 1989 Loma Prieta, California earthquake have been reported (Dodge and Beroza, 1997; Schaff and Beroza, 2004). Baisch and Bokelmann (2002) suggest that coseismic deformation caused by this earthquake might lead to crack opening either by localizations of shear stress or by elevated pore fluid pressure. Concentrated deformation at low-strength fault zones may help to cause damage. After the earthquake, relaxational processes, such as crack healing, fluid diffusion, and post-seismic deformation caused the cracks to close again that can be approximated by a logarithmic recovery rate. As rocks heal, a contribution can be from either continued right-lateral deformation due to the regional stress field that dominated the coseismic displacements or fault-normal compression owing to a reduction in crack volume. The variation in apparent crack density inferred by seismic velocity measurements reflects changes in either crack volume or rearrangement of aspect ratio caused by the earthquake.

We conclude that cracks that opened during the mainshock closed soon thereafter. This consistent with our interpretation of the soft low-velocity fault-zone waveguide on the SAF as being at least partially weakened in the 2004 *M*6 mainshock, but with possible significant cumulative effects as well.

The temporal changes in crack-induced anisotropy near the Nojima fault that ruptured in the 1995 *M*7.1 Kobe earthquake have been observed in shear-wave splitting (Tadokoro *et al.*, 1999; Ikuta and Yamaota, 2004). However, there was no clear change in shear-wave splitting anisotropy after the 1999 Hector Mine earthquake, California (Cochran *et al.*, 2003). In addition, Cochran *et al* (2005) also observed no clear changes in shear-wave splitting parameters along the SAF associated with the 2004 Parkfield earthquake using some of the same seismic array data as presented here, suggesting that the shear-wave splitting may be not sensitive to detect small changes in crack density because the velocity change influences both the fast and slow orthogonally-polarized shear waves. However, they see strong fault-parallel alignment in polarization direction of the fast *S* wave within a 100-200 m wide zone along strike of the SAF that overlaps with the region of greatest velocity reductions reported here.

We also note that the ratio of traveltime changes for *P* to *S* waves is 0.57 within the rupture zone and ~0.65 in the surrounding rocks (Fig. 3d), suggesting that cracks within the fault zone are more wet than those out of the zone at shallow depths according to equations for the elastic moduli of the medium with cracks (Garbin and Knopoff, 1975). This may be due to the higher permeability owing to higher porosity within the damaged fault zone than in the surrounding rocks, even though every crack includes a similar fraction of fluids. High permeability and low strength have been measured in a damage zone centered at the main trace of the Nojima fault in the 1995 Kobe earthquake (Lockner *et al*., 2000). High pressure-water is coming up from depth and the highly fractured fault-zone acts as a fluid channel.

Our observations of fault zone damage and healing associated with the latest *M*6 Parkfield earthquake are in general consistent with the model of velocity as a function of time owing to damage and healing for Lander and Hector Mine earthquakes (Vidale and Li, 2003). However, the magnitude of damage and healing observed on the SAF is smaller than those on the Landers and Hector Mine rupture zones, probably related to the magnitudes of earthquake, slip, stress drop, pore-pressure, and rock type.

Acknowledgments

This study was supported by NSF/EarthScope Grant EAR-0342277, USGS Grant NEHRP20060160, and partially by the SCEC. Special thanks to S. Hickman, W. Ellsworth, and M. Zoback of SAFOD PIs for their coordination in our experiments for seismic characterization of the SAFOD drilling. We acknowledge J. Varian, G. Varian, G. Work, and B. Mosby for permissions to conduct our experiment on their lands, and the IRIS for the use of PASSCAL instruments. We are grateful to P. Malin, C. Thurber, S. Roecker, M. Rymer, R. Catchings, A. Snyder, R. Russell, L. Powell, B. Nadeau, N. Boness, D. McPhee, and F. Niu for their collaborations in our research at Parkfield. We thank Associated Editor Ramon Arrowsmith, reviewer Norm Sleep and an anonymous reviewer for their helpful suggestions and comments on the manuscript. This research was supported by the Southern California Earthquake Center. SCEC is funded by NSF Cooperative Agreement EAR-0106924 and USGS Cooperative Agreement 02HQAG0008. The SCEC contribution number for this paper is 924.

References

Aki, K., Asperities, barriers, characteristic earthquakes, and strong motion prediction (1984). *J. Geophys. Res*. **89**, 5867-5872.

Angevine, C. L., D. L., Turcotte, and M. D. Furnish (1982). Pressure solution lithification as a mechanism for the stick-slip behavior of faults, *Tectonics*, **1**, 151-160.

Blanpied, M. L., D. A. Lockner, and J. D. Byerlee (1992). An earthquake mechanism based on rapid sealing of faults, *Nature*, **359**, 574-576.

Boettcher, M, S., and C. Marone (2004). Effects of normal stress variation on the strength and stability of creeping faults, *J. Geophys. Res.* **109**, B03406, dioi:10.1029/2003JB002824.

Baisch. S, and G. H. R. Bokelmann (2001). Seismic waveform attributes before and after the Loma Prieta earthquake: scattering change near the earthquake and temporal recovery, *J. Geophys. Res*. **106**, 16,323-16,337.

Byerlee, J., Friction, overpressure and fault-normal compression (1990). *Geophys. Res. Lett*. **17**, 2109-2112.

Chester F. M., J. P. Evans, and R. L. Biegel (1993). Internal structure and weakening mechanisms of the San Andreas fault, *J. Geophys. Res*. **98**, 771-786.

Cochran, S. E., J. E. Vidale, and Y. G. Li (2003). Near-fault anisotropy following the Hector Mine earthquake, *J. Geophys. Res*. **108**, B9, 2436-2447, ESE 11.

Cochran, S. E., Y. G. Li, and J. E. Vidale (2005). Anisotropy in the shallow crust observed around the San Andreas Fault before and after the 2004 M6 Parkfield earthquake, *Bull. Seism. Soc. Am.*, this issue.

Dieterich, J. H. (1978). Time-dependent friction and the mechanics of strike-slip. *Pure Appl. Geophys*., **116**, 790-806.

Dodge, D., and G. C. Beroza (1997). Source array analysis of coda waves near the 1989 Loma Prieta, California mainshock: Implications for the mechanism of coseismic velocity changes, *J. Geophys. Res.* **102**, 24,437-24,458.

Eberhart-Phillips, D., and A. J. Michael (1993). Three-dimensional velocity structure, seismicity, and fault structure in Parkfield region, central California *J. Geophys. Res.* **98**, 15737-15758.

Fialko, Y., D. Sandwell, D. Agnew, M. Simons, P. Shearer, B. Minster (2002). Deformations on nearby faults induced by the 1999 Hector Mine earthquake, *Science*, **297**, 1858-1862.

Garbin, H. D., and L. Knopoff (1975). Elastic moduli of a medium with liquid-filled cracks, *Quart. Appl. Math. October*, **32**, 301-303.

Hickman, S. H., and B. Evans (1992). Growth of grain contacts in halite by solution-transfer: Implications for diagenesis, lithification, and strength recovery, in *Fault Mechanics and Transport Properties of Rocks*, pp. 253-280, Academic, San Diego, Calif.

Hickman, S. H., M. D. Zoback, and W. L. Ellsworth (2005). Structure and Composition of the San Andreas fault zone at Parkfield: Initial results from SAFOD Phase 1 and 2, *EOS, Transactions, American. Geophysics Union*, **83**, No.47, 237.

Ikuta, R., and K. Yamaoka (2004). Temporal variation in the shear wave anisotropy detected using the accurately controlled routinely operated signal system (ACROSS), *J. Geophys. Res.* **109**, B09305, doi:10.1029/2003JB002901.

Kanamori, H. (1994). Mechanics of earthquakes, *Ann. Rev. Earth Planet., Sci.*, **22**, 207-237.

Korneev, V. A., R. M. Nadeau, T. V. McEvilly (2003). Seismological studies at Parkfield IX: Fault-zone imaging using guided wave attenuation, *Bull. Seism. Soc. Am*. **80**, 1245-1271.

Langbein, J., R. Bocherdt, D. Dreger, J. Fletcher, J. L. Hardbeck, M. Hellweg, C. Ji, M. Johnston, J. R. Murray, R. Nadeau, M. J. Rymer, and J. A. Trieman (2005). Preliminary report on the 28 September 2004, M 6.0 Parkfield, California earthquake, *Seism. Res. Lett.* **76**, No. 1, 10-26.

Lees, J. M., and P. E. Malin (1990). Tomographic images of *P* wave velocity variation at Parkfield, California, *J. Geophys. Res.* **95**, 21,793-21,804.

Li, Y. G., P. C. Leary, K. Aki, and P. E. Malin (1990). Seismic trapped modes in Oroville and San Andreas fault zones, *Science*, **249**, 763-766.

Li, Y. G., W. L. Ellsworth, C. H. Thurber, P. E. Malin, and K. Aki (1997). Observations of fault-zone trapped waves excited by explosions at the San Andreas fault, central California, *Bull. Seism. Soc. Am.* **87**, 210-221.

Li, Y. G., J. E. Vidale, K. Aki, F. Xu, and T. Burdette (1998). Evidence of shallow fault zone strengthening after the 1992 *M*7.5 Landers, California, earthquake, *Science*, **279**, 217-219.

Li, Y. G. and J. E. Vidale (2001). Healing of the shallow fault zone from 1994-1998 after the 1992 *M*7.5 Landers, California, earthquake, *Geophys. Res. Lett.* **28**, 2999-3002.

Li, Y. G., J. E. Vidale, S. M. Day, D. D. Oglesby, and E. Cochran (2003). Post-seismic fault healing on the 1999 *M*7.1 Hector Mine, California earthquake, *Bull. Seism. Soc. Am*. **93**, 854-869.

Li, Y. G., J. E., Vidale, and S. E. Cochran (2004). Low-velocity damaged structure on the San Andreas fault at Parkfield from fault-zone trapped waves, *Geophys. Res. Lett.* **31**, L12S06, p1-5.

Lockner, D. A., H. Naka, H. Tanaka, H. Ito, and R. Ikeda (2000). Permeability and strength of core samples from the Nojima fault of the 1995 Kobe earthquake, *in Proceedings of the International Workshop on the Nojima Fault Core and Borehole Data Analysis*, Tsukuba, Japan, Nov 22-23, 1999, USGS Open file Report 00-129, edited by H. Ito, K. Fujimoto, H. Tanaka, and D. A. Lockner, 147-152.

Marone, C., J. E. Vidale, and W. L. Ellsworth (1995). Fault healing inferred from time dependent variations in source properties of repeating earthquakes, *Geophys. Res. Lett.* **22**, 3095-3098.

Marone, C. (1998). The effect of loading rate on static friction and the rate of fault healing during the earthquake cycle, *Nature*, **391**, 69-72.

Michelini, A., and T. V. McEvilly (1991). Seismological studies at Parkfield, I, Simultaneous inversion for velocity structure and hypocenters using cubic B-splines parameterization, *Bull. Seism. Soc. Am.* **81**, 524-552.

Massonnet, D, W. Thatcher, and H. Vadon (1996). Detection of postseismic fault-zone collapse following the Landers earthquake, *Nature*, **382**, 612-616.

Mooney, W. D., and A. Ginzburg (1986). Seismic measurements of the internal properties of fault zones, *Pure Appl. Geophys.* **124**, 141-157.

Niu F. L., P. G. Silver, R. M. Nadeau, and T. V. McEvilly (2003). Stress-induced migration of seismic scatters associated with 1993 Parkfield aseismic transient event, *Nature*, **426**, 544-548.

Nur. A., Dilatancy (1972). Pore fluid, and premonitory variations of ts/tp travel times, *Bull. Seismol. Soc. Am*. **62**, 1217-1222.

O'Connell, R. J., and B. Budiansky (1974). Seismic velocities in dry and saturated cracked solids, *J. Geophys. Res.* **79**, 5412-5426.

Olsen, M., C. H. Scholz, and A. Leger (1998). Healing and sealing of a simulated fault gouge under hydrothermal conditions for fault healing, *J. Geophys. Res.* **103**, 7421-7430.

Peltzer, G., P. Rosen, F. Rogez, and K. Hudnut (1998). Poroelastic rebound along the Landers 1992 earthquake surface rupture, *J. Geophys. Res.* **103**, 30131-30145.

Rice, J., R. (1980). The mechanics of earthquake rupture, In Physics of the Earth's Interior, A. M. Dziewonski and B. Boschi (Editors), North-Holland, Amsterdam, 555-649.

Rice, J. R. (1992). Fault stress states, pore pressure distributions, and the weakness of the San Andreas fault, in *Fault Mechanics and Transport Properties of Rocks*, edited by B. Evans and T.-F. Wong, pp. 475-503, Academic, San Diego, Calif.

Richardson, E., and C. Marone (1999), Effects of normal stress vibrations on frictional healing, *J. Geophys. Res*. **104**, 28,859-28,878.

Rubinstein, Justin, and G. C. Beroza (2005). Depth constrain on nonlinear strong ground motion from the 2004 Parkfield earthquake, submitted to *Seism. Res. Lett.* **32**, L14313, doi: 10.1029/2005GL023189.

Schaff, D. P., and G. C., Beroza (2004). Coseismic and postseismic velocity changes measured by repeating earthquakes, *J. Geophys. Res.* **109**, B10302, doi: 10.1029/2004JB003011.

Scholz, C. H. (1990). *The Mechanics of Earthquakes and Faulting*, Cambridge Univ. Press, New York.

Shalev, E., and P. E. Malin (2005). Fault-zone guided waves observations in the SAFOD drill hole, *EarthScope National Annual Meeting Proceedings*, **228**, April 2005.

Sibson, R. H. (1977). Fault rocks and fault mechanisms, *J. Geol. Soc. London*, **133**, 191-213.

Sleep, N. H., E. Richardson, and C. Marone (2000). Physics of friction and strain rate localization in synthetic fault gouge, *J. Geophys. Res*. **105**, 25,875-25,890.

Snieder, R. A., A. Gret, H. Douma, and J., Scales (2002). Coda wave interferometry for estimating nonlinear behavior in seismic velocity, *Science*, **295**, 2253-2255.

Tadokoro, K, M. Ando and Y. Umeda (1999). *S* wave splitting in the aftershock region of the 1995 Hyogo-ken Nanbu earthquake, *J. Geophys. Res*., **104**, 981-991. Thurber, C. H., S. Roecker, W. Ellsworth, Y. Chen, W. Lutter, and R. Sessions (1997). Two-dimensional seismic image of the San Andreas fault in the northern Gabilan Range, central California: Evidence for fluids in the fault zone, *Geophys. Res. Lett.* **24**, 1591-1594.

Thurber, C., S. Roecker, K. Roberts, M. Gold, L. Powell, and K. Rittger (2003). Earthquake location and three-dimensional fault zone structure along the creeping section of the San Andreas fault near Parkfield, CA: Preparing for SAFOD, *Geophys. Res. Lett*. **30**, 1112-1115.

Unsworth, M., P. Malin, G. Egbert, and J. Booker (1997). Internal structure of the San Andreas fault at Parkfield, CA, *Geology*, 356-362, 1997.

Vidale, J. E., W. L. Ellsworth, A. Cole, and C. Marone (1994). Rupture variation with recurrence interval in eighteen cycles of a small earthquake, *Nature*, **368**, 624-626.

Vidale, J. E. and Li, Y. G. (2003). Damage to the shallow Landers fault from the nearby Hector Mine earthquake, *Nature*, **421**, 524-526, 30 Jan.

Yasuhara, H., C. Marone, and D., Ellsworth (2004). Fault zone restrengthening and frictional healing: The role of pressure solution, *J. Geophys. Res*., in review.

Department of Earth Sciences
University of Southern California
Los Angeles, California 90089-0740
ygli@usc.edu
(Y.G.L., P.C.)

Institute of Geophysics and Planetary Physics
Scripps Institution of Oceanography
La Jolla, California, 92093-0225
(E.S.C.)

Institute of Geophysics and Planetary Physics
University of California, Los Angeles
Los Angeles, California 90095
(J.E.V.)

U.S. Geological Survey, MS 977
345 Middlefield Road
Menlo Park, California 94025
(T.B.)

Seismic Velocity Variations on the San Andreas Fault Caused by the 2004 *M*6 Parkfield Earthquake and Their Implications

Yong-Gang Li[1], Po Chen[1], Elizabeth S. Cochran[2], and John E. Vidale[2]

[1]*Department of Earth Sciences, University of Southern California, Los Angeles, California 90089-0740, USA*
[2]*Institute of Geophysics and Planetary Physics, University of California at Los Angeles, Los Angeles, California 90095, USA*

Repeated earthquakes and explosions recorded at the San Andreas fault near Parkfield before and after the 2004 *M*6 Parkfield earthquake show large seismic velocity variations within a ~200-m-wide zone along the fault to depths of ~6 km. The seismic arrays were co-sited in the two experiments, and located in the middle of a high-slip part of the surface rupture. Waveform cross-correlations of microearthquakes recorded in 2002 and subsequent repeated events recorded a week after the 2004 *M*6 mainshock show a peak ~2.5% decrease in seismic velocity at stations within the fault zone, most likely due to the co-seismic damage of fault-zone rocks during dynamic rupture of this earthquake. The damage zone is not symmetric, instead extending farther on the southwest side of the main fault trace. Seismic velocities within the fault zone measured for later repeated aftershocks in following 3-4 months show ~1.2% increase at seismogenic depths, indicating that the rock damaged in the mainshock recovers rigidity, or heals, through time. The healing rate was not constant but largest in the earliest stage of post-mainshock. The magnitude of fault damage and healing varies across and along the rupture zone, indicating that the greater damage was inflicted and thus greater healing is observed in regions with larger slip in the mainshock. Observations of rock damage during the mainshock and healing soon thereafter are consistent with our interpretation of the low-velocity waveguide on the SAF being at least partially softened in the 2004 *M*6 mainshock, with additional cumulative effects due to recurrent rupture.

Key words: Parkfield earthquake, temporal velocity variation, rock damage and healing.

1. Introduction

In order to relate present-day crustal stresses and fault motions to the geological structures formed by previous ruptures we must understand the evolution of fault systems on many spatial and time scales. Extensive research in the field, in laboratories and with numerical simulations have illuminated that the fault zone undergoes high, fluctuating stress and pervasive cracking during an earthquake (e.g., Aki, 1984; Mooney and Ginzburg, 1986; Scholz, 1990; Rice, 1992; Kanamori, 1994). Rupture models that involve variations in fault-zone fluid pressure over the earthquake cycle have been proposed (e.g., Dieterich, 1978; Blanpied *et al.*, 1992, 1998; Olsen *et al.*, 1998). Structural fault variations (e.g., Das and Aki, 1977; Rice, 1980) and rheological fault variations (e.g., Sibson, 1977; Angevine *et al.*, 1982) as well as variations in strength and stress may affect the earthquake rupture (e.g., Vidale *et al.*, 1994; Beroza, *et al.*, 1995). Karageorgi *et al.* (1997) and Korneev *et al.* (2000) detected and modeled traveltime changes in vibroseismograms in a localized region where the 1966 *M*6 Parkfield earthquake initiated. Parkfield, and attributed these variations to hydrological changes correlated with a significant pulse in fault slip and seismicity during 1987-1995. However, earthquake-related fault-zone damage and healing have been documented quantitatively in only a few cases (e.g. Marone *et al.*, 1995; Li *et al.*, 1998; Massonnet *et al.*, 1996; Yasuhara *et al.*, 2004). The origin of the spatial and temporal variability in the fault zone properties also remains a major mystery. Repeated seismic surveys using explosions along rupture zones of the 1992 *M*7.4 Landers and 1999 *M*7.1 Hector Mine, California earthquakes (Li and Vidale, 2001; Li *et al.*, 2003; Vidale and Li, 2003) showed that seismic velocities within the shallow part of the fault zone increased by a few percent in 1 to 6 years after the mainshocks, most likely due to the closure of partially fluid-filled cracks that opened during the mainshocks. These observations illuminate a conceptual framework of fault-zone damage and healing progression associated with major earthquakes.

The low-velocity and low-resistivity zone on the SAF near Parkfield has been revealed by many researchers (e.g., Lees and Malin, 1990; Li *et al.*, 1990, Michelini and McEvilly, 1991; Ben-Zion and Malin, 1991; Eberhart-Phillips and Michael, 1993; Thurber et

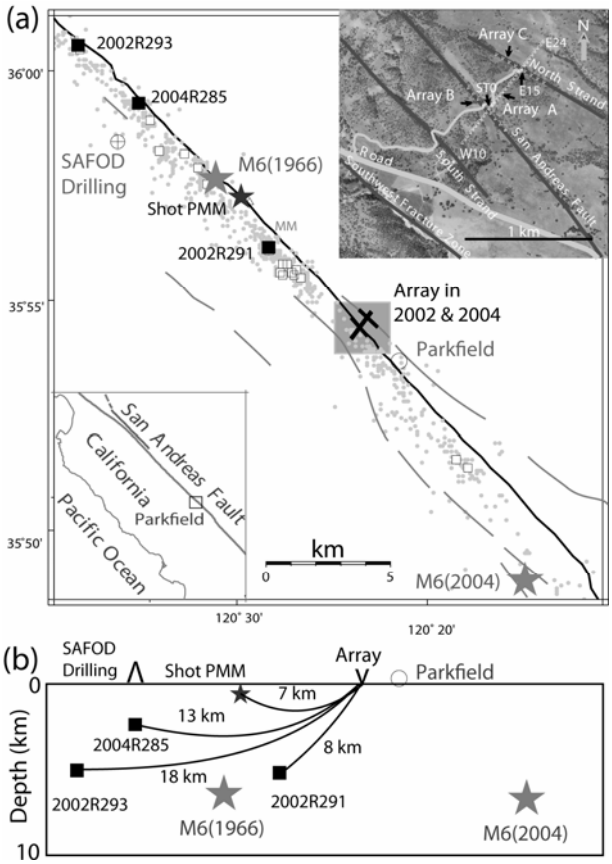

Fig. 1. (a) Map shows the location of seismic arrays (solid lines) deployed across and along the San Andreas fault and north strand at the site near Parkfield, California in 2002 and 2004, the *M*6 earthquake in 1966 and 2004 (grey stars), repeated shot PMM (black stars). Solid squares - microearthquakes on Julian date R291 and R293 in 2002 and the SAFOD target event on R285 in 2004. Dots - aftershocks of the *M*6 earthquake on September 28, 2004 at Parkfield, California. Open squares – clusters of repeated aftershocks used in our previous study for post-mainshock fault healing (Li et al, 2005). Inset: Array A consists of 35 PASSCAL RT130s and 2Hz L22 sensors with station spacing of 25 m. Coordinates of station ST0 of array A, located on the SAF main trace are 35°N54.566' and 116°W26.954'. Arrays B and C consist of 5 stations spaced at 50 m. Station ST0 was located on the main fault trace. Fault lines and topographic map are provided by Michael Rymer of the USGS. (b) The vertical section along the San Andreas fault at Parkfield shows locations of the seismic array, shots, the 1966 and 2004 *M*6 earthquakes, and repeated events in 2002 and 2004 used in this study.

al., 1997; Unsworth *et al.*, 1997). Using fault-zone trapped waves recorded at the SAF near Parkfield (Li *et al.*, 1997, 2004; Korneev *et al.*, 2003), a ~100-200 m wide low-velocity waveguide has been delineated on the SAF at seismogenic depths, in which shear-velocities are reduced by 20-40%. This distinct low-velocity zone is thought to be caused by intense fracturing during earthquakes, brecciation, liquid-saturation and possibly high pore-fluid pressure nears the fault. Recent results from San Andreas Fault Observatory (SAFOD) drilling and borehole logs show a low-velocity zone on the SAF with ~25-30% velocity reduction and high porosity a couple of hundred meters wide at the ~3.2 km depth, indicating a damage zone associated with the SAF (Hickman *et al.*, 2005). Byerlee (1990) and Rice (1992) note that pore fluids may migrate up from depth and the fault-zone acts as a channel due in part to its greater permeability than adjacent blocks. High pressure-water is coming up from depth and the highly fractured fault-zone acts as a fluid channel. High permeability and low strength have been measured in a damage zone centered at the main trace of the Nojima fault in the 1995 Kobe earthquake (Lockner *et al*., 2000).

The *M*6 Parkfield earthquake that occurred on 28 September 2004 provides us a rare opportunity to examine the possible variations in the volume and magnitude of the low-velocity anomalies on the SAF over the earthquake cycle. After this earthquake, we deployed a dense seismic array at the same sites as used in our experiment in the fall of 2002. The data recorded for repeated explosions detonated within the San Andreas in 2002 and after the 2004 *M*6 Parkfield earthquake show a few percent decreases in seismic wave velocity within an ~200-m-wide zone along the fault strike at the shallow depth, most likely due to the co-seismic damage of rocks during dynamic rupture in this *M*6 mainshock (Li *et al.*, 2006). The data from clustered aftershocks at the depth to 7 km show velocity recovery by ~1.2% within the fault zone in 3 months after the mainshock, indicating that the damaged rock has been healing following the mainshock. The width (~200 m) of the damage zone characterized by larger velocity changes is consistent with the low-velocity waveguide model on the San Andreas fault near Parkfield derived from fault-zone trapped waves (Li *et al.*, 1997, 2004; Korneev *et al.*, 2003).

In this paper, we present the data recorded in our repeated seismic surveys at Parkfield in the fall of 2002 and after the 2004 *M*6 earthquake. Results from waveform cross-correlation of the data for repeated microearthquakes before and after the 2004 mainshock further validate the progression of co-seismic damage and post-mainshock healing on the SAF at seismogenic depths associated with this earthquake.

2. Data and Results

In October 2002, we carried out a seismic experiment at the San Andreas fault near Parkfield and ~15 km southeast of the drilling site of San Andreas Fault Observatory at Depth (SAFOD) to record fault-zone guided waves generated by explosions and microearthquakes for a detailed delineation of the low-velocity damage structure on the SAF (Li *et al.*, 2004). The array recorded several local microearthquakes during 3 weeks of array operation, including two *M*~1-2 events occurring at depths of 5-6 km within the fault

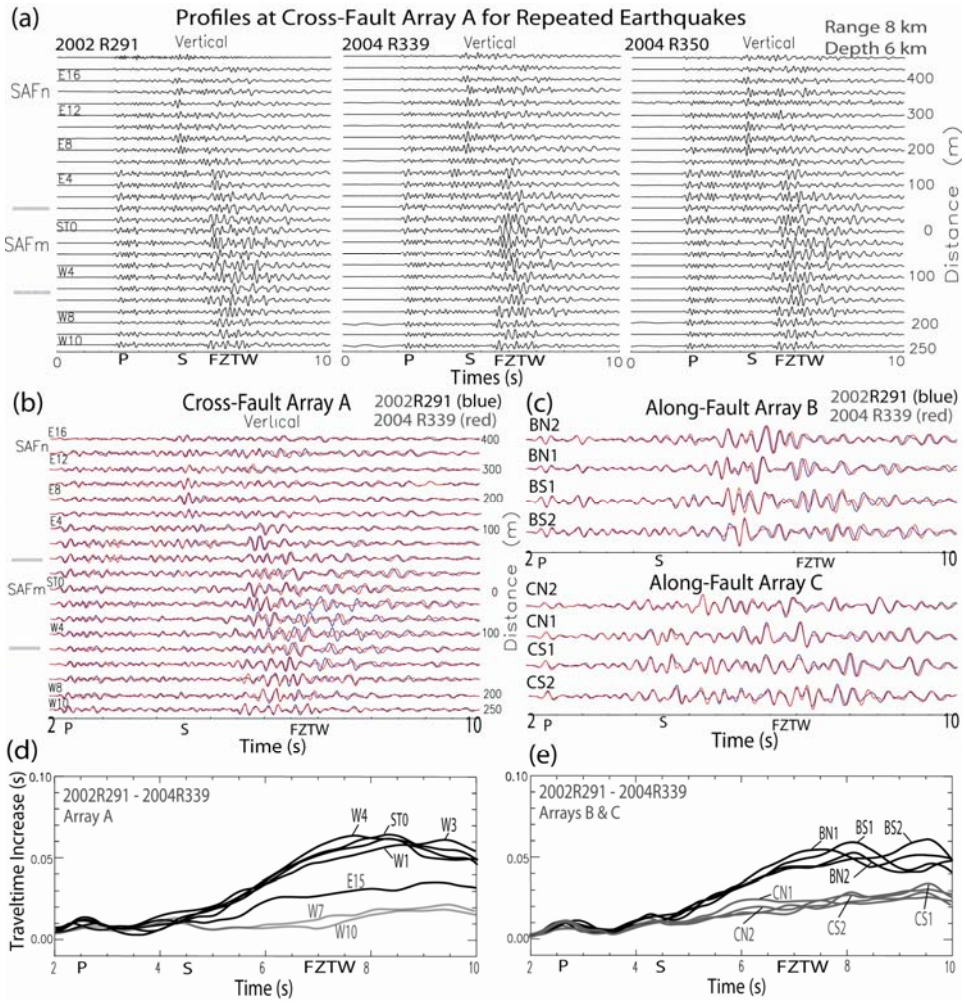

Fig. 2. (a) Vertical-component seismograms recorded at array A for 3 repeated *M*1.0 microearthquakes occurring at depth of 6 km and range 8 km from the array on Julian date R291 in 2002 and on R339 and R350 in 2004. Seismograms have been <8 Hz filtered. Stations ST0 and E15 were located on the main fault (SAFm) and north strand (SAFn). The first *P* and *S* waves arrive at ~2.2 s and ~4.5 s. Fault-zone trapped waves (FZTW) are dominant between 5.5 s and 8.5 s at stations in the range of ~150-200 m marked by two bars. (b) Overlapped seismograms at working stations of Array A for the event on R291 in 2002 (blue lines) and its repeated event on R339 in 2004 (red lines). Seismograms have been <5 Hz filtered. First *P*-arrivals from repeated events are aligned. Similar waveforms are recorded, but waves travel slower after the 2004 *M*6 Parkfield earthquake. (c) Seismograms recorded at arrays B and C along the SAF main fault and north strand for these two repeated events, showing larger arrival delays at stations of array B than array C for the event in 2004. Cross-correlations of seismograms for repeated events on R291 in 2002 and on R339 in 2004 (d) at stations of array A within and out of the fault zone, and (e) at stations of arrays B and C, showing larger traveltime increases at stations close to the SAF main fault.

zone on October 18 and 20 (Julian date R291 and R293) in 2002 (Fig. 1). These data are also used in the present study for monitoring temporal variations in velocity structure on the SAF associated with the 2004 *M*6 Parkfield earthquake. Immediately after the *M*6 Parkfield, California earthquake on 28 September, 2004, we deployed 45 PASSCAL seismometers in linear arrays at the same place as our previous experiment in 2002 near Parkfield to record aftershocks. The array site was located in the middle of a high-slip part of the surface rupture in this earthquake. Array A was 750-m-long across the main trace of the San Andreas fault (SAF) and its north strand while array B and array C were 200-m along the main fault and north strand, respectively (Fig. 1a). Three-component sensors were buried at the same locations as in our previous experiment at Parkfield in the fall of 2002. Seismometers operated in a continuous mode for 3.5 months starting a week after the mainshock, sampling at 100 Hz. We culled 21 clusters of repeated events from ~800 aftershocks in our recorded data using the catalog of Northern California Seismic Network (R. M. Nadeau,

personal communication, 2004). Each cluster includes at least 5 repeated aftershocks occurring at the same place with the location difference among them smaller than 200 m and the difference in magnitude smaller than 0.5. The location precision of Parkfield earthquakes in the catalog is less than a few tens of meters in relative distance. Repeated aftershocks in each cluster show similar waveforms with correlation coefficient higher than 0.8. The data from clustered aftershocks have been used to examine the fault healing after the 2004 *M*6 earthquake (Li *et al.*, 2006).

When we examined the data of 2004 Parkfield aftershocks, we found some clustered aftershocks occurring at the same locations of the microearthquakes recorded at our seismic array in 2002, which located beneath Middle Mountain and the SAFOD drilling site, respectively (Fig. 1b). We used the moving-window waveform cross-correlation method (Karageorgi *et al.*, 1992, 1997; Niu *et al.*, 2003) to measure the changes in seismic wave traveltimes for these repeated events recorded before and after the 2004 *M*6 Parkfield earthquake, and evaluate variations in velocity structure on the SAF associated with this *M*6 earthquake.

We applied low-pass (< 5Hz) filter to seismograms and used a 1-s window with the window center moving from the first *P*-arrival to later *S* cod for waveform cross-correlation. Korneev *et al.* (2003) used 2.5-5.5-Hz band-pass filtered seismograms from Parkfield microearthquakes at to compute spectral amplitude ratio of fault-zone guided waves to *S* waves. To ensure reliable results from computations, we enforced a minimum correlation coefficient of 0.8 for the *P*, *S* and guided waves in filtered seismograms between the repeated events. Figure 2a shows seismograms recorded at arrays across the SAF for the event on R291 in 2002 and its repeated events on R339 and R350 in 2004, occurring within the fault zone at depth of 6 km and ~5 km northwest of the array (Fig. 1). Prominent fault-zone trapped waves (FZTW) with relatively large amplitudes and long wavetrains following *S*-waves appeared at stations within a ~200-m-wide zone near the main fault trace. Figures 2b and 2c illustrate overlapped seismograms at 3 arrays across and along the fault for microearthquakes on R291 in 2002 and on R339 in 2004, showing similar waveforms for these two repeated events, but seismic waves traveled slower for the event after the 2004 M6 Parkfield earthquake. Note that stations on Array B along the main fault trace registered larger traveltime changes than those on Array C along the north fault strand. Figures 2d and 2e illustrates moving-window cross-correlations of waveforms recorded at Arrays A, B, and C for these

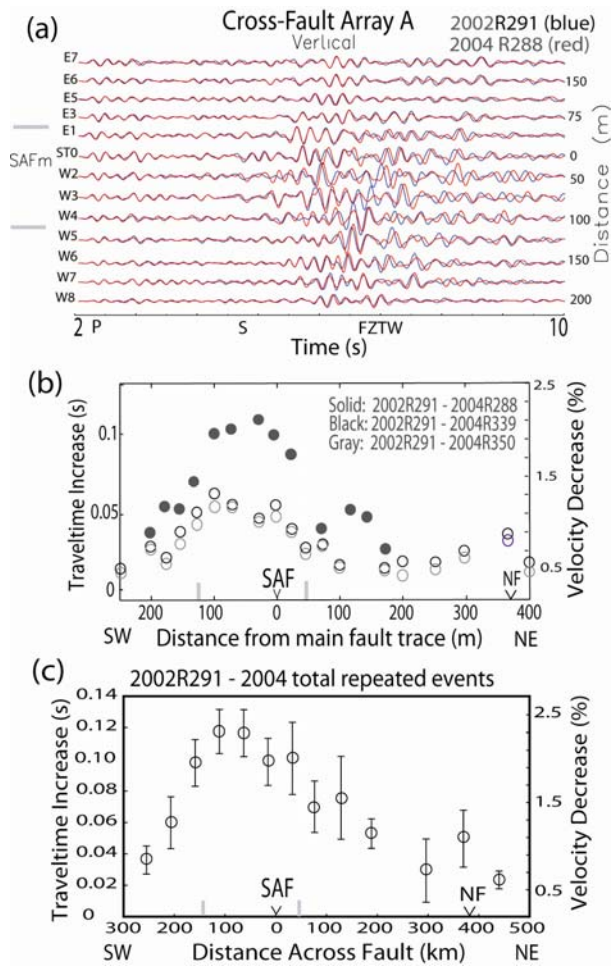

Fig. 3. (a) Overlapped seismograms at working stations of Array A for the event on R291 in 2002 and its repeated event on R288 in 2004. Seismograms have been <5 Hz filtered. Other notations are the same in Fig. 2b. (b) The maximum traveltime increases of seismic waves in 2-10 s at stations versus distances from the main fault trace measured by waveform cross-correlations between the event on R291 in 2002 and its repeated events on R288, R339 and R350 in 2004. (c) Traveltime increases and velocity decreases in percentage and standard deviations for shear wave and fault-zone trapped waves at all available stations measured by moving window cross-correlations between the event on R291 in 2002 and 6 repeated events on R288 to R350 in 2004.

two repeated events, showing ~35-65 ms delay in traveltime of dominant fault-zone trapped waves between 5.5 s and 8.5 s at stations within the fault zone, but less than 20 ms delay in traveltime for the *S* wave arriving at ~4.5 s and later coda at stations in surrounding rocks in 2004. Stations on the north fault strand registered traveltime delay of ~25-35 ms in traveltime between 5.5 and 8.5 s. In computation, we aligned the first *P*-arrivals for repeated events to avoid errors in event origin times in the catalog so the true traveltime delays for *S* and trapped waves may contain small undetermined changes in *P* traveltime. Assuming that velocity changes were uniform in the crust sampled

by these waves, the increases in traveltime are straightforward to interpret. The dominant trapped waves arrived between 5.5 s and 8.5 s with a 35-65 ms delay in 2004, so the shear wave velocity within the fault zone decreased by ~0.7% in average plus unmeasured changes for the *P* wave between R291 in 2002 and R339 in 2004. In contrast, the shear wave velocity in surrounding rocks decreased by <0.25% during the same time period, according to a ~10-20 ms traveltime delay for *S* and coda waves arriving between 4.5 s and 8.5 s. In justice to this simplification for estimation of velocity variations from measured traveltime changes, we show the synthetic traveltime delays between the repeated events using the depth-variable velocity model in the discussion section.

Figure 3a shows overlapped seismograms at stations of array A for the event on R291 in 2002 and its earlier repeated event on R288 in 2004, which occurred 2 weeks after the *M*6 Parkfield earthquake, illuminating larger traveltime delays between them than those for the later repeated events. In Figure 3b, we plot maximum increases in traveltime (2-10 s) at all working stations of 3 arrays measured by moving window cross-correlation between the event on R291 in 2002 and its repeated events on R288, R339, and R350 in 2004, showing largest traveltime delays in 2004 at stations within a ~200-m-wide zone along the main fault and much smaller changes at stations beyond this zone while intermediate changes registered at stations on the north fault strand for each pair of repeated events. The measurements show a ~110 ms maximum delay in traveltime of trapped waves arriving at ~8 s within the fault zone between the events on R291 in 2002 and on R288 in 2004. This value is about twice larger than those measured for later repeated aftershocks on R339 and R350 in 2004. We estimate that the shear wave velocity decreased by ~1.4% plus changes for *P* waves within the fault zone between R291 in 2002 and R288 in 2004. If *P* and *S* wave velocity changes have the proportion as they would in a Poisson solid, measured traveltime increases imply that the net decrease in shear wave velocity between R291 in 2002 and R288 in 2004 was ~2.3% within the fault zone, and then recovered to a deficit of ~1.2% on R339 and R350 in 2004. Figure 3c exhibits the maximum traveltime and velocity changes measured by moving-window waveform cross-correlations at all available array stations between the event on R291 in 2002 and its 7 repeated events occurring on R288 to R350 in 2004. The data have been corrected for changes in traveltimes of *P* waves and normalized to the earliest event on R288 among them. Again, results show velocity decreases after the *M*6 Parkfield earthquake on 28 September (R273) in 2004, with the largest change of ~2.3% within a ~200-m wide zone along the SAF main trace and moderate changes at the north fault strand.

Assuming that there was no significant change in seismic velocity between the fall of 2002 and September 28, 2004 at Parkfield region, the velocity changes measured in our repeated seismic surveys are most likely associated with the September 28, 2004 *M*6 Parkfield earthquake that caused velocity decrease due to co-seismic damage of fault-zone rocks with cracks opening in dynamic rupture. The damaged rock then recovered its rigidity with time after the mainshock due to closure of cracks. Although processes associated with aseismic transients have shown to influence wave propagation at Parkfield (Niu *et al.*, 2003), there were no such transients and resolvable measurements in seismic velocity in this area between the fall of 2002 and the 2004 *M*6 earthquake (Rubinstein and Beroza, 2005). A seasonal water table change and rainfall would affect the seismic velocity at shallow depth (Karageorgi *et al.*, 1997). However, as we carried out repeated experiments at Parkfield in the same season of 2002 and 2004, there were not significant variations in water table. The driller showed that the water table in the shot-hole at Middle Mountain was at the depth of ~25 m in the fall of 2002 and 2004. Thus, it is plausible to attribute our observed velocity changes at Parkfield to the 2004 *M*6 earthquake. We found that the damage zone is not symmetric but extends farther on the southwest side of the main fault trace. In our previous study of fault-zone structure at Parkfield (Li *et al.*, 2004), we have delineated a ~150-m-wide, distinct low-velocity waveguide on the main SAF and a branch waveguide with smaller velocity reduction on the north strand at this site. The width of this zone characterized by largest velocity decreases caused by the recent *M*6 earthquake is consistent with the width of the low-velocity zone on the SAF delineated using fault-zone trapped waves. Observations of seismic velocity changes before and after the 2004 *M*6 Parkfield earthquake indicate that the low-velocity waveguide on the SAF has been at least partially softened, with additional cumulative damage due to recurrent ruptures. We interpret that the north strand might have experienced minor breaks due to secondary slip and strong shaking from ruptures on the main fault in the major earthquakes on the SAF, including the 2004 *M*6 mainshock.

The above examples show larger delay in traveltime between the event in 2002 and the earlier repeated event in 2004, indicating that seismic velocities within the fault zone might recover with time after the 2004 *M*6 earthquake. In order to confirm this trend, we examined traveltime delays between the event on R291 in 2002 and its ten repeated events occurring on R281-R360, from a week to ~3 months after the 2004 *M*6 mainshock. Figure 4a exhibits seismograms of these repeated aftershocks at stations W1 and E7 located within and out of the fault zone, respectively. *P*-arrivals for all events are aligned at the same time in plot. Fault-zone trapped waves are dominant between 6.5 s and 8.5 s at station W1, but show much smaller amplitudes at station E7, 175 m northeast of the main

fault trace. We observed similar waveforms for the repeated events. However, seismic waves traveled faster in 2002. Moving-window cross-correlations of waveforms show the largest delay of ~125 ms of dominant fault-zone trapped waves arriving at ~8 s at station W1 between the earliest aftershock on R281 in 2004 and the event on R291 in 2002, plus the undetermined changes of the *P*-wave (Fig. 4b). The traveltime delays gradually decreased to ~50 ms for the latest repeated event on R350, ~3 months after the 2004 mainshock. Based on the same assumptions described above, we estimate that the net shear velocity within the fault zone decreased by ~2.5% between R291 in 2002 and R281 in 2004, and then increased by ~1.2% in the following ~3 months. In contrast, the changes in shear velocity registered at station E7 was smaller than 0.5% in the same time period. Although we lack of data in the first week after the 2004 Parkfield earthquake, the data recorded at our arrays indicate that shear velocities within the fault zone reduced by at least 2.5%, most likely due to the damage of fault-zone rocks in dynamic rupture of this *M*6 earthquake. Figure 4b illustrates traveltime decreases and shear velocity increases measured at stations within and out of the fault zone for these repeated aftershocks in 2004 with respect to the event on R291 in 2002. The seismic velocity increases with time after the mainshock indicate that the damaged rock has being healing due to its rigidity recovery after the earthquake. However, the healing rate was not constant, but decreased logarithmically with time, similar to our previous observations at rupture zones of the 1992 Landers and 1999 Hector Mine earthquakes (Li *et al.*, 2003; Vidale and Li, 2003).

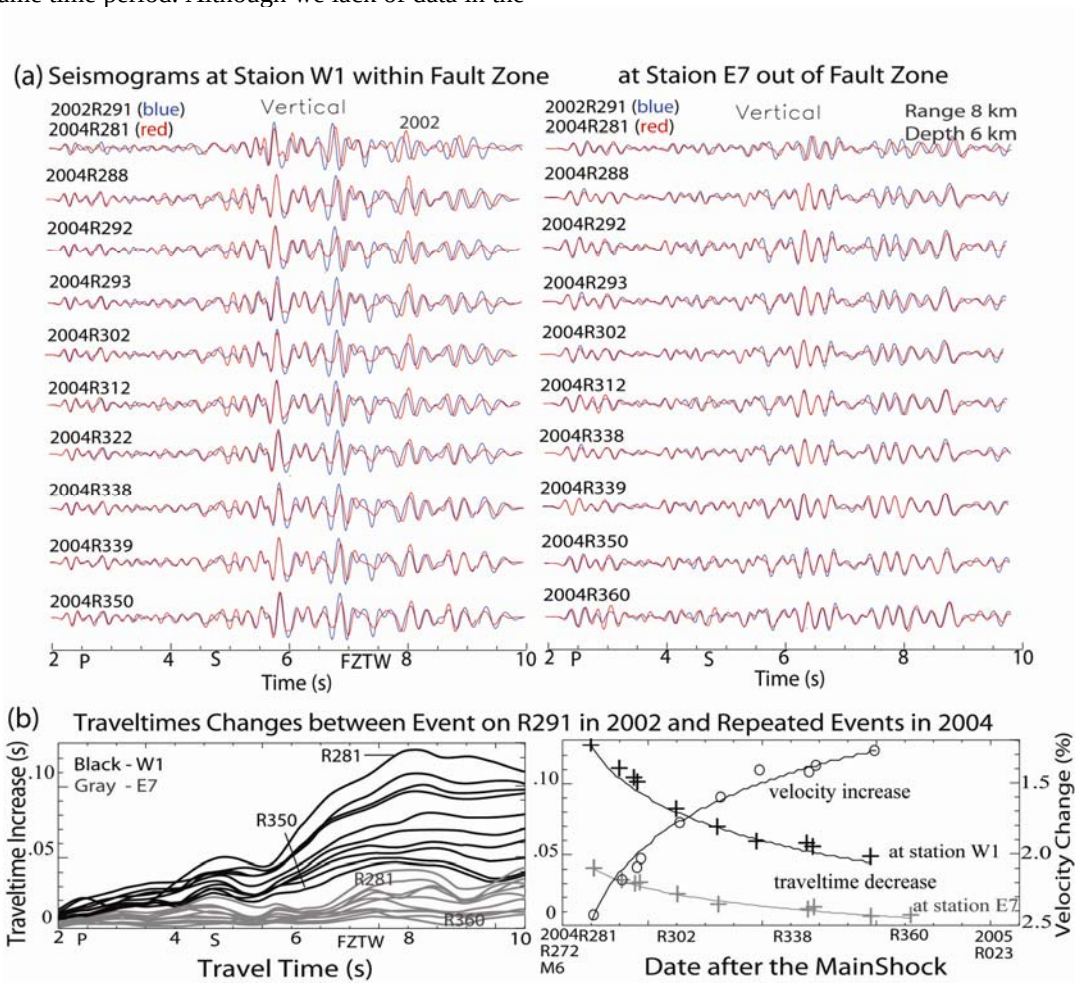

Fig. 4. (a) Vertical-component seismograms recorded at stations W1 and E7 of array A for the microearthquake on R291 in 2002 (black line) and 10 repeated events from R281 to R360 in 2004 (gray lines), showing larger traveltime increases at station W1 within the fault zone than at station E7, 175 m off the fault. Seismograms have been low-pass (<5 Hz) filtered. First *P*-arrivals from repeated events are aligned at ~2.2 s. (b) Left: Moving window cross-correlations of waveforms show traveltime increases between the event on R291 in 2002 and its 10 repeated events in 2004 with the largest increase for the earliest repeated event on R281 and a decreasing trend with dates after the mainshock. Traveltime increases are much larger at station W1 than station E7 in the same time period. Right: The maximum traveltime delays and shear velocity changes in percentage measured at stations W1 and E7 between the event on R291 in 2002 and its repeated events in 2004. The curve is the logarithmic fit to measurements of traveltime changes with a constant of velocity change 0.012 /day in logarithm.

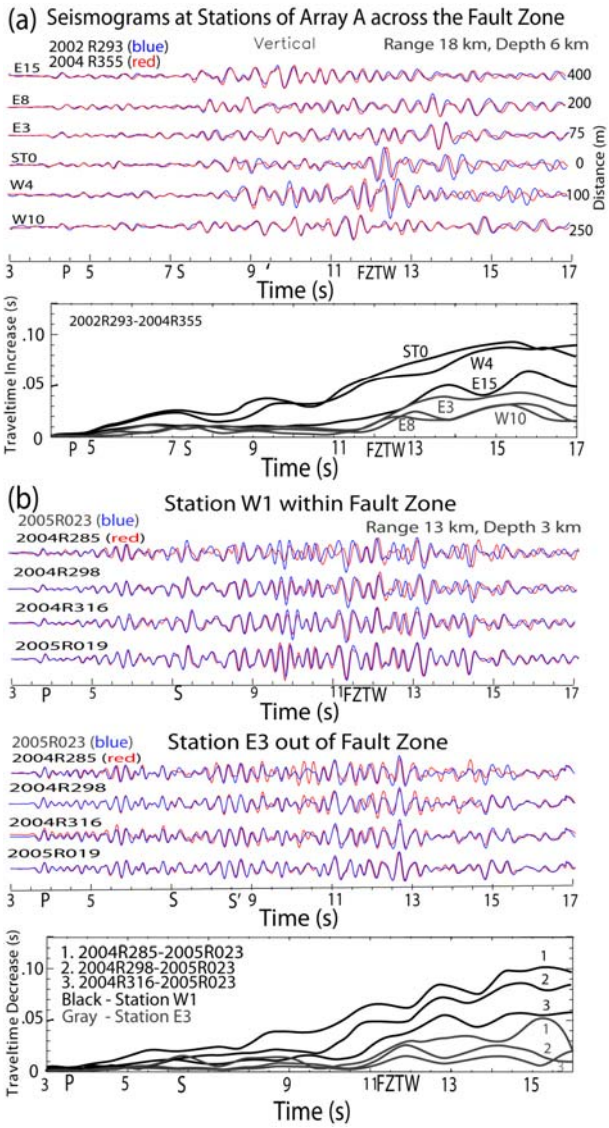

Fig. 5. (a) Vertical-component seismograms recorded at 6 stations of array A for a *M*1.4 earthquake occurring at depth of 5 km and distance (range) 18 km NW of the array on Julian date R293 in 2002 and a repeated event on R355 in 2004. Seismograms have been low-pass (<5 Hz) filtered and are plotted using a common scale for all traces. First *P*-arrivals from repeated events are aligned at ~4.2 s. Moving-window cross-correlations of waveforms for the repeated events show largest traveltime increases at stations ST0 and W1 within the fault zone. Station W15 located at the north fault strand registered moderate traveltime increase. (b) Vertical-component seismograms at stations W1 and E3 within and out of the fault zone for 5 repeated aftershocks occurring on the SAF at the location of SAFOD target events at depth ~3 km. First *P*-arrivals from these events are aligned at ~3.6 s. Seismograms for the latest event on R023 in 2005 (blue line) are overlaid by those from 4 repeated aftershocks in 2004 (red lines), showing that seismic waves traveled fastest for the latest event. Waveform cross-correlations between the event on R023 in 2005 and its earlier repeated events show that travel times from these events decrease with time after the *M*6 mainshock.

We then examined the data recorded for another microearthquake recorded on October 20 (R293) in 2002 and its repeated events in 2004, occurring at 5 km depth and near the north end of the rupture segment of the 2004 *M*6 earthquake, ~16 km NW of the array site (Fig. 1). Figure 5a exhibits seismograms recorded at stations of array A for this event and its repeated event on December 20 (R355) in 2004, showing similar waveforms, but waves traveled faster in 2002. Note the larger amplitudes of fault-zone trapped waves appearing at stations within the fault zone. Waveform cross-correlations show ~80-90 ms increase in traveltime of dominant trapped waves arriving between 12 s and 15 s at stations ST0 and W4 within the fault zone, but <30 ms at stations E8 and W10 far away from the main fault trace in 2004. Station E15 on the north fault registered a moderate delay of ~50 ms in traveltime. Taking similar assumptions as in the previous examples (Fig. 2), we estimate that net shear wave velocities within the fault zone reduced by ~0.9% for this pair of repeated events located near the NW end of the 2004 rupture zone, smaller than the velocity reduction of ~1.2% measured for repeated events between R291 in 2002 and R350 in 2004 (see Fig. 3), which located in the middle of a high-slip part of the rupture zone although the time spans between repeated events in the two pairs are nearly the same. These measurements indicate the variation in magnitude of rock damage along the rupture in the 2004 Parkfield earthquake.

In our experiment at Parkfield, we recorded several small persistently repeated aftershocks on the main SAF at the location of the SAFOD "target events" (Fig. 1). Figure 5b shows seismograms recorded at stations W1 and E3 of array A for five such repeated events between R285 in 2004 and R023 in 2005. Seismograms from the latest event on 23 January (R023) in 2005 are overlaid by those from 4 earlier repeated events on R285, R298 and R316 in 2004 and R019 in 2005. We observed similar waveforms for the repeated events, but waves from the latest event traveled fastest and waves from the earliest event traveled slowest, showing velocity increase with time after the *M*6 mainshock on September 28 (R273) in 2004. We measured traveltime changes between the event on January 23 (R023) in 2005 and earlier repeated events by waveform cross-correlations, showing the maximum traveltime advance of ~80 ms for dominant guided waves arriving at ~13 s at station W1 within the fault zone plus the change for *P*-wave between R023 in 2005 and R285 in 2004. In contrast, smaller changes were registered at station E3 out of the fault zone. The measurements show that seismic wave traveltimes decreased (velocity increased) with time in the post-mainshock stage, most likely due to healing of fault-zone rocks that damaged in the *M*6 mainshock. Based on the measurements for this cluster of repeated events occurring near the NW end of the rupture in 2004, we estimate that the apparent shear

velocity within fault zone increased by ~1.0% in ~3 months between R285 in 2004 and R023 in 2005, smaller than the value measured for another cluster of repeated events in the middle of a high-slip part of the surface rupture during the similar time period as shown in Figure 4.

3. Discussions and Conclusion

We have used the data from repeated explosions detonated within the SAF near Parkfield before and after the 2004 *M*6 earthquake to measure the seismic velocity changes associated with this earthquake. Figure 6a exhibits seismograms with similar waveforms recorded at cross-fault array A for the repeated shots detonated on 16 October in 2002 and 30 December in 2004. However, seismic waves traveled slower after the 2004 M6 earthquake with largest traveltime increases in a ~200-m-wide zone along the main fault, moderate increases at the north strand and much smaller changes in surrounding rocks (Fig. 6b). Moving-window cross-correlations of waveforms for the repeated shots show a decrease of ~1.3% in shear velocity within the fault zone. We also measured traveltime changes for repeated aftershocks in 21 clusters located at different depths along the rupture of the 2004 earthquake and found that the maximum shear velocity increased by ~1.2% within the fault zone beneath Middle Mountain during ~3 months starting one week after the mainshock (Li *et al.*, 2006). Assuming that there were no significant changes in seismic velocity at Parkfield area in the time period between the shot in 2002 and the 2004 *M*6 earthquake, we estimate the net decrease in shear velocity of at least ~2.5% owing to co-seismic damage of fault-zone rocks caused by dynamic rupture of this *M*6 earthquake although we lack of data in the first week after the mainshock. We note that the ratio of traveltime changes for *P* to *S* waves is 0.57 within the rupture zone and ~0.65 in the surrounding rocks (Fig. 6c), indicating that cracks within the fault zone are more wet than those out of the zone according to equations for the elastic moduli of the medium with cracks (Garbin and Knopoff, 1975). Water may be coming up from depth with the highly fractured fault-zone acting as a fluid channel.

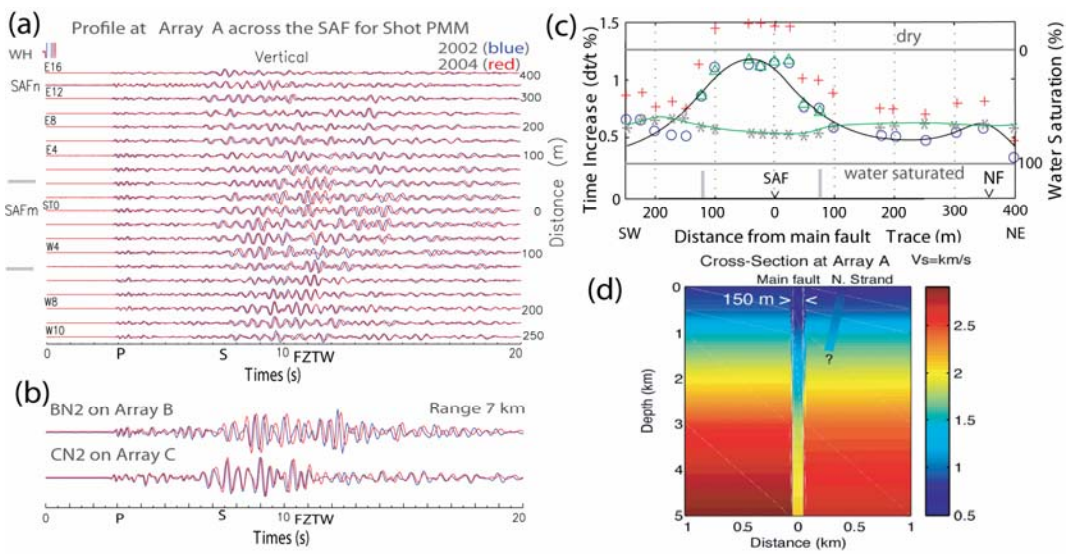

Fig. 6. (a) Vertical-component seismograms recorded at array A across the SAF for repeated shot PMM detonated within the low-velocity fault zone at 7 km NW of the array on 16 October (R289) in 2002 and 28 December (R364) in 2004. Seismograms have been low-pass (< 3 Hz) filtered and are plotted using a common scale for all traces in each plot. The shot origin time is at 0 s. *P* and *S* waves arrive at ~3 s and ~7 s. Fault-zone trapped waves (FZTW) with large amplitudes and long wavetrains are dominant between *S* arrival and 15 s at stations in the range of ~150 m marked by two bars. Similar waveforms were recorded for the repeated shots, but waves traveled slower after the *M*6 Parkfield earthquake in 2004. WH denotes the station located at the wellhead of shot-hole; the unclipped first *P* arrivals show identical arrival times for the repeated shots. (b) Vertical-component seismograms recorded at station BN2 of array B and CN2 of array C. for repeated shot PMM in 2002 and 2004, showing similar waveforms, but with larger delay at array B along the main fault than at array C along the north fault (NF) strand. (c) Traveltime increases in percentage for *P* (red crosses), *S* (blue circles), and trapped waves (green circles) measured by cross-correlations of seismograms at array A across the SAF for repeated shot PMM in 2002 and 2004, showing seismic velocity decreases. The solid curve is a polynomial fit to traveltime increases of *S* waves in 2004. A pair of vertical grey bars denotes a 150-200-m-wide zone with greater travel time increases. Ratio of traveltime changes for *P* waves to *S* waves (green stars with a curve) indicates the degree of water saturation in cracks. Two horizontal light lines indicate the ratios predicted for a range of water percentage for Poisson solid. (d) The low-velocity waveguide model on the SAF, near Parkfield derived from fault-zone trapped waves (Li *et al.*, 2004). The main fault zone is marked by a ~150-m-wide waveguide in which velocities are reduced by 30-40% and *Q* is 10-50 between the surface and 5 km depth. The north strand is marked by a minor waveguide.

Figure 6d shows a ~150-m-wide low-velocity zone on the SAF at this site, within which seismic velocities are reduced by 25-40% from wall-rock velocities to the depth of at least 5 km, delineated in our previous seismic study using fault-zone guided waves at Parkfield (Li *et al.*, 2004). Recent results from the SAFOD drilling project and borehole logs at Parkfield show high porosity and multiple slip planes in an ~200-m-wide low-velocity zone with velocity reduction of ~25-30% on the SAF at ~3.2 km depth (Hickman *et al.*, 2005). Our present study using repeated events shows that the SAF at Parkfield co-seismically weakens and consequently heals when it undergoes strong dynamic stresses and pervasive cracking during the 2004 *M*6 earthquake. Although the damage zone along the SAF has accumulated over geological time, it was in part weakened by the latest *M*6 earthquake in 2004 due to inelastic deformation around the propagating crack tip in the mainshock, as predicted by existing fault-zone rupture models (e.g., Scholz, 1990).

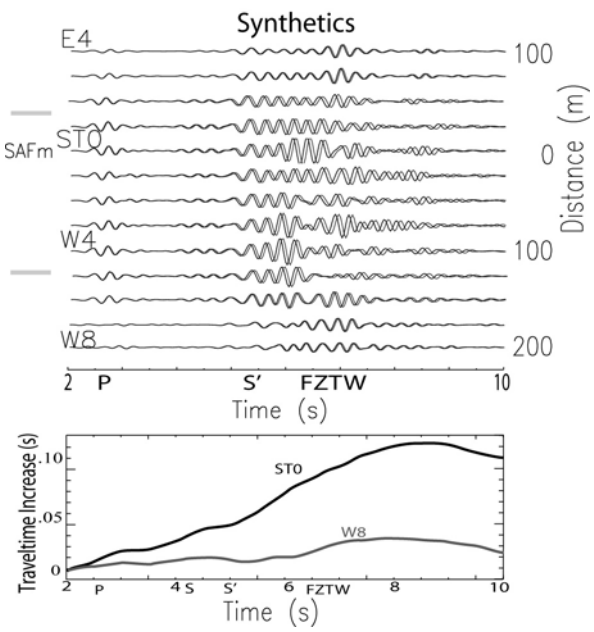

Fig. 7. top: Vertical-component of finite-difference synthetic seismograms at stations of array A for the two repeated events on R291 in 2002 (black lines) and on R281 in 2004 (gray lines) using the fault-zone model shown in Figure 6d. Model parameters used for the event in 2002 are the same as those in the model resulted from our previous experiment at this site in 2002 (Li *et al.*, 2004). Velocities are reduced by 2.5% and 0.5% within and out of the fault-zone, respectively, for computation of seismograms for the event in 2004. Seismograms have been <5 Hz filtered. First *P*-arrivals from repeated events are aligned. bottom: Moving-window cross-correlations of seismograms for the repeated events at stations ST0 and W8 of array A within and out of the fault zone. Other notations are the same as in Fig. 2.

In the present paper, we show the data from microearthquakes recorded at our array in October 2002 and their repeated events recorded at the same array site after the 2004 *M*6 Parkfield earthquake to determine the seismic velocity changes on the SAF at seismogenic depth before and after this earthquake using the moving-window waveform cross-correlation for these repeated events. The measurements of traveltime changes (Figures 2 and 3) indicate a ~2.5% shear velocity decrease within the fault zone between R291 in 2002 and R281 in 2004, a week after the *M*6 Parkfield earthquake. This value is consistent with our previous estimation of the net velocity decrease on the SAF caused by this *M*6 earthquake using the data from repeated shots and clustered aftershocks as described above. We interpret that the 2004 *M*6 mainshock caused additional damage of rocks while the low velocity damage structure on the SAF has cumulated effects in recurrent rupture of historical earthquakes.

We simulated seismograms for the event on R291 in 2002 using a 3-D finite-difference code [*Graves*, 1996] in terms of the depth-variable structure model shown in Figure 6d and for its repeated event on R281 in 2004 with the velocities reduced by 2.5% within the fault zone and by 0.5% in wall-rocks from original values in this model. Figure 7 shows synthetic seismograms at cross-fault array and traveltime delays measured by moving-window cross-correlation of waveforms at stations STO and W8 within and out of the fault zone. The synthetic traveltime delays between these repeated events are in general agreeable with observations (Fig. 4b).

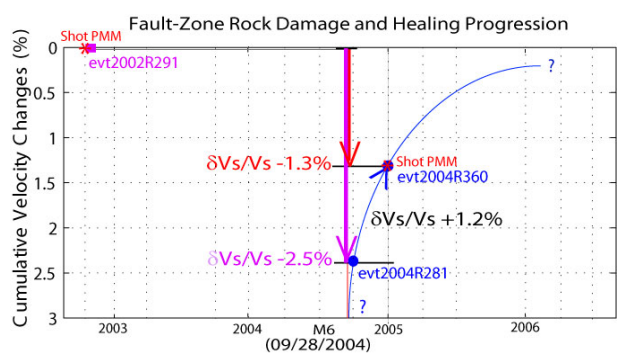

Fig. 8. S-wave velocity changes within the rupture zone associated with the *M*6 Parkfield earth-quake on September 28, 2004. The *S* velocity decreased by ~1.3% in the time period between the two repeated shots on 16 October, 2002 and 28 December, 2004. Measurement for repeated microearthquakes occurring in 2002 and in a week after the 2004 *M*6 mainshock show ~2.5% decrease in *S* velocity, most likely due to the co-seismic rock damage during the mainshock. Measurements for repeated aftershocks show that the *S* velocity within the rupture zone increased by ~1.2% in the following 3 months starting, indicating fault healing with rigidity recovery of damaged rocks.

The low-velocity anomalies on the SAF might vary over the earthquake cycle. Our measurements of the changes in traveltime for repeated aftershocks show a ~1.2% increase in shear velocity within the rupture zone during ~3 months starting a week after the 2004 *M*6 Parkfield earthquake (Fig. 4). It indicates that the fault heals by rigidity recovery of damaged rocks in the post-seismic stage due to the closure of cracks that opened in the mainshock. The healing rate is logarithmically decreasing through time with greater healing rate in the earlier stage of the inter-seismic period (Fig. 8).

We find that the magnitude of rock damage and healing varies across the SAF with largest value within a ~150-200-m wide low-velocity zone (Figs 3 and 6) that experienced greater damage in the 2004 *M*6 earthquake. The damage zone is asymmetric, broader on the southwest side of the main fault trace. The asymmetry may imply that the fault zone has a significant cumulative damage due to previous large earthquakes on the SAF. When a fault ruptures, it may preferentially damage the already weakened rocks in the zone, even though those rocks are not symmetrically distributed on either side of the main slip plane (Chester *et al.*, 1993). Alternately, greater damage may be inflicted in the extensional quadrant than the compressional quadrant near the propagating crack tip (Andrews, 2005). We shall use fault-zone guided waves and coda wave interferometry method (Snieder and Vrijlandt, 2005) to study if the width of the damage zone also changed due to this M6 earthquake.

The measurements of seismic velocity changes for repeated events occurring at different locations show variations in rock damage and healing along the fault strike, with larger magnitude in the high-slip part of the SAF beneath Middle Mountain during the 2004 *M*6 Parkfield earthquake (Figs. 3 and 4) than near the NW end of the rupture zone (Fig. 5). Korneev *et al.* (2003) found larger amplitudes of fault-zone guided waves on the SAF southwest of Middle Mountain, possibly due to dewatering by fracture closure and fault-normal compression. Our observations are consistent with the results from 21 clusters of aftershocks along the 2004 rupture at Parkfield (Li *et al.*, 2006) and our previous tentative conclusion for observations of fault healing at the Landers and Hector Mine rupture zones that greater damage was inflicted, and thus greater healing is observed, in regions with larger slip in the mainshock (Li *et al.*, 2003).

Calculation of a ~2.5% decrease in velocity using formula for cracked media (O'Connell and Budiansky) revealed that the apparent crack density within the rupture zone increased by ~0.035, which caused ~5% decrease in shear rigidity of the fault-zone rock during dynamic rupture of the 2004 *M*6 Parkfield earthquake. The subsequent 1.2% increase in *S* velocity suggests the apparent crack density within the rupture zone decreased by 0.017 in the following ~3 months.

Rubinstein and Beroza (2005) observed significant traveltime delays caused by the 2004 *M*6 Parkfield earthquake at the seismic network stations for repeated earthquakes occurring at depths of ~3 km near the SAFOD drilling site before and after the 2004 *M*6 earthquake. They measured traveltime increases exceeding ~25 ms in *S* coda for the repeated SAFOD target events occurring on October 21 and 23, 2003, approximately one year before the *M*6 earthquake and on September 28, 2004 immediately after the mainshock at borehole station MM of Parkfield Seismic Network, located ~200 m NE of the SAF main trace (Fig. 1a). They also observed direct *S*-wave arrival delays up to 7 ms to many of the surface stations but much smaller delays at borehole stations in the Parkfield area. They attribute the time delays to cracks opened during the strong shaking of the *M*6 Parkfield earthquake at depths shallower than 100-300 m. Crack opening is likely favored at shallow depths with soft rock and lower confining crustal stress in a broad distance range from the epicenter due to strong ground motion. Our stations, in contrast, were located much closer to the fault than the network stations. The data presented here from the shots and aftershocks located on or close to the fault mainly document the changes within the fault zone rather than the changes in surrounding rocks. The smaller (<0.3%) background changes in traveltime registered at off-fault stations of our seismic seem consistent with observations of Rubinstein and Beroza (2005). We interpret the observed velocity decrease within the fault zone as mainly due to crack opening caused by the dynamic rupture of the latest *M*6 earthquake. Shaking-induced weakening may also effect the rupture propagation because the pre-existing weak, low impedance fault zone is susceptible to damage (Fialko *et al.*, 2002; Vidale and Li, 2003).

During the fault healing, the reduction of crack density may be controlled by a combination of mechanical and chemical processes on the active fault. Fault healing may be affected by time-dependent frictional strengthening (Vidale *et al.*, 1994; Marone, 1998), rheological fluid variations or changes in the state of stress (Blanpied *et al.*, 1992), cementation, recrystallization, pressure solution, crack sealing and grain contact welding (Hickman and Evans, 1992; Olsen *et al.*, 1998) and the fault-normal compaction of the rupture zone (Massonnet *et al.*, 1996; Boettcher and Marone, 2004) as well as chemical healing from mineralogical lithification of gouge materials over longer time period at seismogenic depth (Angevine *et al.*, 1982). In addition, the 'crack dilatancy' mechanism (Nur, 1972) associated with the earthquake is likely to operate for co-seismic fault damage and post-mainshock healing even if other processes are active too. The temporal changes in crack-induced anisotropy near the Nojima fault that ruptured in the 1995 *M*7.1 Kobe earthquake have been observed in shear-wave splitting

(Tadokoro *et al.*, 1999; Ikuta and Yamaota, 2004). However, there was no clear change in magnitude of shear-wave splitting after the 1999 Hector Mine earthquake (Cochran *et al.*, 2003), suggesting that the shear-wave splitting may be not sensitive to detect small changes in crack density because the velocity change influences both the fast and slow orthogonally-polarized shear waves.

The stress-related temporal changes in seismic velocity caused by the 1989 Loma Prieta, California earthquake have been reported (Ellsworth *et al.*, 1992; Dodge and Beroza, 1997; Schaff and Beroza, 2004). Baisch and Bokelmann (2002) suggest that coseismic deformation caused by this earthquake might lead to crack opening either by localizations of shear stress or by elevated pore fluid pressure. Concentrated deformation at low-strength fault zones may help to cause damage. After the earthquake, relaxation processes, such as crack healing, fluid diffusion, and post-seismic deformation cause the cracks to close again with an approximately logarithmic recovery rate (Dieterich, 1972). As rocks heal, a contribution can be from either continued right-lateral deformation due to the regional stress field that dominated the coseismic displacements or fault-normal compression owing to a reduction in crack volume. The variation in apparent crack density inferred by seismic velocity measurements reflects changes in either crack volume or rearrangement of aspect ratio caused by the earthquake. We tentatively conclude that the cracks that opened during the mainshock closed soon thereafter. This consistent with our interpretation of the soft low-velocity fault-zone waveguide on the SAF as being at least partially weakened in the 2004 *M*6 mainshock, but with possible significant cumulative effects as well.

Our observations of fault zone damage and healing associated with the latest *M*6 Parkfield earthquake are in general consistent with the model of velocity evolution owing to damage and healing for Lander and Hector Mine earthquakes (Vidale and Li, 2003). However, the magnitude of damage and healing observed near Parkfield on the SAF is smaller than those on the Landers and Hector Mine rupture zones, probably related to the smaller magnitude mainshock, and smaller slip, and possibly differences in stress drop, pore-pressure, and rock type.

Acknowledgments. This study was supported by NSF/EarthScope Grant EAR-0342277, USGS Grant NEHRP20060160, and partially by the Southern California Earthquake Center. Special thanks to S. Hickman, W. Ellsworth, and M. Zoback of SAFOD PIs for their coordination in our experiments for seismic characterization of the SAFOD drilling. We acknowledge J. Varian, G. Varian, G. Work, and B. Mosby for permissions to conduct our experiment on their lands, and the IRIS for the use of PASSCAL instruments. We are grateful to P. Malin, C. Thurber, S. Roecker, M. Rymer, R. Catchings, A. Snyder, R. Russell, L. Powell, B. Nadeau, N. Boness, D. McPhee, and F. Niu for their collaborations in our research at Parkfield. We thank Editor Eiichi Fukuyama, reviewer T. Mizuno, and an anonymous reviewer for their helpful suggestions and comments on the manuscript. SCEC is funded by NSF Cooperative Agreement EAR-0106924 and USGS Cooperative Agreement 02HQAG0008. The SCEC contribution number for this paper is 962.

References

Aki, K., Asperities, barriers, characteristic earthquakes, and strong motion prediction, *J. Geophys. Res*. **89**, 5867-5872, 1984.

Andrews, D. J., Rupture dynamics with energy loss outside the slip zone, *J. Geophys. Res*. 110, B01307, dio:0.1029. 2005.

Angevine, C. L., D. L., Turcotte, and M. D. Furnish, Pressure solution lithification as a mechanism for the stick-slip behavior of faults, *Tectonics*, **1**, 151-160, 1982.

Baisch. S, and G. H. R. Bokelmann, Seismic waveform attributes before and after the Loma Prieta earthquake: scattering change near the earthquake and temporal recovery, *J. Geophys. Res*. **106**, 16,323-16,337, 2001.

Ben-Zion, Y., and P. Malin, San Andreas fault zone head waves near Parkfield, California, *Science*, **251**, 1592-1594, 1991.

Blanpied, M. L., D. A. Lockner, and J. D. Byerlee, An earthquake mechanism based on rapid sealing of faults, *Nature*, **359**, 574-576, 1992.

Boettcher, M, S., and C. Marone, Effects of normal stress variation on the strength and stability of creeping faults, *J. Geophys. Res.* **109**, B03406, doi:10.1029/2003JB002824, 2004.

Byerlee, J., Friction, overpressure and fault-normal compression, *Geophys. Res. Lett*. **17**, 2109-2112, 1990.

Chester F. M., J. P. Evans, and R. L. Biegel, Internal structure and weakening mechanisms of the San Andreas fault, *J. Geophys. Res*. **98**, 771-786, 1993.

Cochran, S. E., J. E. Vidale, and Y. G. Li, Near-fault anisotropy following the Hector Mine earthquake, *J. Geophys. Res*. **108**, B9, 2436-2447, ESE 11, 2003.

Dieterich, J. H., Time-dependent friction and the mechanics of strike-slip. *Pure Appl. Geophys*., **116**, 790-806, 1978.

Dodge, D., and G. C. Beroza, Source array analysis of coda waves near the 1989 Loma Prieta, California mainshock: Implications for the mechanism of coseismic velocity changes, *J. Geophys. Res.* **102**, 24,437-24,458, 1997.

Eberhart-Phillips, D., and A. J. Michael, Three-dimensional velocity structure, seismicity, and fault structure in Parkfield region, central California *J. Geophys. Res.* **98**, 15737-15758, 1993.

Ellsworth, W. L, A. T. Cole, G. C. Beroza, and M. C. Verwoerd, Changes in crustal wave velocity association with the 1989 Loma Prieta, California earthquake, *EOS* **73**, 360, 1992.

Fialko, Y., D. Sandwell, D. Agnew, M. Simons, P. Shearer, B. Minster, Deformations on nearby faults induced by the 1999 Hector Mine earthquake, *Science*, **297**, 1858-1862, 2002.

Garbin, H. D., and L. Knopoff, Elastic moduli of a medium with liquid-filled cracks, *Quart. Appl. Math. October*, **32**, 301-303, 1975.

Graves, R. W., Simulating seismic wave propagation in 3D elastic media using staggered-grid finite differences, *Bull. Seismol. Soc. Am.*, **86**, 1091-1106, 1996.

Hickman, S. H., and B. Evans, Growth of grain contacts in halite by solution-transfer: Implications for diagenesis, lithification, and strength recovery, in *Fault Mechanics and Transport Properties of Rocks*, pp. 253-280, Academic, San Diego, Calif., 1992.

Hickman, S. H., M. D. Zoback, and W. L. Ellsworth, Structure and Composition of the San Andreas fault zone at Parkfield: Initial results from SAFOD Phase 1 and 2, *EOS, Transactions, American. Geophysics Union*, **83**, No.47, 237, 2005.

Ikuta, R., and K. Yamaoka, Temporal variation in the shear wave anisotropy detected using the accurately controlled routinely

operated signal system (ACROSS), *J. Geophys. Res.* **109**, B09305, doi:10.1029/2003JB002901, 2004.

Kanamori, H., Mechanics of earthquakes, *Ann. Rev. Earth Planet., Sci.*, **22**, 207-237, 1994.

Karageorgi, E., R. Clymer, and T. McEvilly, Seismological studies at Parkfield: II: Search for temporal variations in wave propagation using vibroseis, *Bull. Seism. Soc. Am.* **82**, 1388-1415, 1992.

Karageorgi, E. D., T. V. McEvilly, and R. W. Clymer, Seismological studies at Parkfield: IV: Variations in controlled-source waveform parameters and their correlation with seismicity, 1987 to 1995, *Bull. Seism. Soc. Am.* **87**, 39-49, 1997.

Korneev, V. A., T. V. McEvilly, and E. D. Karageorgi, Seismological studies at Parkfield VIII: Modeling the observed travel-time changes, *Bull. Seism. Soc. Am.* **90**, 702-708, 2000.

Korneev, V. A., R. M. Nadeau, and T. V. McEvilly, Seismological studies at Parkfield IX: Fault-zone imaging using guided wave attenuation, *Bull. Seism. Soc. Am.* **80**, 1245-1271, 2003.

Langbein, J., R. Bocherdt, D. Dreger, J. Fletcher, J. L. Hardbeck, M. Hellweg, C. Ji, M. Johnston, J. R. Murray, R. Nadeau, M. J. Rymer, and J. A. Trieman (2005). Preliminary report on the 28 September 2004, M 6.0 Parkfield, California earthquake, *Seism. Res. Lett.* **76**, No. 1, 10-26.

Lees, J. M., and P. E. Malin, Tomographic images of *P* wave velocity variation at Parkfield, California, *J. Geophys. Res.* **95**, 21,793-21,804, 1990.

Li, Y. G., P. C. Leary, K. Aki, and P. E. Malin, Seismic trapped modes in Oroville and San Andreas fault zones, *Science*, **249**, 763-766, 1990.

Li, Y. G., W. L. Ellsworth, C. H. Thurber, P. E. Malin, and K. Aki, Observations of fault-zone trapped waves excited by explosions at the San Andreas fault, central California, *Bull. Seism. Soc. Am.* **87**, 210-221, 1997.

Li, Y. G., J.E. Vidale, K. Aki, F. Xu, and T. Burdette, Evidence of shallow fault zone strengthening after the 1992 *M*7.5 Landers, California, earthquake, *Science*, **279**, 217-219, 1998.

Li, Y. G. and J. E. Vidale, Healing of the shallow fault zone from 1994-1998 after the 1992 *M*7.5 Landers, California, earthquake, *Geophys. Res. Lett.* **28**, 2999-3002, 2001.

Li, Y. G., J. E. Vidale, S. M. Day, D. D. Oglesby, and E. Cochran, Post-seismic fault healing on the 1999 *M*7.1 Hector Mine, California earthquake, *Bull. Seism. Soc. Am.* **93**, 854-869, 2003.

Li, Y. G., J. E., Vidale, and S. E. Cochran, Low-velocity damaged structure on the San Andreas fault at Parkfield from fault-zone trapped waves, *Geophys. Res. Lett.* **31**, L12S06, p1-5, 2004.

Li, Y. G., Po Chen, E. S. Cochran, J. E. Vidale, and T. Burdette, Seismic evidence for rock damage and healing on the San Andreas fault associated with the 2004 *M*6 Parkfield earthquake, Special issue for Parkfield *M*6 earthquake, *Bull. Seism. Soc. Am.*, **96**, pp. S1-S, doi: 10.1785/0120050803, 2006.

Lockner, D. A., H. Naka, H. Tanaka, H. Ito, and R. Ikeda, Permeability and strength of core samples from the Nojima fault of the 1995 Kobe earthquake, *in Proceedings of the International Workshop on the Nojima Fault Core and Borehole Data Analysis*, Tsukuba, Japan, Nov 22-23, 1999, USGS Open file Report 00-129, edited by H. Ito, K. Fujimoto, H. Tanaka, and D. A. Lockner, 147-152, 2000.

Marone, C., J. E. Vidale and W. L. Ellsworth, Fault healing inferred from time dependent variations in source properties of repeating earthquakes, *Geophys. Res. Lett.* **22**, 3095-3098, 1995.

Marone, C., The effect of loading rate on static friction and the rate of fault healing during the earthquake cycle, *Nature*, **391**, 69-72, 1998.

Michelini, A., and T. V. McEvilly, Seismological studies at Parkfield, I, Simultaneous inversion for velocity structure and hypocenters using cubic B-splines parameterization, *Bull. Seism. Soc. Am.* **81**, 524-552, 1991.

Massonnet, D, W. Thatcher, and H. Vadon, Detection of postseismic fault-zone collapse following the Landers earthquake, *Nature*, **382**, 612-616, 1996.

Mooney, W. D., and A. Ginzburg, Seismic measurements of the internal properties of fault zones, *Pure Appl. Geophys.* **124**, 141-157, 1986.

Niu F. L., P. G. Silver, R. M. Nadeau, and T. V. McEvilly, Stress-induced migration of seismic scatters associated with 1993 Parkfield aseismic transient event, *Nature*, **426**, 544-548, 2003.

Nur. A., Dilatancy, Pore fluid, and premonitory variations of ts/tp travel times, *Bull. Seismol. Soc. Am.* **62**, 1217-1222, 1972.

O'Connell, R. J., and B. Budiansky, Seismic velocities in dry and saturated cracked solids, *J. Geophys. Res.* **79**, 5412-5426, 1974.

Olsen, M., C. H. Scholz, and A. Leger, Healing and sealing of a simulated fault gouge under hydrothermal conditions for fault healing, *J. Geophys. Res.* **103**, 7421-7430, 1998.

Rice, J., R., The mechanics of earthquake rupture, In Physics of the Earth's Interior, A. M. Dziewonski and B. Boschi (Editors), North-Holland, Amsterdam, 555-649, 1980.

Rice, J. R., Fault stress states, pore pressure distributions, and the weakness of the San Andreas fault, in *Fault Mechanics and Transport Properties of Rocks*, edited by B. Evans and T.-F. Wong, pp. 475-503, Academic, San Diego, Calif., 1992.

Richardson, E., and C. Marone, Effects of normal stress vibrations on frictional healing, *J. Geophys. Res*. **104**, 28,859-28,878, 1999.

Rubinstein, Justin, and G. C. Beroza, Depth constrain on nonlinear strong ground motion from the 2004 Parkfield earthquake, submitted to *Seism. Res. Lett.* **32**, L14313, doi: 10.1029/2005GL023189, 2005.

Schaff, D. P., and G. C., Beroza, Coseismic and postseismic velocity changes measured by repeating earthquakes, *J. Geophys. Res.* **109**, B10302, doi: 10.1029/2004JB003011, 2004.

Scholz, C. H., *The Mechanics of Earthquakes and Faulting*, Cambridge Univ. Press, New York, 1990.

Sibson, R. H., Fault rocks and fault mechanisms, *J. Geol. Soc. London*, **133**, 191-213.

Snieder, R., and M. Vrijlandt, Constraining Relative Source Locations with Coda Wave Interferometry: Theory and Application to Earthquake Doublets in the Hayward Fault, California, *J. Geophys. Res.*, **110,** B04301, 10.1029/2004JB003317, 2005.

Tadokoro, K, M. Ando and Y. Umeda (1999). *S* wave splitting in the aftershock region of the 1995 Hyogo-ken Nanbu earthquake, *J. Geophys. Res*., **104**, 981-991, 1997.

Thurber, C. H., S. Roecker, W. Ellsworth, Y. Chen, W. Lutter, and R. Sessions, Two-dimensional seismic image of the San Andreas fault in the northern Gabilan Range, central California: Evidence for fluids in the fault zone, *Geophys. Res. Lett.* **24**, 1591-1594, 1997.

Unsworth, M., P. Malin, G. Egbert, and J. Booker, Internal structure of the San Andreas fault at Parkfield, CA, *Geology*, 356-362, 1997.

Vidale, J. E., W. L. Ellsworth, A. Cole, and C. Marone, Rupture variation with recurrence interval in eighteen cycles of a small earthquake, *Nature*, **368**, 624-626, 1994.

Vidale, J. E. and Li, Y. G., Damage to the shallow Landers fault from the nearby Hector Mine earthquake, Nature, 421, 524-526, 2003.

Yasuhara, H., C. Marone, and D., Ellsworth, Fault zone restrengthening and frictional healing: The role of pressure solution, *J. Geophys. Res.* **110**, B06310, doi:10.1029/2004JB003327, 2005.

Y.G. Li (e-mail: ygli@usc.edu), P. Chen, E. S. Cochran, and J. E. Vidale.

Low-Velocity Damage Zone on the San Andreas Fault at Depth near SAFOD Site at Parkfield Delineated by Fault-Zone Trapped Waves

By Yong-Gang Li, John E. Vidale, and Peter E. Malin

Abstract We deployed a dense linear array of 45 seismometers across and along the San Andreas fault near the SAFOD site at Parkfield in 2003 to record fault-zone trapped waves generated by near-surface explosions and microearthquakes located within the fault zone. Observations and simulations of the fault-zone trapped waves show a ~150-200-m-wide low-velocity waveguide along the SAF, within which shear velocities are reduced by 20-40% from wall-rock velocities and the *Q* value of fault-zone rocks is 10-50, indicating the existence of a damage zone on the major plate boundary at Parkfield. The damage zone on the SAF extends across seismogenic depths to at least ~7 km and is not symmetric but extends farther on the southwest side of the main fault trace. The width and velocities of this zone delineated by fault-zone trapped waves recorded at surface arrays are consistent with the results from SAFOD drilling and logs that show high porosity and multiple slip planes in a ~200-m-wide low-velocity zone with velocity reduction of ~20-30% on the main SAF at ~3.2 km depth [Hickman, 2005]. Recently, down-hole seismic stations within the main fault zone at this depth also registered prominent fault-zone guided waves from microearthquakes occurring below, indicating that the low-velocity waveguide on the SAF extends to the deeper seismogenic level [Malin, et al., 2006].

1. Introduction

The spatial extent of fault weakness, and the loss and recouping of strength across the earthquake cycle are critical ingredients in our understanding of fault mechanics. In order to relate present-day crustal stresses and fault motions to the geological structures formed in their past earthquake histories, we must understand the evolution of fault systems on many spatial and time scales. Extensive field and laboratory research, and numerical simulations indicate that fault zones undergo high, fluctuating stress and pervasive cracking during a earthquake [e.g., Aki, 1984; Chester et al., 1993]. While we know slip is localized on faults because of their lower strength compared to the surrounding bedrock, critical parameters remain unknown. For example, friction laws are approximate [e.g., Richardson and Marone, 1999], and the magnitude of strength reduction and its spatial extent at seismogenic depth are still not well constrained [e.g., Hickman and Evans, 1992].

Near Parkfield, CA, many researchers have observed a low-velocity zone surrounding the surface trace the San Andreas fault [e.g. Thurber *et al.*, 2003; Unsworth *et al.*, 1997; Roecker *et al.*, 2004]. This zone is from a few hundred meters to 1 km wide, and has velocity reductions of 10-30% and *Vp/Vs* ratios on the order of 2.3. The low-velocity zone is thought to be caused by intense fracturing during earthquakes, brecciation, liquid-saturation and possibly high pore-fluid pressures near the fault core. Recent results from drilling logs at the Parkfield San Andreas Fault Observatory at Depth show a low velocity zone more than one hundred meters wide at ~3 km depths, indicating a damage zone associated with the San Andreas Fault Zone (SAFZ) [Hickman *et al.*, 2005]. Pore fluids arising from depth appear to hold a complex relationship with this damage zone, with its outer portions appearing to be more permeable than its core [Rice, 1992; Lockner *et al*., 2000].

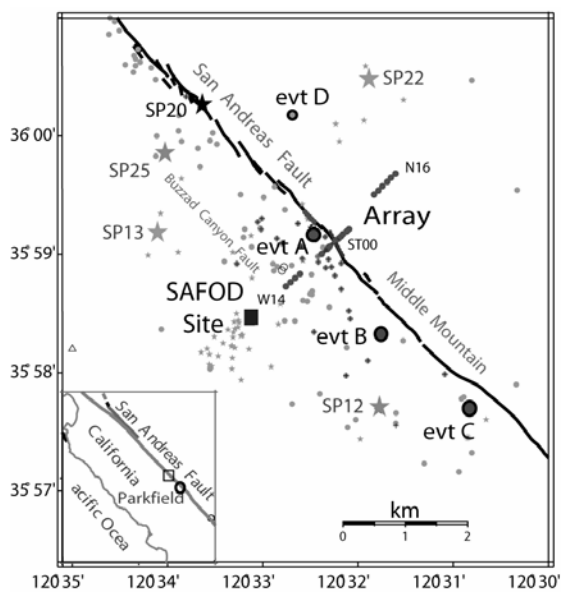

Figure 1 Map shows locations of linear seismic arrays of 45 PASSCAL RT130s (circles in line) deployed across and along the San Andreas fault near the SAFOD site (square), 5 explosions (stars) detonated by USGS, small shots (stars) and microearthquakes (dots) recorded at our array in the fall of 2003. Station ST0 in array was located on the main fault trace. Dark dots denote 37 earthquakes at different depths showing fault-zone trapped waves and are used for measurements shown in Fig. 3. Event A (2931125) is a *M*2.2 SAFOD target event occurring at ~3 km depth on Julian date R293 in 2003. Events B (2940516), C (2930452), and D (2931210) are deep earthquakes. Waveforms from them are shown in Fig. 2.

Recently, prominent fault-zone guided waves have been recorded in the SAFOD main-hole at ~3 km depth, suggesting that a SAFZ-related low-velocity waveguide extends to deeper levels [Malin et al., 2006]. In this article, we discuss the fault-zone trapped waves recorded at the linear seismic array deployed across the SAFZ near the SAFOD site in 2003. The data from local microearthquakes occurring at different depths provide better constraints on the depth extent of the damage structure of the SAF. These results help extend the direct measurements of fault-zone properties in the SAFOD main hole to a 3-D structural image of the SAFZ.

2. Data and Results

Many seismic and geophysical surveys conducted near the SAFOD site ~15 km NW of Parkfield in 2003 have provided useful structural information before the SAFOD drilling through the plate boundary. Coordinated by SAFOD PIs, we deployed a dense linear seismic array of 45 PASSCAL RT130 three-component seismometers across and along the San Andreas fault to record fault-zone trapped (guided) waves for seismic site characterization (Fig. 1). During the experiment, we recorded ~100 local earthquakes at depths between 2 and 12 km and 5 explosions in the fan-geometry detonated by the USGS. The data show prominent fault-zone trapped waves generated by the events located within the fault zone and have been used to delineate the internal damage structure and physical properties of the SAF at seismogenic depths.

Figure 2 exhibits seismograms recorded at cross-fault array for 3 microearthquakes near the SAFOD site, showing prominent fault-zone trapped waves (FZTW) with large amplitudes and long wavetrains after *S*-arrivals at stations close to the SAF main trace in a width range of ~150-200-m for events A and B occurring within the fault zone. In contrast, trapped waves are not clear at the same stations for event C occurring 1.5 km away from the fault zone, and stations located out of the fault zone register brief body waves for 3 events. Note some seismic energy trapped within a branch fault (BF) which may connect to the main fault trace at depth. Recently, the bore seismograms recorded in the SAFOD main hole at 3.2 km depth show prominent fault-zone guided waves partitioned from the main fault to this branch fault [*Chavarria et al.*, 2004; *Malin et al.*, 2006]. We also note that fault-zone trapped waves from event C occurring at ~11 km depth show much longer wavetrains of the FZTW after S-arrivals than those generated by shallow event A at ~3 km depth, indicating that the low-velocity waveguide on the SAF likely extends to deep seismogenic level. In contrast, wavetrains after *S*-arrivals at the same stations for the off-fault event D at ~9 km depth are much shorter than those from event C although two events occurred at the similar depth and distance from array.

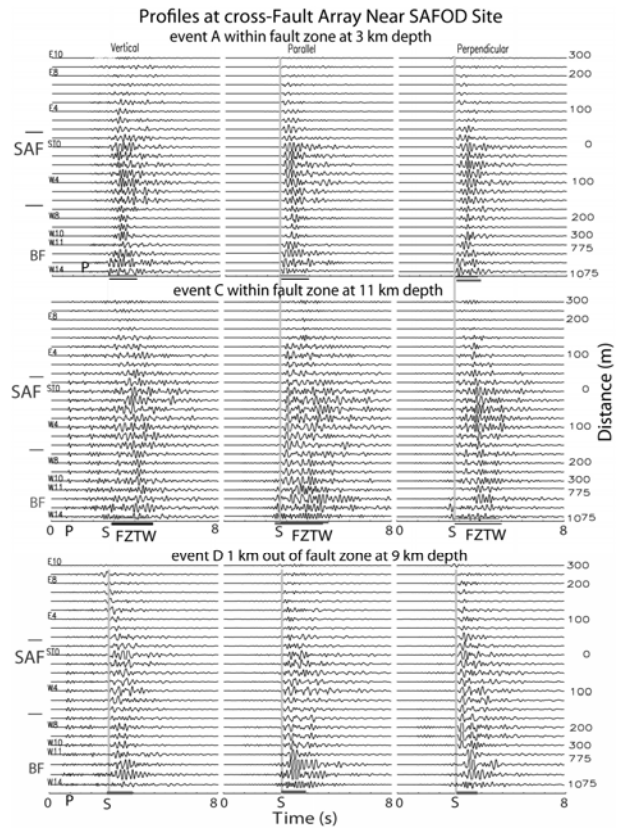

Figure 2 (a) Three-component seismograms at the cross-fault array for 3 micro earthquakes occurring within and out of the fault zone, Station names and distances from the main fault trace (SAF) are denoted. Seismograms have been (<6 Hz) filtered and plotted in a fixed amplitude scale in each plot. Prominent fault-zone trapped waves (FZTW) appear at stations between E6 and W4, indicating a ~150-200-m wide low-velocity waveguide along the SAF. Vertical lines are aligned with *S* arrivals from these events. The solid bar denotes the length of trapped wavetrains after *S*-waves. The length of FZTW from the deeper event C at ~11 km is ~2.2 s much longer that ~1.2 s length of FZTW from event A at ~3 km, indicating that the low-velocity waveguide likely extends to the deep part of seismogenic zone. In contrast, the wavetrain after *S*-arrival for the off-fault event D at the same depth of event C is much shorter than that for event C within the fault zone. Note that some seismic energy was trapped within a branch fault (BF) of the SAF.

In order to examine the depth extension of the low-velocity zone on the SAF, we used the data from 37 local earthquakes located within the fault zone at different depths with the raypath incidence angles to the array smaller than 30° from vertical (Fig. 3a). Figure 3b shows seismograms and envelopes at station ST0 located on the main fault trace for 11 on-fault events at different depths near SAFOD site. *S*-arrivals for these events are aligned at 2 s. The length of fault-zone trapped wavetrains following *S*-arrivals progressively increases from ~1.2 s to ~2.2 s as the event depths increase from 2.6 km to 11.7 km. In contrast, much shorter wavetrains after *S*-arrivals with flat changes in

length are registered at the same station for 11 other events located away from the fault zone in the similar depth range. In Figure 3d, we plot the measured FZTW wavetrain lengths for 37 on-fault events and 13 off-fault events at depths between 2 km and 12 km, showing that the lengths of FZTW wavetrains at stations within the fault zone for on-fault events increase from 1.0 s to 2.2 s as the depth increases from ~2 km to ~12 km, but shorter wavetrains with flat depth-dependent changes are seen at the same stations for off-fault events. Stations located out of the fault zone registered short wavetrains after *S*-arrivals for all these events. These observations indicate that the low-velocity waveguide (damage zone) on the SAF extends across seismogenic depths to at least 7-8 km although the velocity reduction within the zone becomes smaller with depth due to the larger confined stress at greater depths.

Based on our observations of fault-zone trapped waves, we construct a velocity and *Q* model across the SAF near the SAFOD site as shown in Fig. 4d. The wall-rock velocities are constrained by tomography profiles at Parkfield [Thurber *et al.*, 2003; Roecker *et al.*, 2003]. Using a 3-D FD code [Graves, 1996], we simulated FZTW generated by explosions to determine the shallow 1 or 2 km fault zone structure, and then simulated trapped waves from earthquakes to obtain a model of the SAF with depth-variable structure at seismogenic depths. The model parameters at 3 km depth are constrained by direct measurements of the fault zone width and velocities in the SAFOD main hole [Hickman *et al*., 2005]. Figure 4 shows FD simulations of FZTW for explosion SP20 detonated within the fault zone at ~3 km north of the SAFOD site and 2 on-fault earthquakes event A and B at depths of 3 km and 7 km, respectively. The earthquake at 3 km is a SAFOD target event occurring on R293 of 2003. We obtained a good fit of synthetics to seismograms recorded at our cross-fault array. The source at 7 km depth within the fault zone generates longer FZTW wavetrains after *S*-waves than those from a source at 3 km depth, agreeable with observations, indicating our model is applicable for the fault-zone structure near the SAFOD site. We have tested finite-difference simulations for the deep event at 7 km but using a model with a low-velocity waveguide at shallower depth of 3 km. The synthetic seismograms showed a shorter wavetrain after *S*-arrivals and could not match observed long wavetrains for this deep event.

Using the fault-zone model in Fig. 4d, we simulated seismograms (Fig. 3c) at station ST0 on the main fault trace for 11 on-fault earthquakes and 11 off-fault earthquakes at depths between 3.6 km and 11.2 km for comparison with observed seismograms (Fig. 3b) for these events. The lengths of synthetic FZTW wavetrains increase with the event depth, agreeable with our observations shown in Fig. 3b. These results further verify the existence of a low-velocity waveguide (damage zone) on the SAF at Parkfield that likely extends to seismogenic depths deeper than ~7 km.

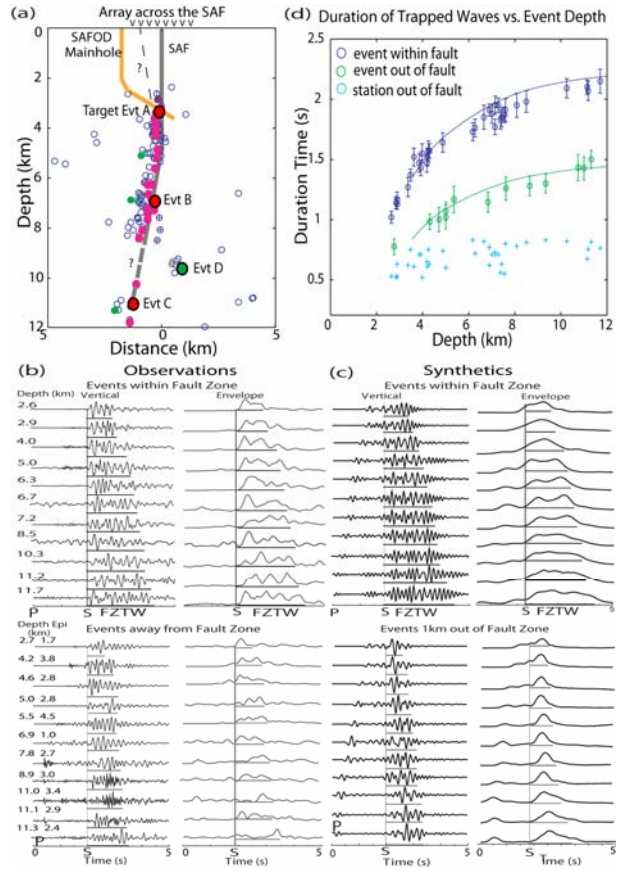

Figure 3 (a) Vertical section across the SAF and the SAFOD site shows locations of microearthquakes recorded at our seismic array in 2003. Dark (red) circles denote earthquakes showing prominent fault-zone trapped waves with long wavetrains after *S*-arrivals. Gray (green) circles denote events showing short wavetrains after *S*-arrivals. The deep part of the SAF dips toward SW at high angle. Waveforms from events A-D are shown in Fig. 2. The SAF and a branch fault (dashed lines) may connect at depth. (b) top: Vertical-component seismograms and envelopes recorded at station ST0 on the SAF main trace for 11 on-fault zone earthquakes at different depths and with the raypath incidence angle <30° from vertical show an increase in wavetrain length (marked by solid bar) of fault-zone trapped waves (FZTW) as event depths increase. *S*-arrivals for all these events are aligned in plot. Bottom: The same plot but for 11 off-fault events between the similar depths shows much shorter wavetrains after *S*-arrivals and flat changes with event depths. (c) Finite-difference synthetic seismograms and envelops at station ST0 for 11 on-fault and 11 off-fault events at different depths using the fault-zone structural model in Fig. 4d show the increasing trend of FZTW wavetrain lengths of FZTW for on-fault events agreeable with observations. In computation, the average epicentral distance of these events are 2-km from station ST0. (d) The wavetrain lengths after *S*-arrivals versus event depths for earthquakes occurring within and out of the fault zone. Each data point is averaged from measurements at 4 stations close to or far away from the fault for on-fault. Error bars are standard deviations. Curves are polynomial fits to the data. Crosses are measurements at stations located 300-m away from the fault for all these events. Plots indicate that the low-velocity zone on the SAF extends across seismogenic depths.

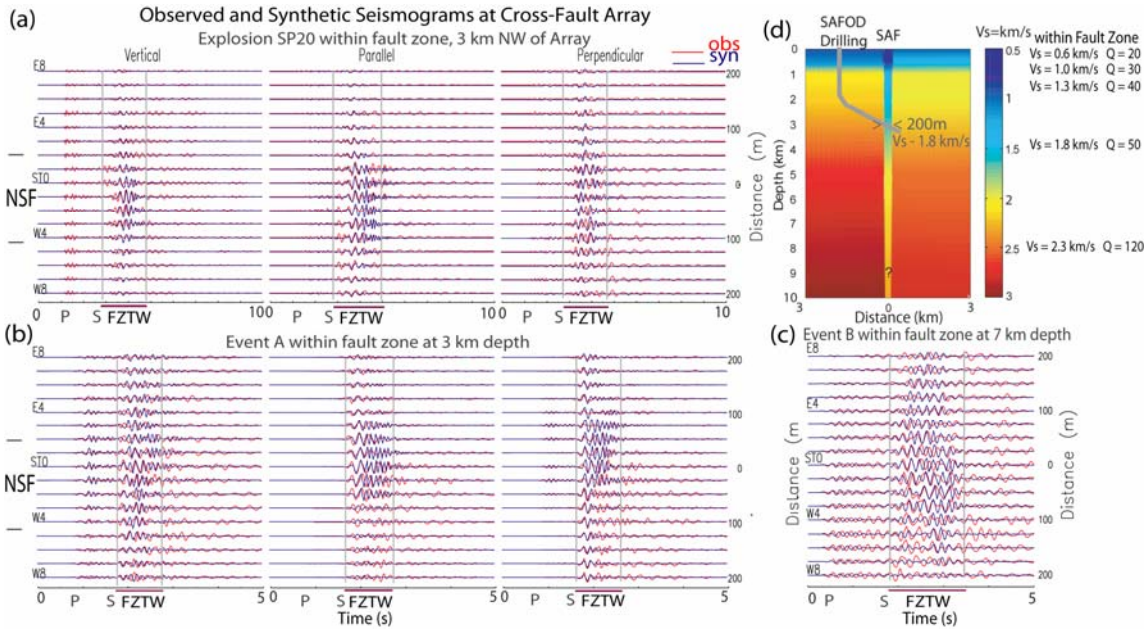

Figure 4 (a) Observed and 3-D finite-difference synthetic seismograms in three-components using model parameters shown in (d) for an explosion SP20 detonated within the fault zone, ~3 km northwest of the array. Other notations are the same in Fig. 2. (b) Same as in (a), but for the SAFOD target event A occurring at 3 km depth within the fault zone. (c) Vertical-component of observed and FD synthetic seismograms for a microearthquake event B occurring at ~7 km depth within the fault zone. *S*-arrivals are aligned at the same time for event B with event A, showing longer FZTW wavetrains for the deeper event C. A double-couple source is used for earthquakes while an explosion source is used for the shot. The FZTW wavetrains from the deeper event C is longer than that from event A. (d) Cross-fault depth sections show the structural model near the SAFOD site. Model parameters within a 100-200-m-wide low-velocity waveguide on the SAF are obtained from 3-D finite-difference simulations best fit to observed waveforms generated by explosions and earthquakes at different depths. *S* velocities within the waveguide are reduced by 25-40% from wall-rock velocities that are not symmetric at two sides of the SAF. The width and *S* velocity of the low-velocity fault zone at 3.2 km depth shown in the model are from the direct measurements in the SAFOD main hole.

3. Conclusion

Observations and modeling of fault-zone trapped waves recorded at dense linear seismic arrays deployed near the SAFOD site, Parkfield show the existence of a distinct low-velocity damage zone along the SAF and extending across seismogenic depths. The structural model for the SAF shown in Fig. 4d is still a simple one although it explains part of the data. The true structure in 3-D may be more complicated. It will be elucidated through a detailed study using the data recorded at surface and in the SAFOD main hole.

Acknowledgments. This study is supported by EarthScope Grant EAR0342277, USGS Grant NEHRP20060160, and the SCEC. Special thanks to S. Hickman, W. Ellsworth, and M. Zoback for their coordination, and E. Cochran, C. Thurber, S. Roecker, M. Rymer, R. Catchings, A. Snyder, L. Powell, B. Nadeau, N. Boness, and D. McPhee for their collaborations in our experiments at Parkfield. The author was supported by the ICDP to attend the ICDP-IODP Fault-Zone Drilling Workshop at Japan in 2006.

References

Aki, K., Asperities, barriers, characteristic earthquakes, and strong motion prediction, *J. Geophys. Res*. **89**, 5867-5872,1984.

Chavarria, J. A., P. E. Malin, E. Shalev, and R.D. Catchings. A look inside the San Andreas Fault at Parkfield through Vertical Seismic Profiling. *Science*, **302**, 1746-1748, 2004.

Chester F., J. Evans and R. Biegel, Internal structure and weakening mechanisms of the San Andreas fault, *JGR*. **98**, 771-786, 1993.

Hickman, S. H., and B. Evans, Growth of grain contacts in halite by solution-transfer: Implications for diagenesis, lithification, and strength recovery, in *Fault Mechanics and Transport Properties of Rocks*, pp. 253-280, Academic, San Diego, Cal., 1992.

Hickman, S. H., M. D. Zoback, and W. L. Ellsworth, Structure and Composition of the San Andreas fault zone at Parkfield: Initial results from SAFOD Phase 1 and 2, *EOS*, **83**, No.47, 237, 2005.

Li, Y. G., P. Leary, K. Aki, and P. Malin, Seismic trapped modes in Oroville and San Andreas fault zones, *Science*, **249**, 763-766,1990.

Li, Y. G., W. Ellsworth, C. Thurber, P. Malin, K. Aki, Observations of fault-zone trapped waves excited by explosions at the San Andreas fault California, *Bull. Seism. Soc. Am.* **87**, 210-221, 1997.

Li, Y. G., J. E., Vidale, and S. E. Cochran, Low-velocity damaged structure on the San Andreas fault at Parkfield from fault-zone trapped waves, *Geophys. Res. Lett.* **31**, L12S06, p1-5, 2004.

Lockner, D., H. Naka, H. Tanaka, H. Ito, and R. Ikeda. Permeability and strength of core samples from the Nojima fault of the 1995 Kobe earthquake, USGS Open file, Report 00-129, 147-152, 2000.

Malin, P. M., E. Shalev, H. Balven, C. Lewis-Kenedi, New fault structure on the San Andreas fault at SAFOD from P-wave tomography and fault guided waves mapping, *GRL*, in press, 2006.

Rice, J. R., Fault stress states, pore pressure distributions, and the weakness of the San Andreas fault, in *Fault Mechanics and Transport Properties of Rocks*, 475-503, 1992.

Richardson, E., and C. Marone, Effects of normal stress vibrations on frictional healing, *J. Geophys. Res*. **104**, 28,859-28,878, 1999.

Thurber, C., S. Roecker, K. Roberts, M. Gold, L. Powell, and K. Rittger, Earthquake location and 3-D fault zone structure along the creeping section of the San Andreas fault near Parkfield, CA: Preparing for SAFOD, *Geophys. Res. Lett.* **30**, 1112-1115, 2003.

Unsworth, M., P. Malin, G. Egbert and J. Booker, Internal structure of San Andreas fault at Parkfield, CA, *Geology*, 356-362, 1997.

Y.G. Li (University of Southern California, e-mail: ygli@usc.edu),
J. E. Vidale (UCLA) and P. E. Malin (Duke).

Bulletin of the Seismological Society of America, Vol. 96, No. 4B, pp. S364–S375, September 2006, doi: 10.1785/0120050804

Anisotropy in the Shallow Crust Observed around the San Andreas Fault Before and After the 2004 **M** 6.0 Parkfield Earthquake

by Elizabeth S. Cochran,* Yong-Gang Li, and John E. Vidale

Abstract Local seismic arrays were deployed at two locations along the San Andreas fault (SAF) near Parkfield, California, before and after the 2004 **M** 6.0 Parkfield earthquake. Using local earthquakes we determine the anisotropic field within 1–2 km of the main trace of the SAF at the two array locations separated by 12 km. The initial array, near the SAFOD site, was deployed for six weeks in October and November 2003, and the second array, located near the town of Parkfield, was deployed for 3 months following the 28 September 2004 **M** 6.0 Parkfield earthquake.

We find the fast shear-wave polarization direction nearly fault-parallel (N40°W) for stations on the main fault trace and within 100 m to the southwest of the SAF at both array locations. These fault-parallel measurements span the 100- to 150-m-wide zone of pervasive cracking and damage interpreted from fault-zone-trapped waves associated with the main fault core (Li *et al.*, 2004, 2006). Outside of this zone, the fast orientations are scattered with some preference for orientations near N10°E, roughly parallel to the regional maximum horizontal compressive stress direction (σ_h). In addition, fast directions are preferentially oriented parallel to a northern branch of the SAF recorded on stations in the 2004 Parkfield deployment.

The measured anisotropy is likely due to a combination of stress-aligned microcracks away from the fault and shear fabric within the highly evolved fault core. The majority of our measurements are taken outside of the main fault core, and we estimate the density of microcracks from the measured delay times. Apparent crack densities are approximately 3%, with large scatter. The data suggest weak depth dependence to the measured delay times for source depths between 2 and 7 km. Below 7-km source depth, the delay times do not correlate with depth suggesting higher confining pressure is forcing the microcracks to close.

No coseismic variation in the anisotropic parameters is observed, suggesting little to no influence on measured splitting due to the 2004 **M** 6.0 Parkfield earthquake. However, the premainshock and postmainshock data presented here are from arrays separated by 12 km, limiting our sensitivity to small temporal changes in anisotropy.

Introduction

We examine crustal shear-wave anisotropy at two locations along the San Andreas fault (SAF) near Parkfield to investigate lateral and possible temporal variation in anisotropy. Local earthquake data were recorded on seismic arrays prior to and following the 28 September 2004 Parkfield **M** 6.0 earthquake. The data are from one array deployed in October and November 2003, and a second immediately after the **M** 6.0 mainshock. The 2003 array, referred to hereafter as the SAFOD array, is located adjacent to the SAFOD drilling site and the 2004 array, referred to as the Parkfield array, is located 12 km to the southeast along the main trace of the SAF (Fig. 1). During the SAFOD deployment in 2003, prior to the **M** 6.0 earthquake, the background seismicity was moderate, so we have a small but sufficient number of records to compare to the hundreds of aftershock records from 2004. The main points we address in this article are as follow: (1) the lateral variation in anisotropy along the SAF, (2) the physical cause of the observed anisotropy, and (3) the absence of a temporal change in the anisotropic parameters due to the 2004 **M** 6.0 Parkfield earthquake.

Shear-wave splitting studies have long been conducted to estimate the *in situ* stress field in the shallow crust. Shear

*Present address: Institute of Geophysics and Planetary Physics, Scripps Institution of Oceanography, University of California at San Diego, La Jolla, California 92093-0225.

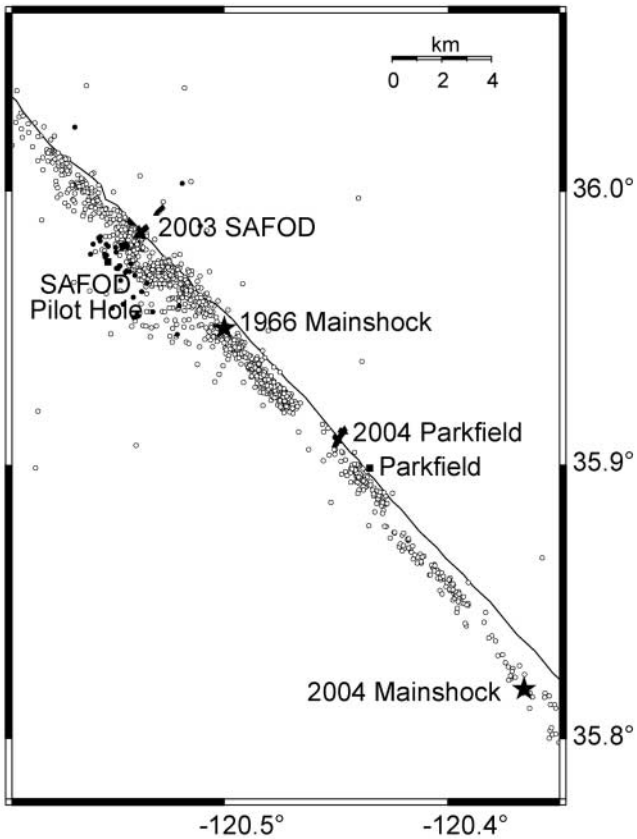

Figure 1. Map of Parkfield segment of the San Andreas fault (SAF). The 2003 and 2004 station locations are given by the filled triangles. The filled circles show earthquakes that occurred during the 2003 deployment. Aftershocks of the 2004 **M** 6.0 Parkfield earthquake that occurred during the 2004 deployment are shown by the open circles. Seismicity is likely concentrated close to the main fault plane, but catalog locations are offset to the southwest due to the large velocity contrast across the fault. The 1966 and 2004 **M** 6.0 mainshock epicenters are show by the filled stars. The town of Parkfield and the SAFOD drilling site are shown by filled squares.

waves are sensitive to compliance and wave speed that varies with polarization direction. Aligned cracks or shear fabric in the medium are the most common causes of the observed anisotropy in the upper crust (Boness and Zoback, 2004a; Crampin, 1990; Crampin and Chastin, 2003; Crampin and Zatsepin, 1997; Hudson, 1994; Zatsepin and Crampin, 1997). In the case of aligned cracks, shear-wave splitting analysis allows us to equate the fast direction with the crack orientation and the delay time with the density of cracks for each source-receiver path. Alternately, if anisotropy is due to shear fabric the anisotropic parameters relate to direction of fabric and degree of shearing. The inherent variability in anisotropic measurements requires that a significant number of records be collected to estimate the crack field or shear fabric.

Anisotropy, whether due to aligned microcracks or shear fabric, is useful to detail the structure and stress state of the fault. Aligned microcracks are thought to be sensitive to perturbations in the local stress field near an active fault and are often invoked to search for temporal changes in the stress field. Fast directions have been shown to rotate spatially, with orientations nearly fault-parallel for stations located on or very close to a fault (e.g., Peng and Ben-Zion, 2004; Tadokoro *et al.*, 1999). Analysis of focal mechanism inversions also suggest a 10° to 30° rotation in the stress field within 1–10 km from the SAF (Hardebeck and Michael, 2004; Provost and Houston, 2001; Townend and Zoback, 2004). However, the focal mechanism studies have not agreed upon the angle of the maximum local stress orientation to the strike of the SAF. The above focal mechanism inversion studies estimate that the maximum compressive stress is rotated 30° to 60° clockwise from the SAF strike in the Parkfield region.

At present, few detailed near-fault studies of the anisotropy have been conducted to search for a rotation of the stress field near an active fault. We employ two dense seismic arrays spanning 1 km and 2.4 km across the SAF to determine the orientation of the main anisotropic feature and look for lateral changes in anisotropic parameters. While the permanent array stations deployed near Parkfield provide extended temporal coverage of the anisotropic field, they cannot be used to examine 10- to 100-m spatial variations across the fault, as they are widely spaced.

A recent study by Boness and Zoback (2004a) details the anisotropic structure observed by SAFOD pilot hole stations prior to the mainshock. The multiple datasets collected in the pilot hole allow the authors to correlate the measured shear-wave splitting with observations of macrocracks, borehole breakouts, and wave speeds at depth. Boness and Zoback (2004a) suggest that the observed anisotropy is likely due to both aligned microcracks and localized shear fabric. The pilot hole is located several kilometers from the main fault strand, so they only examine the anisotropic field at one locale away from the fault. However, their study is useful to map the observed anisotropy to a physical mechanism.

Whether shear-wave splitting measurements are sensitive to changes in the local stress field during a mainshock has remained contentious. Several shear-wave splitting studies near recently ruptured fault zones have claimed to see temporal evolution of the crack field following a large magnitude earthquake or prior to earthquake swarms (e.g., Gao *et al.*, 1998; Tadokoro *et al.*, 1999; Teanby *et al.*, 2004). However, a variety surveys have seen no postseismic change in anisotropic parameters in the months following large magnitude earthquakes (e.g., Cochran *et al.*, 2003; Peng and Ben-Zion, 2004). A recent study by Boness and Zoback (2004b) of the anisotropy observed on the permanent Parkfield array stations showed no coseismic change in the anisotropy following the 2004 **M** 6.0 Parkfield earthquake. This result is somewhat surprising, given the clear coseismic changes observed in *P, S*, and trapped waves associated with

large magnitude earthquakes (Li *et al.*, 1998, 2003, 2006; Rubinstein and Beroza, 2004; Schaff and Beroza, 2004). However, a recent study by Peng and Ben-Zion (2005) suggests that shear-wave splitting studies are not sensitive to small changes in the microcrack field because the velocity change influences both the fast and slow quasipolarized shear waves. We examine the local array data for an evidence of coseismic perturbation of the observed anisotropy near the SAF due to the 2004 **M** 6.0 Parkfield earthquake.

Seismic Array Deployments

Seismic arrays were deployed along the SAF at Parkfield in two locations in 2003 and 2004. The 2003 SAFOD array was deployed near the SAFOD drilling site directly above the target earthquake locations, which are the proposed source locations to be drilled by the SAFOD project. This local seismic array was deployed to help triangulate the exact locations of the target events as well as capture the background seismicity to study the fault-zone properties. The 2004 Parkfield seismic array deployed subsequent to the **M** 6.0 mainshock was located approximately 12 km south of the SAFOD drilling site and approximately 3 km north of the town of Parkfield. The arrays were not colocated due to difficulty in permitting the SAFOD array site in 2004. Both our experiments used REFTEK recording systems with 2-Hz L22 sensors from the PASSCAL instrument center. The data were recorded at a rate of 100 samples per sec.

The 2003 SAFOD seismic array had 30 instruments deployed in a 2400-m-long cross-fault array and an additional 12 stations deployed for 400 m along the main trace of the SAF. The six-week deployment to record background seismicity was from mid-October to the end of November, 2003. The SAFOD site is located about 1 km from of the southwestern end of the cross-fault array (Fig. 1). The station spacing is irregular with a symmetric distribution across the fault, but with some gaps due to difficult field access. Station spacing near the fault is 50 m and increases to 200 m away from the fault. During the deployment, over 200 earthquakes were recorded by the array, most with magnitudes less than 2.0. Several of these events were very close to the SAFOD drilling target events and occurred almost directly under our array. These events are especially interesting as the seismic waves likely travel vertically through the fault zone and provide ideal waveforms with which to study the anisotropy of the SAF zone.

A second deployment took place in 2004 following the **M** 6.0 earthquake on 28 September 2004, referred to as the Parkfield array. The cross-fault array, in this case, has 45 three-component seismometers in an 850-m-long cross-fault and two along-fault arrays, each approximately 400 m long. The along-fault arrays were located on the main trace of the SAF which broke during the **M** 6.0 mainshock, and a secondary branch of the SAF located about 500 m north of the main trace (Fig. 1). The station spacing is 25 m in the cross-fault array and 50 m in the along-fault arrays. This deployment was operated for three months from October to December 2004 and captured almost 1000 aftershocks. An array colocated at this site was previously deployed in 2002; however, due to the very small number of earthquakes recorded (<5) at large distances from the array, no comparisons with the 2004 data could be made.

Data and Processing

In this article, we present both the 2003 SAFOD and 2004 Parkfield shear-wave splitting data to determine anisotropy near the SAF. At these locations, the seismicity tends to concentrate on or very close to the main strand of the SAF, resulting in a linear distribution of earthquakes. This limits the number of earthquakes that fall within the shear-wave window, which requires an angle of incidence of less than 45°, available to determine anisotropy parameters. However, the moderate rate of earthquakes during both deployments gives sufficient datasets to study the anisotropy. In this study, we include results for 34 earthquakes recorded in 2003 and 96 earthquakes recorded in 2004; one or more stations recorded each earthquake.

The complexity of the local geologic structure hinders accurate measurements of the shear-wave splitting. The seismograms are affected by scattered waves due to local extreme velocity contrasts across the fault (Thurber *et al.*, 2006), and many do not have the impulsive shear-wave arrivals essential for anisotropy studies. And, due to the distribution of earthquakes, the seismic waves traveling to the arrays are likely propagating nearly parallel to the main fault trace, allowing only a narrow region near the fault to be sampled. To objectively determine the anisotropy parameters, we employ an automatic program to determine the fast direction and delay time and the associated quality. With the large dataset available, it would be prohibitively time consuming to individually examine each record visually for splitting parameters.

We use the splitting program implemented by Peng and Ben-Zion (2004) that is modeled after the original code by Silver and Chan (1991). The code determines the splitting parameters using the covariance matrix method for the horizontal components and also tests the quality of the data. The data shown in this article must pass a set of 10 quality tests based on previous studies by Cochran *et al.* (2003), Gerst (2003), and Matcham *et al.* (2000) to ensure reliable and replicable shear-wave splitting measurements. Included are tests of the signal-to-noise ratio, the stability of both the fast direction and delay time over a sliding time window, and cross-correlation value, among others.

2003 SAFOD Array Results

We determined anisotropy parameters from 34 earthquakes recorded during the 6-week SAFOD deployment in 2003. The 2-km-wide dense cross-fault array provides us with a unique opportunity to study the distribution of micro-

crack orientations and densities approaching the SAF. The splitting of a shear wave can occur anywhere on the path between the source and the receiver, so we plot the data in several ways to look for systematic patterns in the data with common sources or common receivers (Fig. 2). It is likely, however, that the largest contribution is from the shallow path (e.g., Cochran *et al.*, 2003; Peng and Ben-Zion, 2004).

The high-quality splitting measurements of the fast direction and delay time for 247 earthquake–SAFOD station combinations are given in Figure 2. One or more seismic stations recorded each of the earthquakes studied, and we plot the measured splitting parameters on both the station location and source location. As is evident from the plot, significant scatter is present in the both the fast direction and delay times. The orientation of the fast-arriving shear wave is related to the orientation of the aligned crack or shear fabric that causes the splitting. If the anisotropy is caused by aligned cracks, then the fast direction aligns with the maximum compressive stress field. In addition, we might expect a strong shear fabric within the SAF core as it is a highly evolved fault system with kilometers of accumulated slip.

From the plot in Figure 2, it is evident that neither the near-source nor the near-receiver region dominates the fast orientations. Instead, the fast direction is dependent on the path, whether the path crosses the fault core, and how far the station is from the fault. Note that the earthquake locations shown in Figure 2a are likely closer to the fault plane than plotted, as the catalog locations were pulled to the southwest by the large velocity contrast across the fault. Unfortunately, relocated earthquake locations are only available for a small subset of the data (J. Hardebeck, personal comm., 2005). In general, the fast directions measured from earthquakes that occurred directly under the array appear to show a fault-parallel preferential direction. In contrast, an event located approximately 5 km northwest of the array but still on the trace of the SAF shows nearly fault perpendicular fast directions. The earthquakes located slightly off the fault show greater scatter in the measured fast directions, most likely varying according to whether the path crosses the main fault trace.

Figures 3a and 3b plot the rose diagrams and equal area diagrams for each station of the 2003 SAFOD array for the cross and along fault arrays, respectively. The rose diagrams show the preferred fast directions measured at each station in the array. The equal area plots show how splitting results vary with source backazimuth and angle of incidence. The fast directions and delay times are highly dependent on source and received location suggesting significant fine-scale spatial variation in splitting properties.

We look in detail at the fast directions measured by stations in our along- and cross-fault arrays to determine the anisotropic parameters near the fault. Figure 4 plots rose diagrams of the distribution of fast directions for station groups. Stations were grouped based on distance from the main fault trace to determine if the splitting changes with distance from the fault.

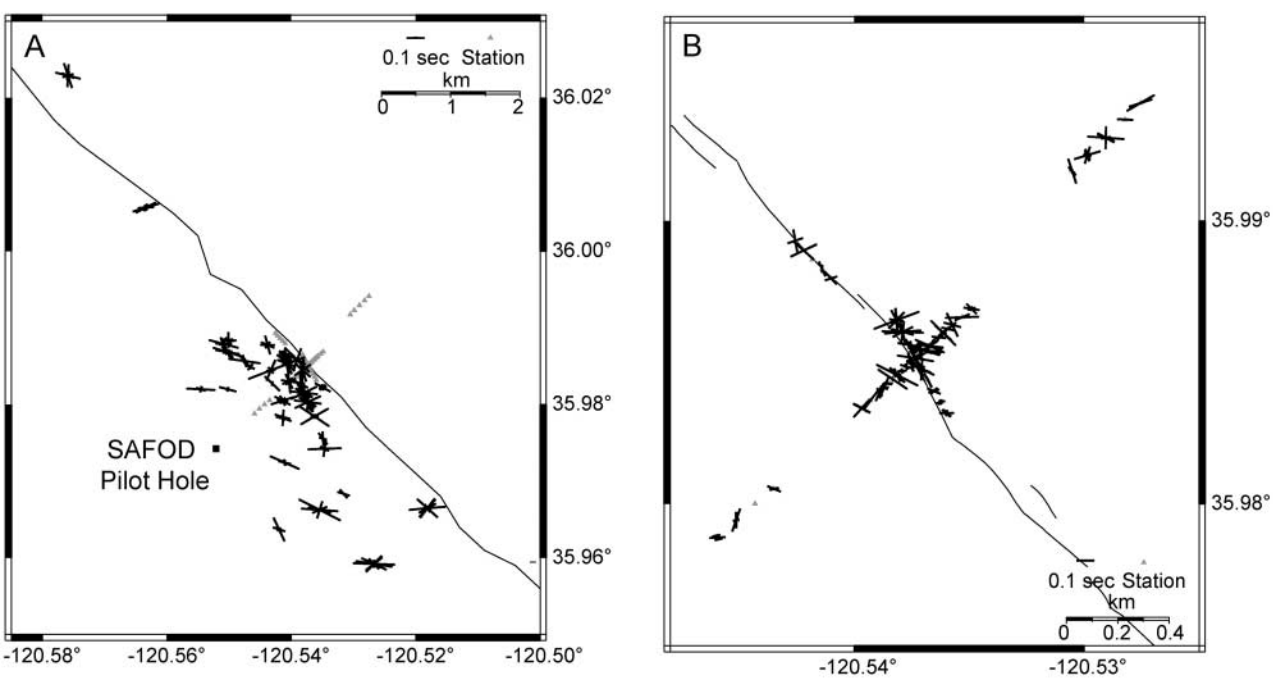

Figure 2. Shear-wave splitting measurements from the 2003 SAFOD array. Station locations are indicated by gray triangles, and the SAF is plotted as a solid line. Bars are oriented parallel to the fast direction and scaled by the delay time. (A) Splitting results plotted on earthquake epicenter. (B) Splitting results plotted on station location. Surface trace in Figure 2B is from mapping by Rymer *et al.* (2006).

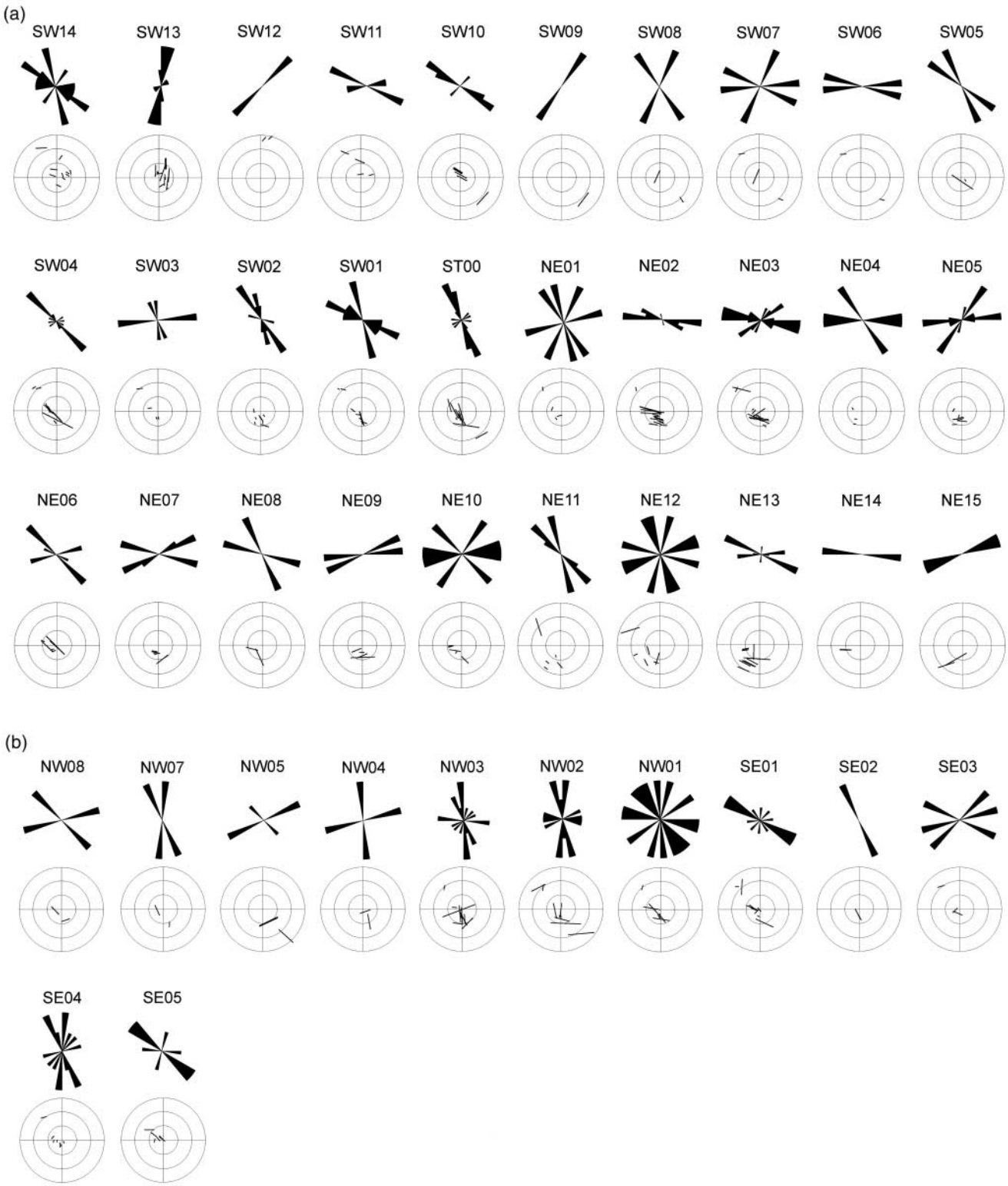

Figure 3. Rose diagrams and equal area plots of splitting parameters for each station in the 2003 SAFOD seismic array. Rose diagrams plot the polar histogram of measured fast directions only. On the equal area diagrams, splitting results are plotted on the earthquake backazimuth and angle of incidence. Bars are oriented parallel to the fast direction and scaled by delay time. Note that the radius of the equal area ranges from 0 to 45, since data processing is limited to events within the shear-wave window. (a) Results for the cross-fault stations ordered from the southwest to northeast. (b) Results for the along-fault stations ordered from the northwest to the southeast.

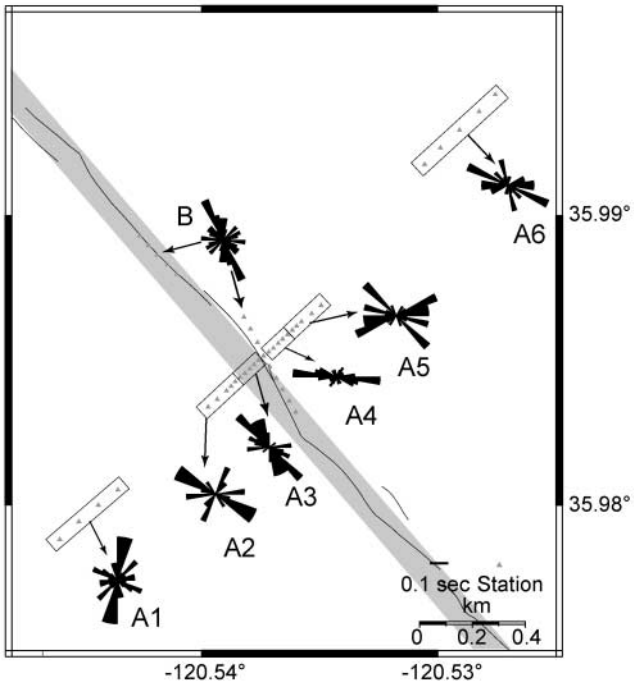

Figure 4. Rose diagrams giving a polar histogram of the fast orientations from 2003. Fast directions are grouped by station location. Groups A (1–6) are splitting measurements from the cross-fault array, and Group B is results from the along-fault array. Gray rectangle shows the reduced velocity fault zone as determined by Li *et al.* (2006). Plotted fault trace is mapping by Rymer *et al.* (2006).

Group B, consisting of stations located on the main trace of the SAF, shows a preferential fast orientation roughly fault parallel. A similar pattern is seen for group A3 located close to the main trace on the southwest side of the fault. Away from the fault, to the southwest, the dominant direction becomes approximately N70°W for group A2. Group A1, roughly 1 km from the fault, shows directions oriented predominately N10°E. On the northeast side of the fault we see a mix of dominant fast directions from fault parallel to roughly east–west. The northeast side of the fault at the SAFOD array location has topography that may affect the accuracy of the splitting measurements due to scattered waves arriving soon after the *S* arrival. In addition, the basement rock type changes from granite to lower velocity Franciscan formation (e.g., Eberhart-Philips and Michael, 1993; Unsworth *et al.*, 1997) across the fault, likely causing scattering of the shear arrivals that may affect the measured splitting. The detailed velocity structure across the SAF near the 2003 SAFOD arrays and the possible effect on the anisotropy measurements will be discussed in more detail subsequently.

It is very common to observe large scatter in delay times measured using shear-wave splitting (e.g., Cochran *et al.*, 2003; Crampin *et al.*, 2004; Peng and Ben-Zion, 2004; Savage *et al.*, 1989; Zhang and Schwartz, 1994). Scattered delay times reflect high spatial variability in the fracture density within the upper crust, substantial variation in shear fabric across the fault, or possibly contamination by scattering. Assuming anisotropy is constant along the source-receiver path, the average anisotropy for all of the measurements at the SAFOD array is 0.014 sec/km, with individual measurements ranging between 0.002 and 0.06 sec/km.

2004 Parkfield Array Results

Shortly after the **M** 6.0 Parkfield earthquake on 28 September 2004, we again recorded earthquakes on cross- and along-fault arrays to determine the anisotropy near the SAF at Parkfield. Although the 2003 and 2004 arrays are not colocated, they are within 12 km along a continuous section of the SAF. The fast orientations and delay times measured subsequent to the **M** 6.0 mainshock to determine whether spatial variation is similar to that observed in 2003. We looked specifically for any temporal changes in the splitting parameters that could be attributed to coseismic perturbation of the anisotropic field. Due to the high aftershock productivity following the mainshock we recorded a large number of events suitable for shear-wave splitting analysis.

Figure 5 shows splitting parameters plotted on source and receiver locations at the 2004 Parkfield array. Only the 300 high-quality results are plotted as obtained from the automated processing that pass the 10 quality factors outlined previously. We see a wide range of splitting parameters that can not be explained by purely near-source or near-receiver properties, similar to scatter seen the 2003 analysis. It is clear from the figure that there is again high spatial variability in anisotropy. In Figure 6, the rose diagrams and equal area diagrams are plotted for each station to better demonstrate the spatial distribution of the data. The rose diagrams show the dominant fast orientations measured at each station and equal area plots plot the fast direction and delay time at the propagation backazimuth and incident angle. While significant scatter is present in the results, similar source-receiver paths give similar splitting measurements, suggesting a somewhat continuous anisotropic field.

We group the fast direction data based on distance from the fault and note the average orientations (Fig. 7). The cross-fault array is split into six groups based on distance from the main and northern fault traces. We examine the fast orientations from southwest to northeast. Group A1, at a distance range of 150–250 m west of the main fault trace show orientations concentrated at near fault parallel and at N30°E. Group A2, on the southwest side of the main trace, shows predominately fault-parallel fast orientations. Group A3 has a mix of orientations, but concentrated at N20°W and N70°E. Group A4, centered between the two fault traces, the main branch of the SAF and the northern branch, shows nearly north–south fast directions. Group A5 shows a mix of fast orientations. Group A6 also has a mix of orientations, but shows fast directions parallel to the northern fault branch and fast directions nearly north–south. Both along-fault groups B and C show a mix of fast directions, but with a preferential

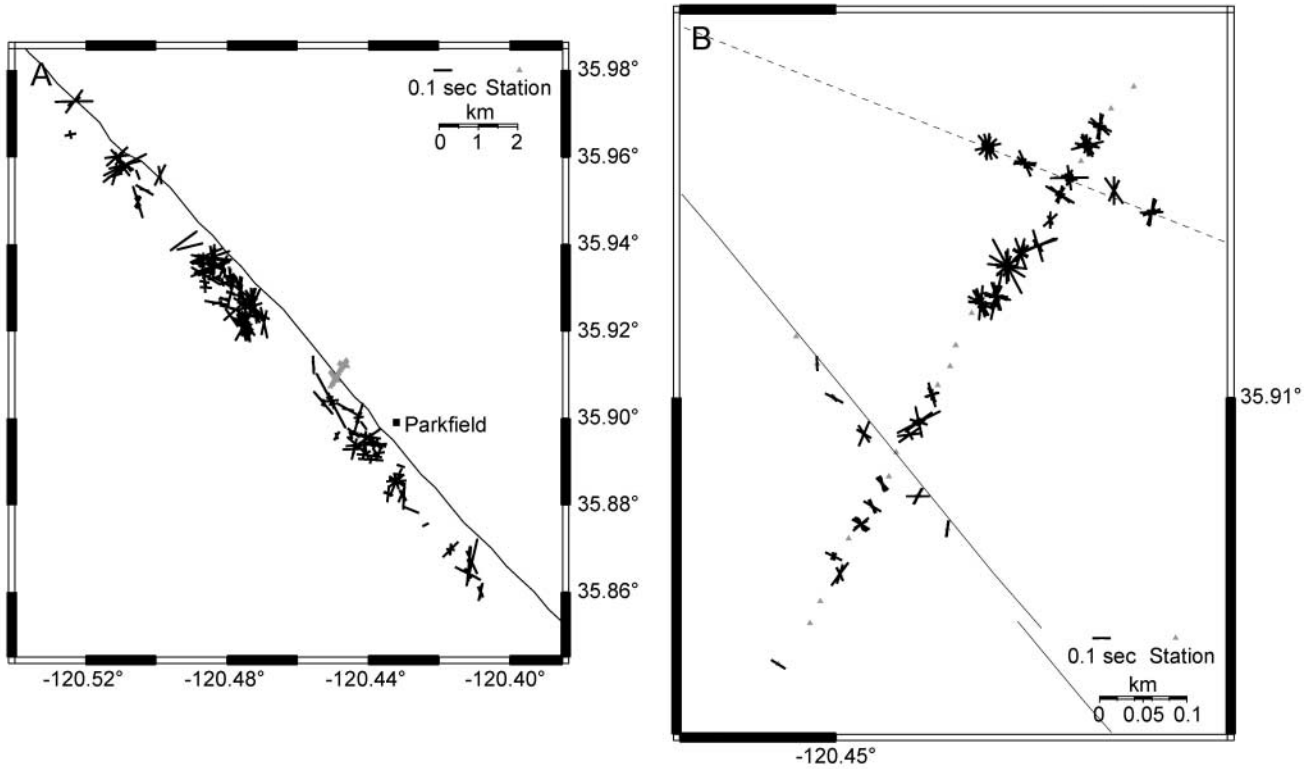

Figure 5. Shear-wave splitting measurements from the 2004 Parkfield array. Station locations are indicated by gray triangles, and the SAF is plotted as a solid line. Bars are oriented parallel to the fast direction and scaled by the delay time. (A) Splitting results plotted on earthquake epicenter. (B) Splitting results plotted on station location.

alignment parallel to the strike of the fault. Overall, we see a pattern very similar to what was observed in 2003.

Path-normalized delay times are scattered and range from 0.002 sec/km to 0.05 msec/km. The average delay time normalized by path length for all 300 Parkfield splitting measurements is 0.012 sec/km. However, the shallowest part of the crust likely has the greatest contribution to the splitting (Cochran *et al.*, 2003; Peng and Ben-Zion, 2004), so path averaging may not be an accurate description of the delay times. Possible depth dependence will be discussed in more detail in the Discussion.

Discussion

Shear-wave splitting measurements have been used extensively to determine the anisotropic field in the shallow crust. However, due to variability in splitting measurements it can be difficult to determine the cause, location, and extent of the anisotropic body in the crust. Data recorded at two temporary array locations near the SAF prior to and following the 2004 **M** 6.0 Parkfield earthquake are analyzed to determine the characteristics of the near-fault anisotropic field. We examine the shear-wave splitting data for spatial distribution of anisotropy as well as any evidence for temporal changes due to the mainshock rupture.

The fast orientations measured by the 2003 SAFOD and 2004 Parkfield arrays show similar overall trends. The measured fast directions are oriented nearly fault-parallel for those stations located along the main trace of the SAF for both the SAFOD and Parkfield arrays. Stations at both arrays that are on the southwest side of the SAF and also within 100 m of the main trace also have fast directions that are strongly fault parallel. In addition, predominately fault-parallel fast orientations are also measured on the 2004 Parkfield array stations sited along a secondary branch of the SAF.

Outside of the fault zone, the fast directions recovered using shear-wave splitting techniques are fairly scattered. The fast orientation data for both the 2003 SAFOD and 2004 Parkfield arrays are shown in Figure 8. The 2004 Parkfield data (Fig. 8B) shows three dominant directions on the polar histogram. Two of the orientations are related to the strike of the main and northern branches of the SAF, while the third is oriented roughly N10°E. The local background stress direction has been shown to be rotated roughly 45° from the strike of the SAF, within 1–10 km of the main fault trace (Hardebeck and Michael, 2004; Provost and Houston, 2001). This would correspond to the third dominant fast orientation we see at distances of 100 m or greater from the two fault branches. In contrast, the 2003 data does not show a similar

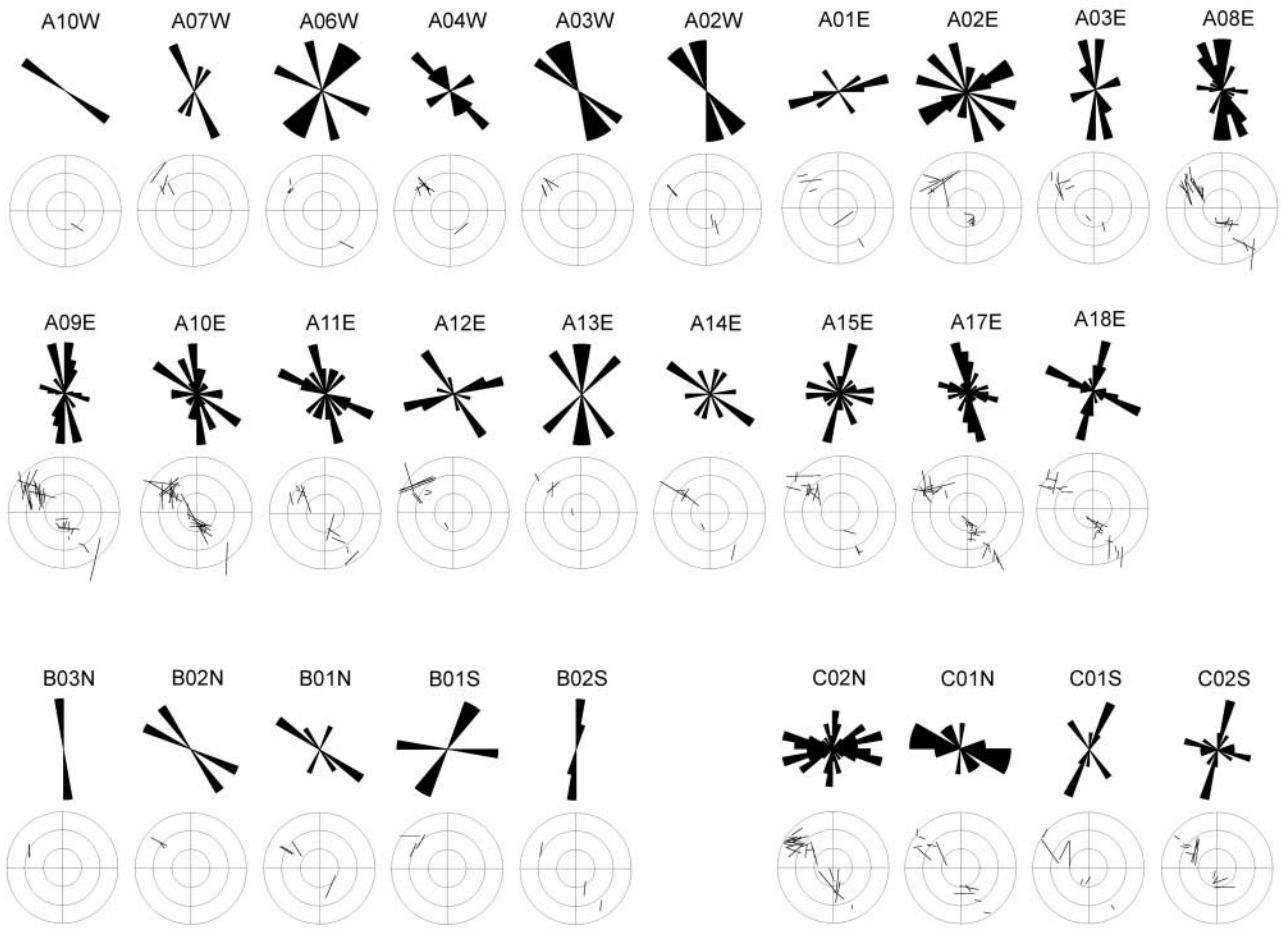

Figure 6. Rose diagrams and equal area plots of splitting parameters for each station in the 2004 Parkfield seismic array. See Figure 3 for more detail. Stations A10W to A02W are west of the main trace of the SAF. Stations A01E to A15E are between the main trace and the northern branch of the SAF. Stations A17E and A18E are east of the northern branch. Array station names beginning with B and C are in the along-fault arrays of the main branch and northern branch, respectively.

dominant N10°E direction as shown in Figure 8a. The orientation data are more scattered and are not strongly related to the strike of the fault or the local background stress direction.

Given that the two arrays are separated by 12 km along the SAF, it is important to compare the structural and material properties of the two locations. A significant number of characterization studies have been conducted along the Parkfield segment of the SAF (e.g., Catchings *et al.*, 2002; Eberhart-Phillips *et al.*, 2003; Thurber *et al.*, 2006; Unsworth *et al.*, 1997). Structurally, both arrays span a section of the SAF that has been described as a flower structure (e.g., Catchings *et al.*, 2002) with several subsidiary branches splaying off of the main fault trace. At the Parkfield array, instruments were deployed along the main fault strand and a secondary branch to the north of the main trace. The anisotropic parameters are clearly affected by this secondary branch as stated previously.

Thurber *et al.* (2006) inverted thousands of earthquake arrival times for the velocity structure along the SAF near Parkfield. The trait common to many of the fault-normal cross sections is a clear velocity contrast across the SAF with a 0.5–1.0 km/sec lower velocity on the northeast side of the fault compared with that on the southwest side of the fault. The velocity cross section −3 of Thurber *et al.* (2006) is colocated with our 2003 SAFOD array, and cross section 9 is close to our 2004 Parkfield array. While the two velocity cross sections are similar, there is a greater velocity contrast across the SAF at the SAFOD array. The large velocity across the fault at the 2003 SAFOD array likely causes an increase in scattered arrivals and may affect the shear-wave splitting measurements. At the 2003 SAFOD array, a clear N10°E dominant fast direction is seen for the stations farthest from the fault on the southwest side. However, no dominant fast direction is observed on the northeast side (Fig. 4).

It is often difficult to determine the cause of the observed shear-wave splitting, as there are several known physical mechanisms, including aligned microcracks, shear

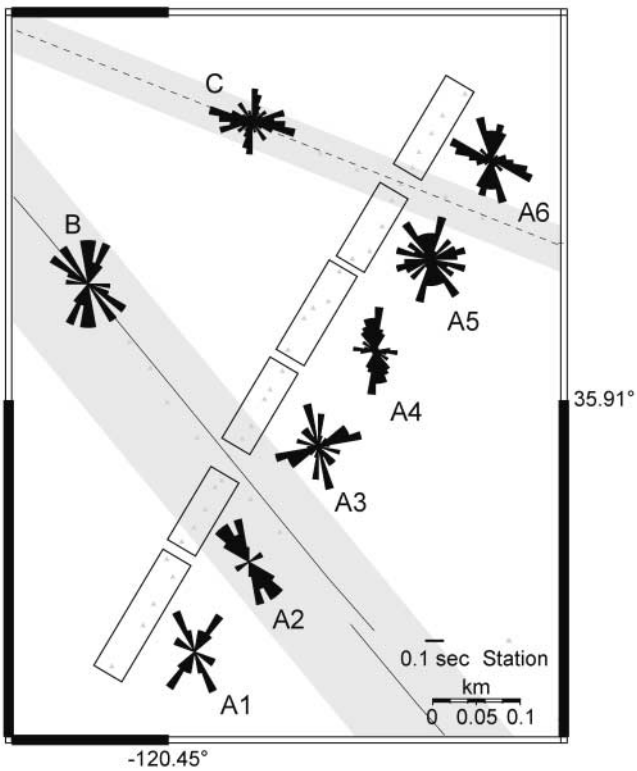

Figure 7. Rose diagrams giving a polar histogram of the fast orientations from 2004. Fast directions grouped by station location. Groups A (1–6) are splitting orientations from the cross-fault array. Group B are the fast orientations from the along-fault array on the main trace of the SAF. Group C are those from along the northern branch of the SAF approximate location shown by a dotted line.

fabric, and preferential alignment of grains. Boness and Zoback (2004a) conducted a study of anisotropy in the SAFOD pilot hole and used a suite of borehole measurements to match the physical phenomena with the recorded shear-wave splitting. They report that the majority of splitting measurements correspond to the maximum compressive stress direction as determined from borehole breakouts, suggestive of aligned microcracks. In localized areas, anisotropy is attributed to shear fabric as seismic waves pass through highly fractured zones of slip. Therefore, we interpret that the observed anisotropy away from the main slip zones is due to aligned microcracks.

However, stations within and adjacent to the major fault traces have systematically different measured splitting orientations. There is preferential alignment parallel to the fault suggesting a strong anisotropy that could either be attributed to a shear fabric related to a highly fractured shear zone or aligned microcracks that are reoriented due to a rotation in the stress field close to the fault. Fault-zone-trapped wave studies conducted along the SAF using the same seismic array data as presented here show a strong trapping structure with reduced velocities along the fault and also to the southwest of the fault in the width range of ~100 m (Li *et al.*, 2004, 2006). Similar to the borehole study by Boness and Zoback (2004a), the low-velocity trapping structure is associated with the strongly preferred fast direction reported here. Given the similarity between the anisotropy traits and velocity measurements measured here and in the pilot hole, we suggest that the splitting in the SAF core is likely due to shear fabric. In addition, we see no evidence of a gradual change in the fast orientations, which would be more indicative of a rotation of the stress field as the SAF is approached.

The local anisotropic field is clearly affected by the presence of the SAF, but we see little change in either fast orientations or delay times due to the 2004 **M** 6.0 mainshock. Our results are in agreement with Boness and Zoback (2004b), who reported that anisotropy results from the Parkfield permanent array stations show no evidence for a change in either fast orientation or delay time at the time of the 2004 **M** 6.0 Parkfield earthquake. It is important to note that, due to the spatial separation of our two array sites, it is difficult to definitively state that no change in the anisotropy occurred concurrent with the mainshock at these locations.

Trapped-wave data clearly indicate a decrease in the velocities in the fault core and a recovery of velocities during 3 months following the mainshock (Li *et al.*, 2006); however, we see no evidence for coseismic or postseismic changes in anisotropy parameters. The coseismic velocity decrease observed using fault zone trapped waves in the fault core is 2.5%, and recovery is on the order of 1%–2%. However, temporal variation concurrent with the Parkfield earthquake is not observed, indicating low sensitivity of anisotropy measurements to temporal changes. As reported by Peng and Ben-Zion (2005), temporal changes are observed in the direct *S*-wave and early *S*-wave coda, but the fast and slow shear-waves are affected equally, resulting in no net change in the measured shear-wave splitting.

The density of microcracks in the shallow crust, away from the fault core, is difficult to determine due to high variability in delay times measured using shear-wave splitting techniques. Figure 9 shows the delay time versus hypocentral distance and source depth for both 2003 and 2004 datasets. The largest contribution to microcrack-controlled anisotropy is from the shallow crust where confining pressures are lower and cracks can remain open. If the majority of the observed anisotropy is due to aligned microcracks, we can estimate the apparent crack density using $\varepsilon = \upsilon_s(\delta t/L)$, where ε is the apparent crack density, υ_s is the shear velocity in the uncracked medium, and $\delta t/L$ is the path-normalized delay time (Hudson, 1981; O'Connell and Budiansky, 1974). The average crack density near the SAF at both the 2003 SAFOD and 2004 Parkfield arrays is at least 3%, assuming a shear-wave velocity of 2.5 km/sec and taking the average of the path-normalized delay times. It is more likely that the anisotropy is confined to the upper 3–5 km, which would result in a greater apparent crack density in the uppermost crust than stated previously.

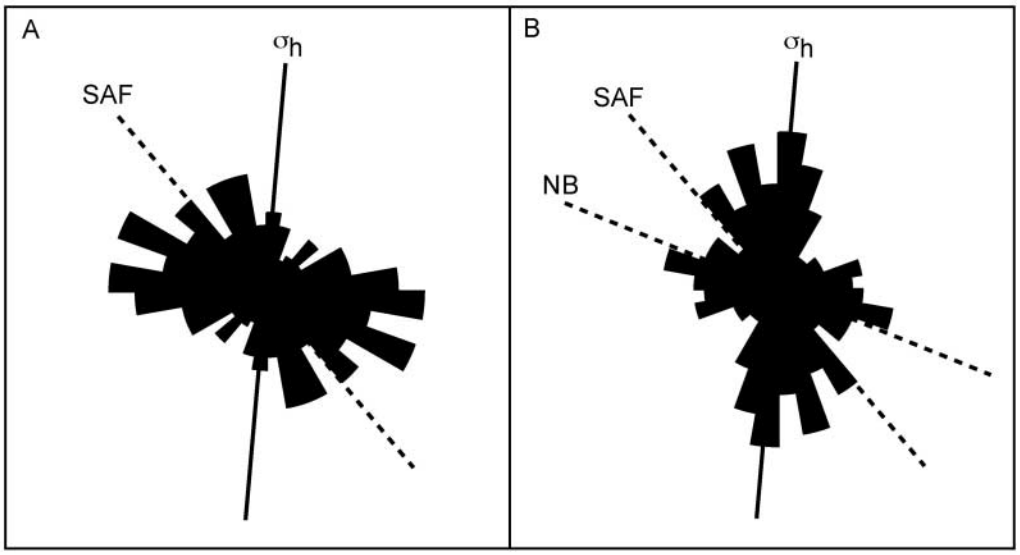

Figure 8. Rose diagram giving the polar histogram of fast directions for (A) the 2003 SAFOD array and (B) the 2004 Parkfield array. The solid line gives the orientation of the local within 1–3 km from the fault maximum compressive stress direction (O_h) from Provost and Houston (2001). The dashed line gives the strike of the SAF and the northern branch (NB) of the SAF. Gray rectangles roughly denote the location of the reduced velocity fault zone as determined by Li *et al.* (2004).

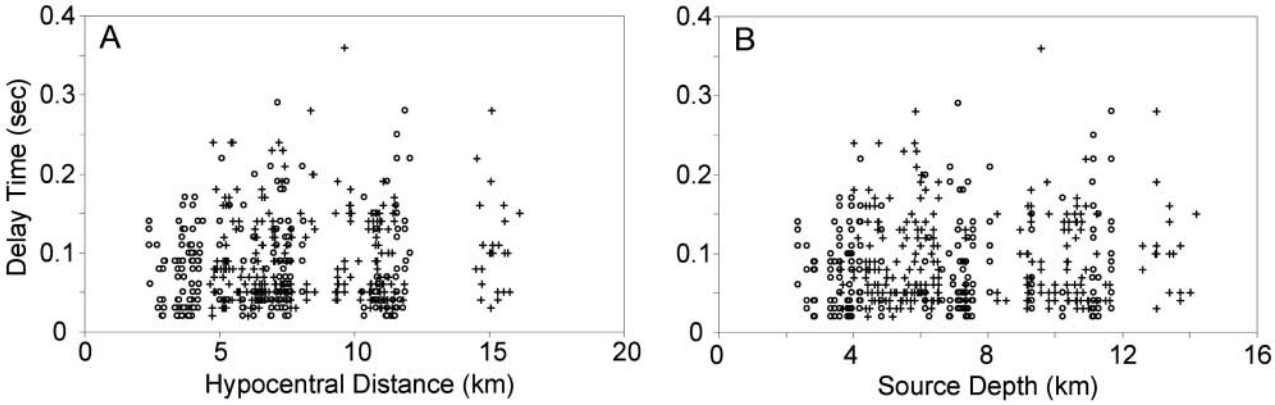

Figure 9. Delay times from 2003 SAFOD and 2004 Parkfield seismic array data shown by circles and crosses, respectively. (A) Delay time versus hypocentral distance. (B) Delay time versus source depth.

The data are very scattered, and it is difficult to draw a conclusive statement about the depth dependence. Several studies have shown a lack of a correlation between event depth and measured delay time, suggesting that the highly anisotropic medium is confined to the upper 3–5 km (Cochran *et al.*, 2003; Peng and Ben-Zion, 2004). However, the data from all the events above 4 km show delay time less than 0.175 sec, but events at depths between 4 and 8 km show delay times up to 0.3 sec showing that the anisotropy likely persists to depth of ~7–8 km. Both Figure 9A and 9B hint at possible depth/distance dependence, but no significant correlation is evident. It is important to note that the delay times for ray paths that primarily travel through the fault core are more strongly influenced by the shear fabric.

Shear-wave splitting measurements near the SAF are highly spatially variable and clearly affected by the presence of the fault. The fast direction is fault parallel for stations directly on the fault and additionally for stations within 100 m to the southwest of the surface trace. This zone of fault-parallel fast directions overlies the region of significant velocity decrease as determined using fault-zone-trapped wave by Li *et al.* (2004, 2006). The anisotropy is likely due to aligned cracks away from the fault and shear fabric within the 100-m-wide fault zone.

Acknowledgments

We would like to thank Z. Peng for the use of his automated splitting code and for many useful discussions throughout the course of this research. Many thanks to SAFOD principle investigators S. Hickman, W. Ellsworth, and M. Zoback for helping coordinate our seismic characterization studies of the SAFOD drilling site. Thanks to J. Rubinstein and an anonymous reviewer for insightful comments to improve the manuscript. We acknowledge J. Varian, G. Varian, G. Work, K. Kester, and B. Mosby for permission to conduct the experiment on their land. We are grateful to P. Malin, C. Thurber, S. Roecker, M. Rymer, R. Catchings, A. Snyder, R. Rusell, L. Powell, B. Nadeau, D. McPhee, and F. Niu for their collaboration in our research at Parkfield. We also thank IRIS for the use of PASSCAL instruments in 2003 and 2004. Seismic data processing was done using Seismic Analysis Code (SAC), and several figures were made with Generic Mapping Tools (GMT) (Wessel and Smith, 1998). This study was supported by NSF/EarthScope Grant EAR-0342277 and the Southern California Earthquake Center (SCEC). SCEC is funded by The National Science Foundation (NSF) Cooperative Agreement EAR-0106924 and USGS Cooperative Agreement 02HQAG0008.

References

Boness, N. L., and M. D. Zoback (2004a). Stress-induced seismic velocity anisotropy and physical properties in the SAFOD Pilot Hole in Parkfield, California, *Geophys. Res. Lett.* **31,** L15S17, doi 10.1029/2003GL019020.

Boness, N. L, and M. D. Zoback (2004b). Multi-scale crustal seismic anisotropy in the region surrounding the San Andreas fault near Parkfield, California, *EOS Trans. AGU* **85,** no. 47, Fall Meet. Suppl., T11F-05 (abstract).

Catchings, R. D., M. J. Rymer, M. R. Goldman, J. A. Hole, R. Huggins, and C. Lippus (2002). High-resolution seismic velocities and shallow structure of the San Andreas fault zone at Middle Mountain, Parkfield, California, *Bull. Seism. Soc. Am.* **92,** 2493–2503.

Cochran, E. S., J. E. Vidale, and Y.-G. Li (2003). Near-fault anisotropy following the Hector Mine earthquake, *J. Geophys. Res.* **108,** 2436, doi 10.1029/2002JB002352.

Crampin, S. (1990). The scattering of shear waves in the crust, *Pure Appl. Geophys.* **132,** 67–91.

Crampin, S., and S. Chastin (2003). A review of shear-wave splitting in the crack-critical crust, *Geophys. J. Int.* **155,** 221–240.

Crampin, S., and S. V. Zatsepin (1997). Modelling the compliance of crustal rock. II. Response to temporal changes before earthquakes, *Geophys. J. Int.* **129,** 495–506.

Crampin, S., S. Peacock, Y. Gao, and S. Chastin (2004). The scatter of time-delays in shear-wave splitting above small earthquakes, *Geophys. J. Int.* **156,** 39–44.

Eberhart-Phillips, D., and A. J. Michael (1993). Three-dimensional velocity structure, seismicity, and fault structure in the Parkfield region, central California, *J. Geophys. Res.* **98,** 15,737–15,758.

Gao, Y., P. Wang, S. Zheng, M. Wang, Y. Chen, and H. Zhou (1998). Temporal changes in shear-wave splitting at an isolated swarm of small earthquakes in 1992 near Dongfang, Hainan Island, southern China, *Geophys. J. Int.* **135,** 102–12.

Gerst, A. (2003). Temporal changes in seismic anisotropy as a new eruption forecasting tool? *MSc Thesis*, Victoria University of Wellington, Wellington.

Hardebeck, J. L., and A. J. Michael (2004). Stress orientations at intermediate angles to the San Andreas Fault, California, *J. Geophys. Res.* **109,** B11303, doi 10.1029/2004JB003239.

Hudson, J. A. (1981). Wave speeds and attenuation of elastic waves in material containing cracks, *Geophys. J. R. Astron. Soc.* **64,** 133–50.

Hudson, J. A. (1994). Overall properties of anisotropic materials containing cracks, *Geophys. J. Int.* **116,** 279–82.

Li, Y.-G., P. Chen, E. S. Cochran, J. E. Vidale, and T. Burdette (2006). Seismic evidence for rock damage and healing on the San Andreas fault associated with the 2004 **M** 6.0 Parkfield Earthquake, *Bull. Seism. Soc. Am.* **96,** no. 4B, S349–S363.

Li, Y.-G., J. E. Vidale, K. Aki, F. Xu, and T. Burdette (1998). Evidence of shallow fault zone strengthening after the 1992 M7.5 Landers, California, earthquake, *Science* **279,** 217–219.

Li, Y-G., J. E. Vidale, and E. S. Cochran (2004). Low-velocity damaged structure of the San Andreas Fault at Parkfield from fault zone trapped waves, *Geophys. Res. Lett.* **31,** L12S06, doi 10.1029/2003GL019044.

Li, Y.-G., J. E. Vidale, S. M. Day, D. D. Ogelsby, and E. Cochran (2003). Postseismic fault healing on the rupture zone of the 1999 M7.1 Hector Mine, California, earthquake, *Bull. Seism. Soc. Am.*, **93,** 854–869.

Matcham, I., M. K. Savage, and K. R. Gledhill (2000). Distribution of seismic anisotropy in the subduction zone beneath the Wellington region, New Zealand, *Geophys. J. Int.* **140,** 1–10.

O'Connell, R. J., and B. Budiansky (1974). Seismic velocities in dry and saturated cracked solids, *J. Geophys. Res.* **79,** 5412–5426.

Peng, Z., and Y. Ben-Zion (2004). Systematic analysis of crustal anisotropy along the Karadere-Düzce branch of the North Anatolian Fault, *Geophys. J. Int.* **159,** 253–274.

Peng, Z., and Y. Ben-Zion (2005). Temporal changes of shallow seismic velocity around the Karadere-Düzce branch of the north Anatolian fault and strong ground motion, *Pure Appl. Geophys.* "Advances in Studies of Heterogeneities in the Earth's Lithosphere: The Keiiti Aki Volume II" **163,** 567–599, doi 10.1007/s0002400500346doi.

Provost, A.-S., and H. Houston (2001). Orientation of the stress field surrounding the creeping section of the San Andreas fault: evidence for a narrow mechanically weak fault zone, *J. Geophys. Res.* **106,** 11,373–11,386.

Rubinstein, J. L., and G. C. Beroza (2005). Depth constraints on nonlinear strong ground motion, *Geophys. Res. Lett.* **32,** L14313, doi 10.1029/2005GL023189.

Rymer, M. J. (2006). Surface fault slip associated with the 2004 Parkfield, California, earthquake, *Bull. Seism. Soc. Am.* **96,** no. 4B, S11–S27.

Savage, M. K., X. R. Shih, R. P. Meyer, and R. C. Aster (1989). Shear-wave anisotropy of active tectonic regions via automated shear-wave polarization analysis, *Tectonophysics* **165,** 279–292.

Schaff, D. P., and G. C. Beroza (2004). Coseismic and postseismic velocity changes measured by repeating earthquakes, *J. Geophys. Res.* **109,** B103002, doi 10.1029/2004JB003011.

Silver, P. G., and W. W. Chan (1991). Shear-wave splitting and subcontinental mantle deformation, *J. Geophys. Res.* **96,** 16,429–16,454.

Tadokoro, K., M. Ando, and Y. Umeda (1999). S-wave splitting in the aftershock region of the 1995 Hyogo-ken Nanbu earthquake, *J. Geophys. Res.* **104,** 981–991.

Teanby, N., J.-M. Kendall, R. H. Jones, and O. Barkved (2004). Stress-induced temporal variation in seismic anisotropy observed in microseismic data, *Geophys. J. Int.* **156,** 459–466.

Thurber, C., H. Zhang, F. Waldhauser, J. Hardebeck, A. Michael, and D. Eberhard-Phillips (2006). Three-dimensional compressional wave-speed model, earthquake relocations, and focal mechanisms for the Parkfield, California, region, *Bull. Seism. Soc. Am.* **96,** no. 4B, S38–S49

Townend, J., and M. D. Zoback (2004). Regional tectonic stress near the San Andreas fault in central and southern California, *Geophys. Res. Lett.* **31,** L15S11, doi 10.1029/2003GL018918.

Unsworth, M. J., P. E. Malin, G. D. Egbert, and J. R. Booker (1997). Internal structure of the San Andreas fault at Parkfield, California, *Geology* **25,** 359–362.

Wessel, P., and W. H. F. Y. Smith (1998). New, improved version of the Generic Mapping Tools released, *EOS Trans. AGU* **79,** 579.

Zatsepin, S. V., and S. Crampin (1997). Modelling the compliance of crustal rock. I. Response of shear-wave splitting to differential stress, *Geophys. J. Int.* **129,** 477–494.

Zhang, Z., and S. Y. Schwartz (1994). Seismic anisotropy in the shallow crust of the Loma Prieta segment of the San Andreas fault system, *J. Geophys. Res.* **99,** 9651–9661.

Earth and Space Sciences Department and Institute of Geophysics and Space Physics
University of California
Los Angeles, California 90095-1567
(E.S.C., J.E.V.)

Department of Earth Sciences
University of Southern California
Los Angeles, California 90089-0740
(Y-G.L.)

Manuscript received 26 August 2005.